

AFOSR-TR-91-0635

(2)

AD-A238 858



Grant AFOSR 86-0337



BASIC PROCESSES
OF
PLASMA PROPULSION

Herbert O. Schrade
P. Christian Slezioma
Helmut L. Kurtz

April 1991

Final Scientific Report
1 August 1986 - 31 July 1990

Approved For	
A-1	
DTIC	
JUL 25 1991	
S	
D	
C	
A-1	

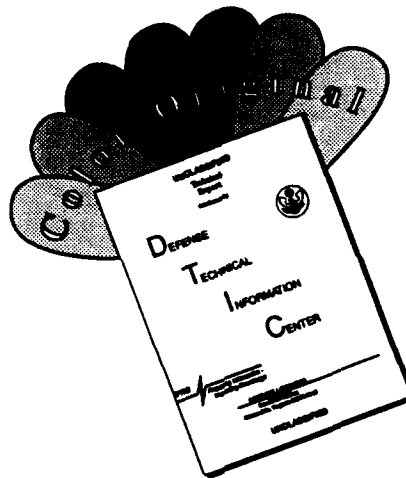
Approved for public release; distribution unlimited
Prepared for the
Air Force Office of Scientific Research
Bolling AFB, DC 20332-6448
through the
European Office of Aerospace Research
and Development
223/231 Old Marylebone Road
London, NW1 5th
England

91-05931



91 7 23 012

DISCLAIMER NOTICE



THIS DOCUMENT IS BEST QUALITY AVAILABLE. THE COPY FURNISHED TO DTIC CONTAINED A SIGNIFICANT NUMBER OF COLOR PAGES WHICH DO NOT REPRODUCE LEGIBLY ON BLACK AND WHITE MICROFICHE.

Preface

The work described in this final report has been sponsored by the Air Force Office of Scientific Research through the European Office of Aerospace Research and Development in London under Grant AFOSR 86 - 0337. The research work period herein is from August 1, 1986 to July 31, 1990.

SECURITY CLASSIFICATION OF THIS PAGE

REPORT DOCUMENTATION PAGE

Form Approved
OMB No. 0704-0188

1a REPORT SECURITY CLASSIFICATION		1b RESTRICTIVE MARKINGS	
2a SECURITY CLASSIFICATION AUTHORITY		3 DISTRIBUTION/AVAILABILITY STATEMENT Approved for public release, distribution unlimited as it appears on the report	
2b DECLASSIFICATION/DOWNGRADING SCHEDULE			
4 PERFORMING ORGANIZATION REPORT NUMBER(S)		5 MONITORING ORGANIZATION REPORT NUMBER(S)	
6a NAME OF PERFORMING ORGANIZATION Inst. f. Raumfahrtssysteme University of Stuttgart	6b OFFICE SYMBOL (if applicable) IRS	7a NAME OF MONITORING ORGANIZATION EOARD, London	
6c ADDRESS (City, State, and ZIP Code) Pfaffenwaldring 31 7000 Stuttgart 80 Germany		7b ADDRESS (City, State, and ZIP Code) AFOSR/NA Boiling AFB DC 20332-6448	
8a NAME OF FUNDING/SPONSORING ORGANIZATION AFOSR/NA Boiling AFB DC 20332-6448	8b OFFICE SYMBOL (if applicable) NA	9 PROCUREMENT INSTRUMENT IDENTIFICATION NUMBER AFOSR Grant 86-00337	
8c ADDRESS (City, State, and ZIP Code) AFOSR/NA Boiling AFB DC 20332-6448		10 SOURCE OF FUNDING NUMBERS PROGRAM ELEMENT NO. 441007 PROJECT NO. 2308 TASK NO. A1 WORK UNIT ACCESSION NO.	
11 TITLE (Include Security Classification) Basic Processes of Plasma Propulsion (not classified)			
12 PERSONAL AUTHOR(S) Herbert O. Schrade, P.Christian Sleciona, Helmut L. Kurtz			
13a TYPE OF REPORT Final	13b TIME COVERED FROM Aug. 86 to July 90	14 DATE OF REPORT (Year, Month, Day) 1991, Jan., 15	15 PAGE COUNT
16 SUPPLEMENTARY NOTATION			
17 COSATI CODES FIELD GROUP SUB-GROUP		18 SUBJECT TERMS (Continue on reverse if necessary and identify by block number)	
19 ABSTRACT (Continue on reverse if necessary and identify by block number) <p>In order to improve performance, lifetime and reliability of plasma thrusters one has to understand and asses the fundamental processes and problem areas like nonequilibrium magneto plasma dynamics flows in electric discharges, their stability and electrode erosion effects. In order to asses the flow, pressure and density or temperature fields in plasma thruster devices several theoretical model calculations have been developed and applied to different thruster configurations. The results of these calculations are compared with corresponding experimental arc devices and both agree well with each other. Concerning the plasma stability work, a new explanation of the so called "Onset Phenomenon" is presented. It is based on a run-away Joule heating effect caused by the self magnetic field of a current carrying plasma channel which drastically decreases the radial heatconduction losses due to the electrons. The dependency of the electron heatflux vector and heatconduction coefficient in a transverse magnetic field</p>		21 ABSTRACT SECURITY CLASSIFICATION	
20 DISTRIBUTION/AVAILABILITY OF ABSTRACT <input checked="" type="checkbox"/> UNCLASSIFIED/UNLIMITED <input checked="" type="checkbox"/> SAME AS RPT <input type="checkbox"/> DTIC USERS		22a NAME OF RESPONSIBLE INDIVIDUAL H. Kurtz	
22b TELEPHONE (Include Area Code) 202-767-4938		22c OFFICE SYMBOL NA	

DD Form 1473, JUN 86

Previous editions are obsolete.

SECURITY CLASSIFICATION OF THIS PAGE

(u)

19 ABSTRACT (Continue on reverse if necessary and identify by block number)

has been derived by means of a perturbation approach of the Maxwell distribution. Cathode erosion measurements have been conducted by means of a fully automatically working test rig. The cathode sample is repeatably charged by a fairly rectangular current pulse of 1400 A which lasts about 2 ms. Erosion rate measurements on thoriated (2%ThO₂) cathode samples are reported on and explained by a refined cathode spot theory.

Contents

1	Introduction	2
2	MPD - Code Development	4
2.1	The Nozzle Type MPD Thruster	4
2.1.1	Flow field code	5
2.1.2	Discharge code	6
2.1.3	Electron temperature code	7
2.1.4	Solution of the Equations	8
2.1.5	Discussion of Results	9
2.1.6	Conclusions	11
2.2	The Cylindrical MPD Thruster	12
2.2.1	Solution of the Equations	16
2.2.2	Numerical Results	16
2.2.3	Comparison with experimental results	30
3	Plasmastability	34
4	Electrode Effects	45
4.1	Cathode Experiments	45
4.2	Measurements	45
4.3	Conclusion and Explanation (qualitative)	53

5 List of Reports and Publications	57
6 Acknowledgements	60
A Appendices	62
A.1 Influence of the Magnetic Field on the Heatflux within an Electrically Charged Plasmacomponent	63
A.2 Determination of the Temperatureprofile within the Constrictor	70
Bibliography	78

List of Figures

1.1 Different MPD-Thruster Devices a) The Nozzle Type Thruster b) The Cylindrical Type Thruster	3
2.1 Thruster with the Calculation Areas. All length Coordinates are in [mm]	18
2.2 Magnetic Reynold's Number Distribution of the Three Different Throat Geometries for 2 kA and a Mass Flow of 0.8 g/s Argon. As Characteristic Length the Nozzle Diameter was Chosen.	19
2.3 Calculated Current Contour Lines of the Three Different Throat Geometries for 2 kA and a Mass Flow of 0.8 g/s Argon.	20
2.4 Electron Temperature Distribution of the Three Different Throat Geometries for 2 kA and a Mass Flow of 0.8 g/s.	21
2.5 Calculated and Measured Electron Temperature Profile for the Thruster with 24 mm Throat Diameter at a Current Level of 2 kA and a Mass Flow of 0.8 g/s.	22
2.6 Potential Lines of the Three Different Throat Geometries for 2 kA and a Mass Flow of 0.8 g/s.	23
2.7 Calculated and Measured Discharge Voltage	24
2.8 Comparison of Calculated and Measured Thrust for a Mass Flow of 0.8 g/s Argon $c_T = 1$	25
2.9 Calculated and Measured Arc Chamber Pressure	26
2.10 Density Maps a) with and b) without the Pinch Effect of the DT2 with Argon Discharge at 2 kA and a mass Flow of 0.8g/s	26
2.11 Calculation Grid of the ZT2-IRS Thruster.	27
2.12 Computation Scheme.	27
2.13 Magnetic Reynold's Number Distribution.	28

2.14	Calculated Current Contour Lines.	28
2.15	Measured a) and Calculated b) Current Contour Lines.	29
2.16	a) Heavy Particles and b) Electron Temperature Contours	32
2.17	Density Distribution.	33
2.18	Velocity Vector Distribution.	33
3.1	Illustration of the Self Magnetic Field within a Plasma Thruster	35
4.1	Scheme of Cathode Testrig	46
4.2	Testrig for Cathode Experiment	47
4.3	Typical Current vers. Time Curve	48
4.4	Measured Erosionrates in $\left[\frac{\mu g}{As}\right]$ as Funktion of the Accumulated Total Electric Charge in $[As]$ for Different Ambient Pressures. Each Measuring Point is the Result of 50 Current Pulses.(Cathode: Thoriated Tungsten at Room Temperature)	49
4.5	Erosion Rate as Funktion of the Accumulated Charge (Number of Current Pulses)	50
4.6	Asymptotic Erosion Rate as Funktion of the Ambient Pressure of a Tungsten Cathode in a Nitrogen Atmosphere Charged by a Rectangular Pulses of 1400 A for 2 ms (Pulsfrequency = $1-2 \text{ min}^{-1}$)	50
4.7	Massloss Due to Pure Heating in a Nitrogen and Argon Atmosphere ($p \leq 100Pa$)	51
4.8	Temperature of the heated probe ($\epsilon = 0.45$) as Funktion of the Heating Power	52
4.9	Scheme of a Spot Discharge	53
4.10	Illustration of the Plasmaflow around the Crater Rim with Prandtl-Meyer Deflection Angle, δ	54
A.1	Illustration of the Particle Motion within a Magnetic Induction Field, \vec{B} , normal to the Gradient, ∇f_i : (a) $\vec{V}_{i\perp}$ towards ∇f_i ; (b) $\vec{V}_{i\perp}$ opposite to ∇f_i (\vec{B} normal to plane).	66
A.2	Temperature Profile for Different Grades n of the Current Density Paraboloïdes within the Arc Core	76

A.3	Plot of γ as Funktion of \hat{T}_e and p as Parameter of Hydrogen as Propellant	77
A.4	Maximum Electrontemperature within an Hydrogen Arc Core as Function ot the Quotient $\frac{I}{r_c}$ (arc current divided by the core radius) for differnt pressure $p, n = 4, \xi = 0$.	77

List of Tables

2.1	Comparison of Numerical and Experimental Results for 2 g/s Argon at 6000 A	30
3.1	J2 according to eq.(3.12) and (3.13)	37
3.2	β for Hydrogen	38
3.3	β for Argon	38
3.4	β^* for Hydrogen	41
3.5	β^* for Argon	42
3.6	$\omega_e \tau_e$ -Values calculated for different Onset conditions at $n=2, 4, 10$ for Argon	44
3.7	$\omega_e \tau_e$ -values calculated for different Onset conditions at $n=2, 4, 10$ for Hydrogen	44
4.1	Erosionrate caused by arcing only at the surface of a heated tungsten (2% thoriated) cathode in a N_2 - atmosphere ($\leq 100Pa$) surface temperature: $\approx 1500K$	52
4.2	Prandel- Mayer Deflection δ for various pressure ratios $\frac{p_0}{p_*}$ and κ - values .	56
A.1	$J_0(n, \xi)$	72
A.2	$J_1(n, \xi)$	73

1. Introduction

Plasma propulsion systems are more advantageous than chemical propulsion systems according to their higher specific impulse rates and are more advantageous than ion engines based on their less complex design features. Plasma propulsion systems in form of arcjets are built in the range of about $0.1 - 0.2 N$ at a power of about $1 kW$ as station keeping devices and in a thrust range of about $1 - 2 N$ at 10 to $30 kW$ for drag compensation (means) and orbit maneuvering. With the advent of onboard nuclear power plants of $100kW$ electric and more high power arcjets and even MPD-thrusters in the range of up into the MW -range could offer substantial cost reduction or payload increase in space transportation and development.

The plasma thrusters which are considered here consist of coaxial electrode systems which support an electrical discharge within an axial gaseous propellant stream. The Joule heated gas or plasma is accelerated by thermal expansion and by self induced electromagnetic forces and depending on whether one or the other accelerating mechanism dominates, one may speak from arcjet- or MPD- thrusters. Indeed the most advanced plasma thruster and almost ready for space flight is the radiatively cooled $1 kW$ [1, 2, 3, 4] and the 15 to $30 kW$ arcjet with hydrazin or ammonia as propellant [5, 6, 7], the less advanced thrusters are the high power arcjets while MPD thrusters are currently investigated up into the several hundred kilowatt range in steady state mode [7] and within the megawatt range in pulsed mode [8, 9]. Despite of their simple designs the physical problems involved are complex and by no means fully understood.

The objective of this work is to locate and to investigate the still unknown effects within the flow discharge region concerning the heating, the acceleration, the loss mechanisms and the stability behavior of the arc discharge as well as the electrode attachment problematic within those plasma thrusters.

Several numerical model calculations have been developed which allow to determine the flow arc discharge region and the performance (thrust, specific impulse) of a nozzle type and a cylindrical MPD-thruster as a function of mass flow rate and electric current. They are described in chapter 2. In chapter 3 a new explanation of the "Onset" - Phenomenon (plasma stability effect in MPD thruster) is presented which is based on a "run away Joule heating" mechanism of the current carrying plasma channel. The results of this new theory are compared with experimental observations and are in very good agreement.

In chapter 4 electrode erosion effects were investigated experimentally and qualitatively explained by an improved spot theory.

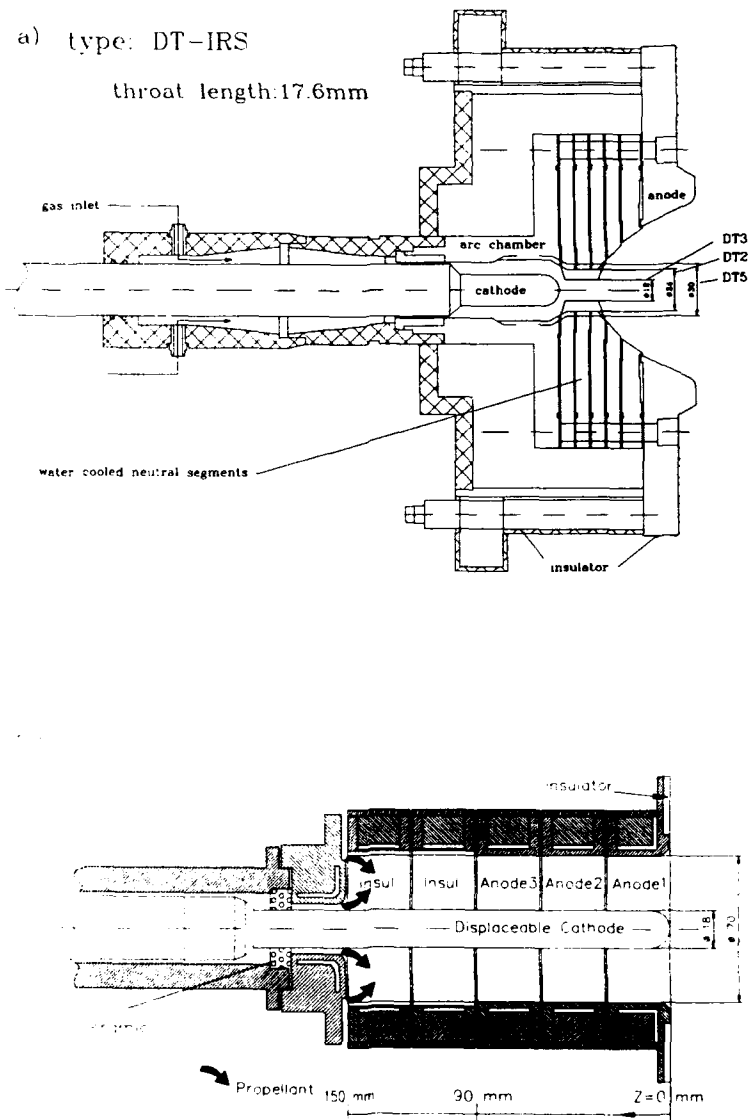


Figure 1.1: Different MPD-Thruster Devices a) The Nozzle Type Thruster b) The Cylindrical Type Thruster

2. MPD - Code Development

Based on the two different self magnetic MPD thruster designs a) the nozzle type and b) the cylindrical type thruster as shown in Fig. 1.1 a), b); two different MPD - codes have been developed and their results compared with experimental ones.

The main difficulties for developing a correct physical model and a numerical simulation are the following: no thermal equilibrium of the plasma, real gas effects, only partly known electrode effects, a not negligible friction due to the low Reynold's numbers caused by low densities and high temperatures, a magnetic Reynold's number too high to separate flow and discharge, etc. These are only the most important physical problems; added to them are the numerical difficulties: different sets of partial differential equation, namely elliptical and hyperbolic ones that have to be coupled, nonlinearities, steep gradients especially at the electrodes, difficult geometries, etc. This list is by no means a complete one.

Due to this complexity, great simplifications have to be made for all codes developed to investigate the MPD thrusters, so that they solve at least parts of the whole problem.

For investigating the flow and discharge fields and their interaction and effects on electric power, thrust and efficiency of the MPD thruster, numerical codes have been developed. These codes are one-dimensional [10], quasi-two-dimensional [11, 12] and simplified two-dimensional ones [13, 14, 15, 16].

2.1 The Nozzle Type MPD Thruster

In order to optimize the constrictor size to a given power and mass flow rate, three nozzle type thruster configurations (Fig 1.1 a) have been investigated experimentally in a wide power range and calculated by means of a semi two dimensional MPD - code. This code was developed to predict the overall performance of these thrusters and to prove the validity of this model approach by comparing the computed with the experimental results.

In this approach, the quasineutral part of the discharge is modeled, electrode effects are not included. For this purpose, independent codes for the discharge, the flow field and the electron temperature distribution have been installed and then solved iteratively [18].

The relatively low magnetic Reynold's number in the region of magnetic acceleration justifies these decoupled calculations.

The basic assumptions for all codes are steady state conditions, rotational symmetry and a fully singly ionized, quasi-neutral plasma.

2.1.1 Flow field code

The flow field is taken as a one-dimensional, frictionless expansion flow, assuming adiabatic behavior for the ions and isothermal for the electrons within the entire Nozzle. One assumes a fully ionized plasma and distinguishes between electron and ion temperatures and assumes a frozen flow within the thruster. Outside the thruster both components are assumed to be adiabatic. The results of the codes are compared with data from experiments performed within a vacuum tank which always has a residual gas pressure. Therefore, a free stream boundary is implemented corresponding to experiments with a similar thruster [19]. Outside the free stream boundary, see Fig. 2.1, the ambient gas mass density is, according to the experiments, set to $10^{-6} \frac{\text{kg}}{\text{m}^3}$ corresponding to a pressure of 0.1 Pa. At the free stream boundary a linear transition of the mass density over a distance of 30mm is implemented to avoid numerical problems by the solution of equation 2.12, caused by discontinuities.

The assumptions for the flow field code are: a one-dimensional frozen flow, an ambipolar expansion flow and no friction.

The basic equations are:

- Continuity Equation:

$$\rho v A = \dot{m} \quad (2.1)$$

- Bernoulli Equation:

$$v dv + \frac{1}{\rho} dp = 0 \quad (2.2)$$

- Equation of State:

- Within the thruster:

$$p = \frac{p_c}{2} \left(\left(\frac{\rho}{\rho_c} \right)^\kappa + \frac{\rho}{\rho_c} \right) \quad (2.3)$$

- Outside the thruster:

$$p = p_c \left(\frac{\rho}{\rho_c} \right)^\kappa \quad (2.4)$$

p_c and ρ_c are the chamber pressure and chamber density, respectively; they can be calculated from the nozzle throat condition.

Within the nozzle throat one assumes that all the ohmic heat input per unit arc length is dissipated radially by heat conduction. This assumption is quite reasonable, since the axial temperature gradient is much smaller than the radial one and since any heat input at the smallest cross sectional area cannot increase the velocity beyond the speed of sound. The radiation loss can be neglected, because within an MPD thruster the chamber and throat pressures are low.

A detailed evaluation of this energy balance within the nozzle throat, made in [18], yields the following equations for calculating the electron temperature within the nozzle

$$T_e = f \left(\frac{I}{r_t} \right)^{\frac{2}{3}} \quad (2.5)$$

where f is a slowly varying function depending on the current distribution.

The equation of state together with the continuity and Bernoulli equations yield the following expansion equations:

- inside the thruster:

$$\frac{\kappa}{\kappa - 1} \frac{p_c}{\rho_c} \left(\frac{\kappa - 1}{\kappa} \ln \left(\frac{\rho_c}{\rho} \right) + 1 - \left(\frac{\rho}{\rho_c} \right)^{\kappa - 1} \right) - \left(\frac{\dot{m}}{\rho A} \right)^2 = 0 \quad (2.6)$$

- outside the thruster:

$$v_{eo}^2 + \frac{2\kappa}{\kappa - 1} \frac{p_{eo}}{\rho_{eo}} \left(1 - \left(\frac{\rho}{\rho_{eo}} \right)^{\kappa - 1} \right) - \left(\frac{\dot{m}}{\rho A} \right)^2 = 0 \quad (2.7)$$

where v_{eo} , p_{eo} and ρ_{eo} are the values at the thruster nozzle exit.

The results of this flow field code are the axial velocity, pressure and density distribution.

After the first step of iteration of all codes, when the current density field is known, the pressure rise due to the pinch effect has been taken into account. This results in the pressure profile:

$$p(r) = p(R) - \int_R^r (\vec{j} \times \vec{B})_r dr \quad (2.8)$$

Together with the continuity equation, one obtains the density profile.

2.1.2 Discharge code

In order to calculate the current distribution of the arc discharge, a two-dimensional computer code has been developed.

The additional assumptions for the discharge code is the neglect of azimuthal current.

The basic equations for the discharge is the extended Ohm's law for plasmas:

$$\vec{j} = \sigma(\vec{E} + \vec{v} \times \vec{B}) - \frac{\omega\tau}{B}(\vec{j} \times \vec{B}) \quad (2.9)$$

Rewriting the Ohm's law by means of Maxwell's equations, one obtains a vector equation for the magnetic induction vector \vec{B} in the form

$$0 = \frac{1}{\mu_0}(\nabla \times (\frac{1}{\sigma} \nabla \times \vec{B}) - (\nabla \times (\vec{v} \times \vec{B})) + \frac{1}{\mu_0}(\nabla \times (\beta(\nabla \times \vec{B}) \times \vec{B})) \quad (2.10)$$

with

$$\beta = \frac{\omega\tau}{B_0\sigma} = \frac{1}{en_e} \quad (2.11)$$

From this equation follows with a stream function $\Psi = r B_\theta$ and with respect to the rotational symmetry and the zero azimuthal current the elliptical, partial differential equation of 2nd order

$$0 = \frac{\partial^2 \Psi}{\partial r^2} + \frac{\partial^2 \Psi}{\partial z^2} - \frac{\partial \Psi}{\partial r} \left(\frac{1}{r} + \frac{1}{\sigma} \frac{\partial \sigma}{\partial r} - \frac{\sigma \Psi}{r} \frac{\partial \beta}{\partial z} + \sigma \mu_0 v_r \right) - \frac{\partial \Psi}{\partial z} \left(\frac{1}{\sigma} \frac{\partial \sigma}{\partial z} + \frac{\sigma \Psi}{r} \frac{\partial \beta}{\partial r} - \frac{2\sigma \beta \Psi}{r^2} + \mu_0 \sigma v_z \right) - \sigma \mu_0 \Psi \left(\frac{\partial v_r}{\partial r} + \frac{\partial v_z}{\partial z} - \frac{v_r}{r} \right) \quad (2.12)$$

The function $\Psi(r, z) = \text{const}$ represents now a current contour line, since $B = B_\theta$ is proportional to $\frac{I(r)}{r}$, where $I(r)$ is the electric current carried through a cross sectional area of πr^2 . The proper boundary conditions for Ψ follow from the geometry of the thruster walls and electrodes. At the insulator inside the thruster and at the inflow boundary Ψ is set to $-\frac{\mu_0}{2\pi} I$. For the electrodes one assumes that the electric field is normal to the surfaces, therefore; $\vec{E} \cdot \vec{t} = 0$, where \vec{t} is the tangential vector of the electrodes surfaces in r-z plain. At the other boundary sections Ψ is set to 0.

2.1.3 Electron temperature code

The electron temperature has a strong effect on the electrical conductivity and the electron density, which again influences the discharge pattern. Therefore, a two-dimensional code for the electron temperature distribution, corresponding to the two-dimensional discharge code, has been written.

The electron temperature distribution is determined by the energy equation for the electron component.

$$\frac{j^2}{\sigma} = -\lambda_e \nabla \cdot T_e - \frac{5k}{2e} j \nabla T_e \quad (2.13)$$

The energy input due to ohmic heating equals the sum of losses given by the heat flux due to conduction and convection. The thermal conductivity λ_e depend on the electron temperature:

$$\lambda_e = 2.08 \frac{k^{\frac{3}{2}} \sqrt{T_e}}{\sqrt{m_e} Q_{ee}} \approx \lambda_{ec} T_e^{\frac{3}{2}} \quad (2.14)$$

where Q_{ee} is the Gvosdover cross section [19]

$$Q_{ee} = \frac{\pi}{4} \left(\frac{z_i e^2}{4\pi \epsilon_0 k T_e} \right)^2 \ln \left(1 + 144 \pi^2 \frac{\epsilon_0^3 T_e^3 k}{n_e e^6 (z_i^2 (z_i + 1))} \right) \quad (2.15)$$

With respect to the rotational symmetry, equations 2.13 - 2.15 result in the following elliptical, partial differential equation of 2nd order:

$$\begin{aligned} 0 = & \frac{j^2}{\sigma} + \left(\frac{\partial^2 T_e}{\partial r^2} + \frac{\partial^2 T_e}{\partial z^2} \right) \lambda_{ec} T_e^{\frac{3}{2}} \\ & + \left(\left(\frac{\partial T_e}{\partial r} \right)^2 + \left(\frac{\partial T_e}{\partial z} \right)^2 \right) \frac{5}{2} \lambda_{ec} T_e^{\frac{3}{2}} \\ & + \frac{\partial T_e}{\partial r} \left(\frac{\lambda_{ec} T_e^{\frac{3}{2}}}{r} + \frac{5k}{2e} T_e j_r \right) \\ & + \frac{\partial T_e}{\partial z} \left(\frac{5k}{2e} T_e j_z \right) \\ & + T_e \left(\frac{5k}{2e} T_e \frac{\partial j_r}{\partial r} + \frac{5k}{2e} T_e \frac{\partial j_z}{\partial z} + \frac{5k}{2e} \frac{1}{r} T_e j_r \right) \end{aligned} \quad (2.16)$$

The boundary condition for T_e along the free stream boundary is set to a value of 10000 K in accordance with the measurements [19]. Outside the free stream boundary the electron temperature is set to a constant value of 7000 K [19]. To avoid a discontinuity at the free stream boundary, a linear transition in radial direction is used. By using a value of 10000 K for the anode and the insulator one obtains reasonable results for the electron temperature inside the nozzle. The cathode is treated as a thermal insulator; therefore $\nabla T_e \cdot \vec{n} = 0$, where \vec{n} is the normal vector of the cathode surface. Due to the axial symmetry, $\frac{\partial T_e}{\partial r} = 0$ on the axis.

2.1.4 Solution of the Equations

The three models described above were solved in the following manner:

For a given flow field, the discharge equation and hence the electron temperature are determined. With these results, in the next iteration step, the flow field equations are calculated. This new flow field and the new distribution of the electron temperature have been taken to calculate the discharge equation, and so on. This iteration steps are repeated until the calculated datas, such as electron temperature distribution and current distribution have reached numerical equilibrium. Usually eight iterations are necessary to get good results.

The expansion relations 2.6 and 2.7 have been solved with the Newton method. The two nonlinear, elliptical, partial differential equations 2.12 and 2.17 are solved with the finite differential method. Figure 2.1 shows the thruster with the free stream boundary which divides the field into two areas. Area 1 and 2 is used as calculation area for Ψ , whereas only area 1 is used for T_e . These areas are discretized with a aquidistant finite differential grid of 1mm height (radial) and 2mm width (axial). The partial derivatives of 1st and 2nd order are replaced by the following differential quotients of any selective function $f(x)$

$$\frac{\partial f}{\partial x} = \frac{f_{x+1} - f_{x-1}}{2\Delta x} \quad (2.17)$$

$$\frac{\partial^2 f}{\partial x^2} = \frac{f_{x+1} - f_x + f_{x-1}}{\Delta x^2} \quad (2.18)$$

With this discretization, one obtains a nonlinear system of equations, which is iteratively solved with a modified Gauss-Seidel algorithm.

2.1.5 Discussion of Results

A main goal for developing this numerical code is to obtain better insight into the current distribution within a continuously running nozzle type MPD thruster. With that developed code, the three geometries as shown in Fig. 1.1a have been calculated.

With quasi-steady pulsed thrusters it is possible to measure the current contour lines, but it is not yet possible to compare these with experimental data on the continuously running thruster because of the high heat load of the probes. This means there is a need for a calculation code for the steady state thruster development.

The magnetic Reynold's number indicates if the discharge influences the flow field significantly. Therefore to evaluate the only weak coupling of flow and discharge within our iterative solution of the three codes, the magnetic Reynold's number $R_m = \mu_0 \sigma v L$ has been calculated. In Fig. 2.2 its distribution for the three throat geometries within the discharge region has been plotted, where as reference length the throat diameter was chosen. Since the main influence of the electromagnetic forces on the flow field occurs in the supersonic part, where the magnetic Reynold's number is fairly low, the decoupling of the flow field and the electromagnetic field model seems justified.

A comparison between calculated and measured current contour lines has been shown earlier [12]. The comparison shows fairly good agreement with the DT2 thruster configuration. In Fig. 2.3 the calculated current contour lines are shown for the different throat geometries at 2000 A with a mass flow of 0.8 g/s argon.

The electron temperature distribution within and outside the thruster at a current level of 2 kA is shown in Fig. 2.4. The maximums of the electron temperature in the symmetry axis are in the middle of the throat, because of the high current density there. The maximum electron temperatures are: 34 600 K for DT5, 37 700 K for DT2 and 51 100 K for DT3. The axial temperature profile is compared with experiments [19] in Fig. 2.5. The coincidence is fairly good. The reason for the lower calculated temperatures upstream is that the temperature boundary condition on the upstream flow boundary of 10000 K at a distance of 185 mm from the thruster end is too low compared with the experiment.

The potential lines within the discharge at 2 kA are plotted in Fig. 2.6. An integration across these lines yields the discharge voltage.

This calculated discharge voltage is compared with the measured voltage in the current range between 1 and 5 kA in Fig. 2.7.

With the measurements, in contrast to the calculation, the electrode fall voltages are included. In the case of the cathode this voltage drop equals about the work function of the cathode material, which means in the case of thoriated tungsten between 1 and 3 volts, and is nearly independent of the discharge current. The anode fall voltage depends strongly on the current; starting with several negative volts at currents up to about 3 kA, the anode voltage rises steeply in the onset region [10]. This explains the different behavior of the two curves at high currents and the fairly good agreement for currents between 1.5 and 3 kA. For DT3 it was not possible to measure with currents over 1.6 kA.

According to the flow conditions and the known electromagnetic force configuration, the thrust can be calculated. The thrust of an MPD thruster is the sum of all gas dynamic surface forces and the electromagnetic volume forces. Hence it is

$$\vec{T} = \int_{A_s} (\rho \vec{v}\vec{v} + \vec{P}) \cdot d\vec{A} - \int_V \vec{j} \times \vec{B} dV \quad (2.19)$$

where A_s represents the surface of all internal walls and V is the current carrying volume. The thermal loss to the wall of the thruster were neglected in this equation. Using the well-known method to match the gasdynamic effect by using a thrust coefficient c_T , where c_T is defined as

$$c_T = \frac{1}{p_c A_t} \int_{A_s} (\rho \vec{v}\vec{v} + \vec{P}) \cdot d\vec{A} \quad (2.20)$$

the absolute value of the thrust yields then

$$|\vec{T}| = c_T p_c A_t + \left| \int_V \vec{j} \times \vec{B} dV \right| \quad (2.21)$$

As it is shown in Fig. 2.8, one obtains for all three devices DT2, DT3 and DT5 a very good fit between measured and calculated thrust by taking a thrust coefficient of $c_T = 1$.

To improve the flow data at the upper flow boundary, which were calculated from the nozzle throat model, the calculated chamber pressure is compared with measurements carried out with DT2-IRS (Fig. 2.9). The very low deviation which is always less than 10 per cent is an indication of the validity of this model.

Since the pinch effect is a two-dimensional phenomenon and is applied here numerically on a one-dimensional flow model, numerical instabilities occur with currents higher than 3.5 kA at a mass flow of 0.8 g/s. These difficulties can only be overcome with a two-dimensional flow model. The results for 4 kA and higher were therefore calculated without accounting for the pinch effect. To evaluate the influence of the pinch effect on the discharge, a calculation was carried out with and without respect to the pinch effect at a current of 3 kA and a mass flow of 0.8 g/s argon for comparison with the results of the codes described above. No significant influence could be detected on the electron temperature distribution, the discharge voltage or the thrust. The influence on the current distribution is demonstrated in Fig. 2.10. The main difference is that with respect to the pinch effect the current is at the anode more concentrated at the nozzle end.

2.1.6 Conclusions

The presented numerical analysis has been applied to a rather complex nozzle type geometry. Despite the shortcomings of the code, namely the decoupled computation of the two dimensional electromagnetic and the one dimensional flow equations yields valuable results:

- Calculated integral values, such as thrust, discharge voltage and discharge chamber pressure fit the measured ones very well.
- The current patterns of the discharge and the electron temperature coincide with the measured data fairly well.

Further steps to improve the method will be a refinement of the flow field code to two-dimensionality and the inclusion of chemical reactions to overcome the restriction of a fully singly ionized gas assumption.

2.2 The Cylindrical MPD Thruster

A new fully two - dimensional axissymmetric code has been developed in which the gas dynamic equations are solved by the finite volume code EULFLEX [21] The electromagnetic discharge equation and the electron energy equation are transformed into curvilinear coordinates and solved under steady state conditions by a modified Gauss-Seidel algorithm.

In order to weigh the suitability of that code, it is used to investigate the cylindrical MPD thruster (Fig. 1.1 b), which is investigated experimentally at the IRS in a steady state as well as in a quasistationary pulsed mode.

All geometrical configuration parameters on which the computation is based on were chosen in accordance with the experimental device. A transformation to curvilinear coordinates allows a calculation of a complex, two-dimensional geometry. Fig. 2.11 shows a grid of those calculations for the cylindrical thruster . The propellant used in the calculation code is argon.

The two-dimensional numerical code is based on a finite volume method for flow calculations,[21] and the Gauss-Seidel method for the electromagnetic discharge[11, 21] and the electron energy equation[23, 24].

In addition to the geometry of the thruster, the code requires the mass flow rate and the electric current as input data, at the starting point the heavy particles temperature and Mach number, and as an input from the experimental investigations the boundary values of the electron temperature. This yields the following results: flow, electron- and heavy particles temperature distribution, pressure distribution, velocity, Mach number distribution, magnetic field, current density distribution and the electromagnetic and electrothermal thrust.

In order to calculate the current distribution of the arc discharge, a two-dimensional computer code has been developed. Additional assumptions for the discharge code are the neglect of azimuthal current.

The basic equation for the discharge is the extended Ohm's law for plasmas:

$$\vec{j} = \sigma(\vec{E} + \vec{v} \times \vec{B}) - \frac{\omega_e \tau_e}{B}(\vec{j} \times \vec{B}) \quad (2.22)$$

Rewriting the Ohm's law by means of Maxwell's equations, one obtains a vector equation for the magnetic induction vector \vec{B} in the form

$$0 = \frac{1}{\mu_0}(\nabla \times (\frac{1}{\sigma} \nabla \times \vec{B}) - (\nabla \times (\vec{v} \times \vec{B})) + \frac{1}{\mu_0}(\nabla \times (\beta(\nabla \times \vec{B}) \times \vec{B})) \quad (2.23)$$

with

$$\beta = \frac{\omega \tau}{B \sigma} = \frac{1}{en_e} \quad (2.24)$$

With the Jacobian J of the transformation from cylindrical to the curvilinear coordinates:

$$J = \frac{1}{\frac{\partial z}{\partial \xi} \frac{\partial r}{\partial \eta} - \frac{\partial z}{\partial \eta} \frac{\partial r}{\partial \xi}} \quad (2.25)$$

where the matrices are formed in terms of the derivatives of the cylindrical coordinates as follows:

$$\begin{aligned} \xi_z &= J \frac{\partial r}{\partial \eta}, & \eta_z &= -J \frac{\partial r}{\partial \xi} \\ \xi_r &= -J \frac{\partial z}{\partial \eta}, & \eta_r &= J \frac{\partial z}{\partial \xi} \end{aligned} \quad (2.26)$$

where the convention $\xi_z = \frac{\partial \xi}{\partial z}$, etc. is used.

The equation (2.23) follows with a stream function $\Psi = r B_\theta$ the elliptical, partial differential equation of 2nd order

$$\begin{aligned} & \frac{\partial^2 \Psi}{\partial \xi^2} (\xi_z^2 + \xi_r^2) + 2 \frac{\partial^2 \Psi}{\partial \xi \partial \eta} (\xi_z \eta_z + \xi_r \eta_r) + \frac{\partial^2 \Psi}{\partial \eta^2} (\eta_z^2 + \eta_r^2) \\ & + \frac{\partial \Psi}{\partial \xi} \left\{ \xi_z \frac{\partial \xi_z}{\partial \xi} + \eta_z \frac{\partial \xi_z}{\partial \eta} + \xi_r \frac{\partial \xi_r}{\partial \xi} + \eta_r \frac{\partial \xi_r}{\partial \eta} \right. \\ & \quad + \xi_z \left[-\frac{1}{\sigma} \left(\xi_z \frac{\partial \sigma}{\partial \xi} + \eta_z \frac{\partial \sigma}{\partial \eta} \right) - \right. \\ & \quad \quad \left. \frac{\sigma \Psi}{R} \left(\xi_r \frac{\partial \beta}{\partial \xi} + \eta_r \frac{\partial \beta}{\partial \eta} \right) + \frac{2\sigma \beta \Psi}{R^2} - \sigma \mu_0 u \right] \\ & \quad + \xi_r \left[-\frac{1}{R} - \frac{1}{\sigma} \left(\xi_r \frac{\partial \sigma}{\partial \xi} + \eta_r \frac{\partial \sigma}{\partial \eta} \right) + \right. \\ & \quad \quad \left. \frac{\sigma \Psi}{R} \left(\xi_z \frac{\partial \beta}{\partial \xi} + \eta_z \frac{\partial \beta}{\partial \eta} \right) - \sigma \mu_0 v \right] \left. \right\} \\ & + \frac{\partial \Psi}{\partial \eta} \left\{ \xi_z \frac{\partial \eta_z}{\partial \xi} + \eta_z \frac{\partial \eta_z}{\partial \eta} + \xi_r \frac{\partial \eta_r}{\partial \xi} + \eta_r \frac{\partial \eta_r}{\partial \eta} \right. \\ & \quad + \eta_z \left[-\frac{1}{\sigma} \left(\xi_z \frac{\partial \sigma}{\partial \xi} + \eta_z \frac{\partial \sigma}{\partial \eta} \right) - \right. \\ & \quad \quad \left. \frac{\sigma \Psi}{R} \left(\xi_r \frac{\partial \beta}{\partial \xi} + \eta_r \frac{\partial \beta}{\partial \eta} \right) + \frac{2\sigma \beta \Psi}{R^2} - \sigma \mu_0 u \right] \\ & \quad + \eta_r \left[-\frac{1}{R} - \frac{1}{\sigma} \left(\xi_r \frac{\partial \sigma}{\partial \xi} + \eta_r \frac{\partial \sigma}{\partial \eta} \right) + \right. \\ & \quad \quad \left. \frac{\sigma \Psi}{R} \left(\xi_z \frac{\partial \beta}{\partial \xi} + \eta_z \frac{\partial \beta}{\partial \eta} \right) - \sigma \mu_0 v \right] \left. \right\} \\ & + \sigma \mu_0 \Psi \left(\frac{v}{R} - \frac{\partial U}{\partial \xi} - \frac{\partial V}{\partial \eta} \right) = 0 \end{aligned} \quad (2.27)$$

with U and V as the contravariant velocities

$$\begin{aligned} U &= \xi_z u + \xi_r v \\ V &= \eta_z u + \eta_r v \end{aligned} \quad (2.28)$$

The function $\Psi(r, z) = \text{const}$ now represents a current contour line, since $B = B_\theta$ is proportional to $\frac{I(r)}{R}$, where $I(r)$ is the electric current carried through a cross sectional area of πr^2 . The proper boundary conditions for Ψ follow from the geometry of the thruster walls and electrodes. At the insulator inside the thruster and at the inflow boundary Ψ is set to $-\frac{\mu_0}{2\pi} I$. For the electrodes the electric field is assumed to be normal to the surfaces $\vec{E} \cdot \vec{t} = 0$. In accordance with the grid in Fig. 2.11 it is equal to $E_{/xi} = 0$, and it follows to:

$$\begin{aligned} \frac{\partial \Psi}{\partial \eta} \left[\frac{\beta \Psi}{R} (\xi_r \eta_r - \xi_z \eta_z) + \frac{1}{\sigma} (\xi_z \eta_r - \xi_r \eta_z) \right] + \\ \frac{\partial \Psi}{\partial \xi} \frac{\beta \Psi}{R} (\xi_r^2 - \xi_z^2) + \mu_0 \Psi (\xi_r u - \xi_z v) = 0 \end{aligned} \quad (2.29)$$

At the other boundary sections and at the symmetry axis Ψ is set to 0.

The electron temperature has a strong effect on the electrical and thermal conductivity and on the electron density, which again influences the discharge pattern. Therefore, a two-dimensional code for the electron temperature distribution, corresponding to the two-dimensional discharge code, was written.

The electron temperature distribution is determined by the energy equation for the electron component.

$$\begin{aligned} \nabla(\lambda_e \nabla T_e) + \frac{5}{2} \frac{k}{e} \vec{j} \nabla T_e = \\ \frac{\vec{j}^2}{\sigma} - \sum_{\nu} n_{\nu} n_e \alpha_{e\nu} (T_e - T_{\text{rot}}) - \epsilon_{\text{ion}} \cdot \frac{\partial n_e}{\partial t} \Big|_{\text{rct}} \end{aligned} \quad (2.30)$$

The first term on the left hand side represents the heat flux of the electron gas due to conduction, and the second term gives the convective change of the electron gas energy. The energy input due to ohmic heating is represented by the first term on the right hand side. The sum of losses due to the energy transfer from the electron gas to the heavy particles gas is calculated by the second term on the right hand side. The reaction losses are given by the last term, where ϵ_{ion} is given by Unsöld.[25]

The heat transfer coefficient $\alpha_{e\nu}$ and the thermal conductivity λ_e depend on the electron temperature [23, 28], where the heat transfer coefficient follows by

$$\alpha_{e\nu} = \frac{8\sqrt{2}}{\sqrt{\pi}} Q_{e\nu} \sqrt{\mu_{e\nu} k T_{e\nu}} \frac{k}{m_e + m_{\nu}} \quad (2.31)$$

and the thermal conductivity by

$$\lambda_e = \frac{15}{8} \sqrt{\frac{\pi}{2}} \frac{n_e k^2 T_e}{\sum_{\nu(e)} n_{\nu} Q_{e\nu} \sqrt{m_{e\nu} k T_{e\nu}}} \quad (2.32)$$

where for Q_{ee} and for $Q_{e\nu}$ with $\nu = \text{ions}$ the Gvosdover cross section[26] is taken, and with $\nu = \text{atoms}$ the Ramsauer cross section is applied.[27]

With respect to the rotational symmetry, equation 2.30 results in the following elliptical, partial differential equation of 2nd order:

$$\begin{aligned} & \alpha \frac{\partial^2 T_e}{\partial \xi^2} + 2\beta \frac{\partial^2 T_e}{\partial \xi \partial \eta} + \gamma \frac{\partial^2 T_e}{\partial \eta^2} + \\ & \frac{J^2}{4\lambda_{ec} T_e^{5/2}} \left[\sum_{\nu} n_e n_{\nu} \alpha_{e\nu} (T_{\nu} - T_e) + \right. \\ & \left. \frac{\tilde{J}^2}{\sigma} - \epsilon_{ion} \cdot \left(u \frac{\partial n_{e,rcr}}{\partial \xi} + v \frac{\partial n_{e,rcr}}{\partial \eta} \right) - \right. \\ & \left. \frac{n_e k T_e}{J} (r_{\eta} u_{\xi} - r_{\xi} u_{\eta} + z_{\xi} v_{\eta} - z_{\eta} v_{\xi}) - \right. \\ & \left. \frac{3n_e k}{2J} \left(u r_{\eta} \frac{\partial T_e}{\partial \xi} - u r_{\xi} \frac{\partial T_e}{\partial \eta} + v z_{\xi} \frac{\partial T_e}{\partial \eta} - v z_{\eta} \frac{\partial T_e}{\partial \xi} \right) \right] \\ & - \sigma \frac{\partial T_e}{\partial \eta} - \tau \frac{\partial T_e}{\partial \xi} = 0 \end{aligned} \quad (2.33)$$

Here ξ and η indicate the partial differentiation to the curvilinear ξ - and η -directions. $\alpha, \beta, \gamma, \sigma, \tau$ are metric terms and J is the Jacobian of the transformation.

At the outflow boundary T_e is set to a value in accordance with measurements[19]. Inside, the solid bodies of the thruster are treated as thermal insulators; therefore $\nabla T_e \cdot \vec{n} = 0$, where \vec{n} is the normal vector of the surfaces. Due to the axial symmetry, $\frac{\partial T_e}{\partial r} = 0$ on the axis. At the inflow boundary T_e is set to a constant value of 7000 K in accordance with the measurements.

For the description of the two-dimensional, axisymmetric flow, the following nonlinear hyperbolic system of differential equations with curvilinear, cylindrical coordinates is used.

$$\frac{\partial}{\partial t} \vec{q} + \frac{\partial}{\partial \xi} \vec{F}(\vec{q}) + \frac{\partial}{\partial \eta} \vec{G}(\vec{q}) + \vec{H}(\vec{q}) = 0 \quad (2.34)$$

The indices t, ξ, η indicate the partial differentiation with respect to time and to the ξ - and η -directions.

The first three terms are used in the usual fluid dynamic manner, where \vec{q} is the flow variables vector and \vec{F} and \vec{G} are the spatial derivatives vectors.[21] The source vector \vec{H} is developed to:

$$\vec{H}(\vec{q}) = \begin{bmatrix} \rho v / R \\ \rho u v / R + \frac{\partial}{\partial \xi} \left\{ \mu \left[2 \frac{\partial U}{\partial \xi} + \left(\frac{\partial V}{\partial \xi} + \frac{\partial U}{\partial \eta} \right) \right] \right\} + j_{\eta} B_{\theta} \\ \rho v^2 / R + \frac{\partial}{\partial \eta} \left\{ \mu \left[2 \frac{\partial V}{\partial \eta} + \left(\frac{\partial U}{\partial \eta} + \frac{\partial V}{\partial \xi} \right) \right] \right\} + j_{\xi} B_{\theta} \\ (p + e) v / R + \nabla \vec{q}_s - \sum_{\nu} n_{\nu} n_e \alpha_{e\nu} (T - T_e) \end{bmatrix} \quad (2.35)$$

The first terms in the source vector transform the plane two-dimensional into a cylindrical calculation. The first additional terms in the impulse equations represent the stress

tensor of the plasma flow, where the viscosity coefficient μ is given by:

$$\mu = \frac{3}{8} \sqrt{\frac{\pi}{2}} \sum_l \frac{m_l n_l k T_l}{\sum_{\nu(=l)} n_\nu Q_{l\nu} \sqrt{m_{l\nu} k T_{l\nu}}} \quad (2.36)$$

The last terms in the impulse equations represent the $\vec{j} \times \vec{B}$ forces from the electromagnetic field. In the energy equation the second source vector term \vec{q}_s represents the heat flux vector due to the heavy particles of the MPD flow, which is given by [28]:

$$\vec{q}_s = \sum_l -\lambda_l \left(\frac{1}{2} \frac{T_l}{n_l} \nabla n_l + \nabla T_l \right) \quad (2.37)$$

Here the heat conductivity coefficients are given by:

$$\lambda_l = \frac{15}{8} \sqrt{\frac{\pi}{2}} \frac{n_l k^2 T_l}{\sum_{\nu(=l)} n_\nu Q_{l\nu} \sqrt{m_{l\nu} k T_{l\nu}}} \quad (2.38)$$

The transfer of Joules heat is contained in the temperature exchange between the electron and the heavy particle temperature, which is represented by $\sum n_\nu n_e \alpha_{e\nu} (T_e - T)$ in the equation of energy conservation.

The transport coefficients are derived more detail in [28]. The cross sections $Q_{l\nu}$ for all coefficients are taken from the references.[26, 27].

2.2.1 Solution of the Equations

The three models described in the subsection above are solved in the following manner:

For a given flow field, the discharge equation and hence the electron temperature is determined. With these results the flow field equations are calculated. This new flow field and the new distribution of the electron temperature are used to calculate the discharge equation, and so on (see Fig. 2.12). These iteration steps are repeated until the calculated datas, such as electron temperature distribution, current distribution and the heavy particles flow field, have reached numerical equilibrium.

The extended Euler equations which determine the heavy particles flow, are solved by the finite volume method EUFLEX.[21] The two nonlinear, elliptical, partial differential equations 2.27 and 2.33 are solved with a Gauss-Seidel finite difference method.

2.2.2 Numerical Results

The magnetic Reynold's number in Fig. 2.13 is based on the distance between the electrodes. It indicates if the induced magnetic field influences the flow field significantly. In Fig. 2.13 one can see that the magnetic Reynold's number increases only at the end of the cathode to 1.1; in the greater part of the discharge area it is considerably lower

then 1. Therefore the weakly coupled calculation of flow and discharge as performed here leads to fairly good results.

The flow inlet boundary conditions were iterated to coincide with an experimentally obtained cold gas thrust of 1 N at a mass flow rate of 2 g/s . For a given current of 6 kA the computation yields the current contour lines, as illustrated in Fig. 2.14.

This calculated current distribution corresponds to that of a continuously running thruster in which the cathode is hot glowing and emits sufficient electrons along its entire length.

In case of pulsed thruster with cold cathode the arc preferably touches the cathode root, therefore the current contour distribution is not comparable with the case of the continuing mode. Unfortunately it is only possible with quasi-steady pulsed thrusters to measure the current contour lines. Due to the high heat load to the probe it is not yet possible to compare the calculated with the experimental data on the continuously running thruster. In order to verify the calculation procedure, an experiment with a withdrawn cathode was carried out, since here the arc attachment is closer to the top of the cathode also in case of a quasi steady state mode. In that case it means there is a need for a calculation and measurement with a short cathode, because in that position the current has hardly any space to move, and the cathode attachment of the arc during a measurement is well defined. This promises a better correspondence with the calculations.

Due to a limitation of the pulsed power supply a comparison between measured and calculated current contour lines has been done only at 3000 A for a cathode position of 30 mm (see Fig 2.15). For this condition, however, the comparison is not quite appropriate, since the difference between pulsed and steady state thrusters is much more distinct for the cylinder type thruster than for the nozzle type thruster. In the experiment the current touches mainly the upstream area of the cathode whereas the calculation results in a stronger current concentration at the tip of the cathode. These different current distributions on the cathode cause a more downstream current on the anode for the calculated case than in the experiment.

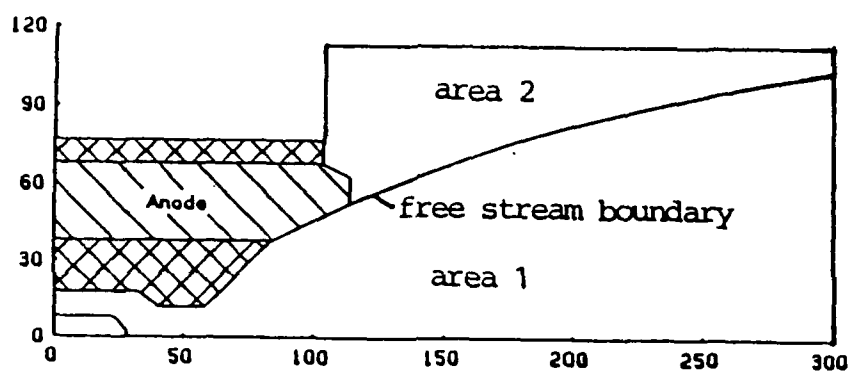


Figure 2.1: Thruster with the Calculation Areas. All length Coordinates are in [mm]

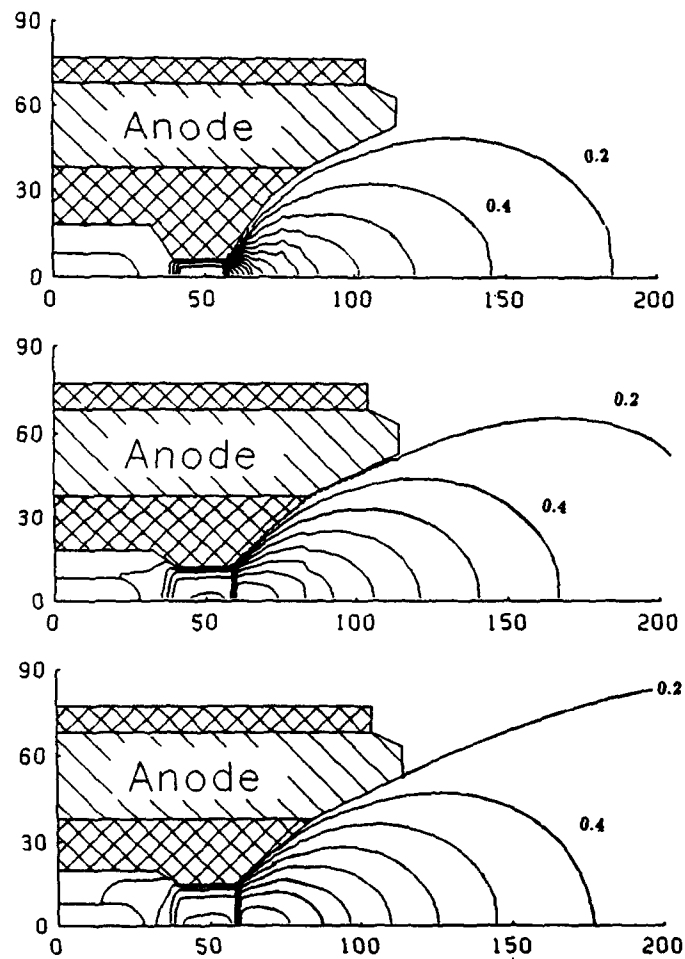


Figure 2.2: Magnetic Reynold's Number Distribution of the Three Different Throat Geometries for 2 kA and a Mass Flow of 0.8 g/s Argon. As Characteristic Length the Nozzle Diameter was Chosen.

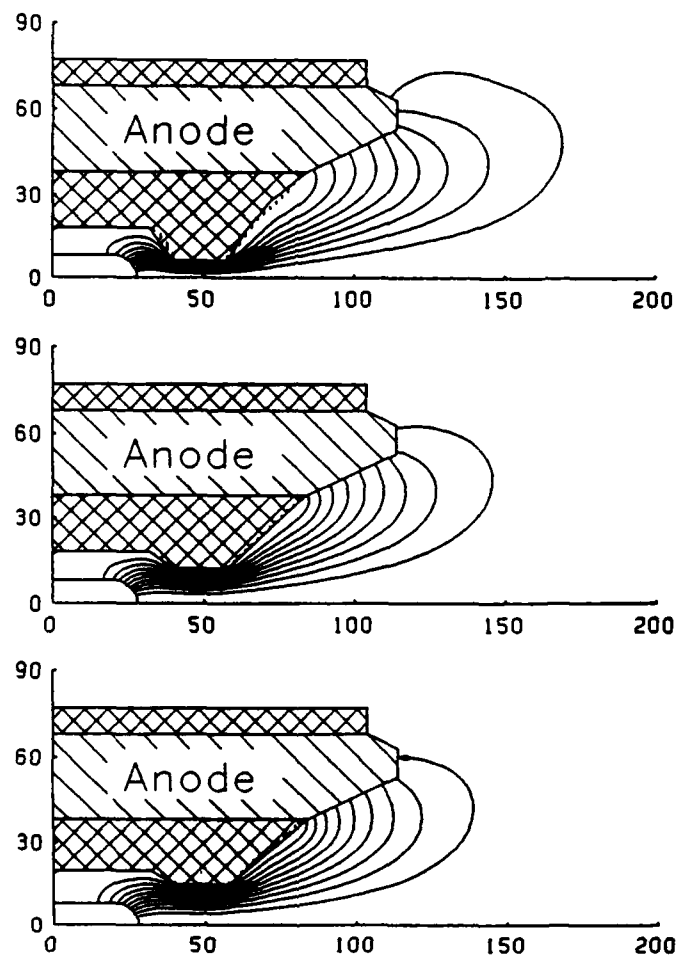


Figure 2.3: Calculated Current Contour Lines of the Three Different Throat Geometries for 2 kA and a Mass Flow of 0.8 g/s Argon.

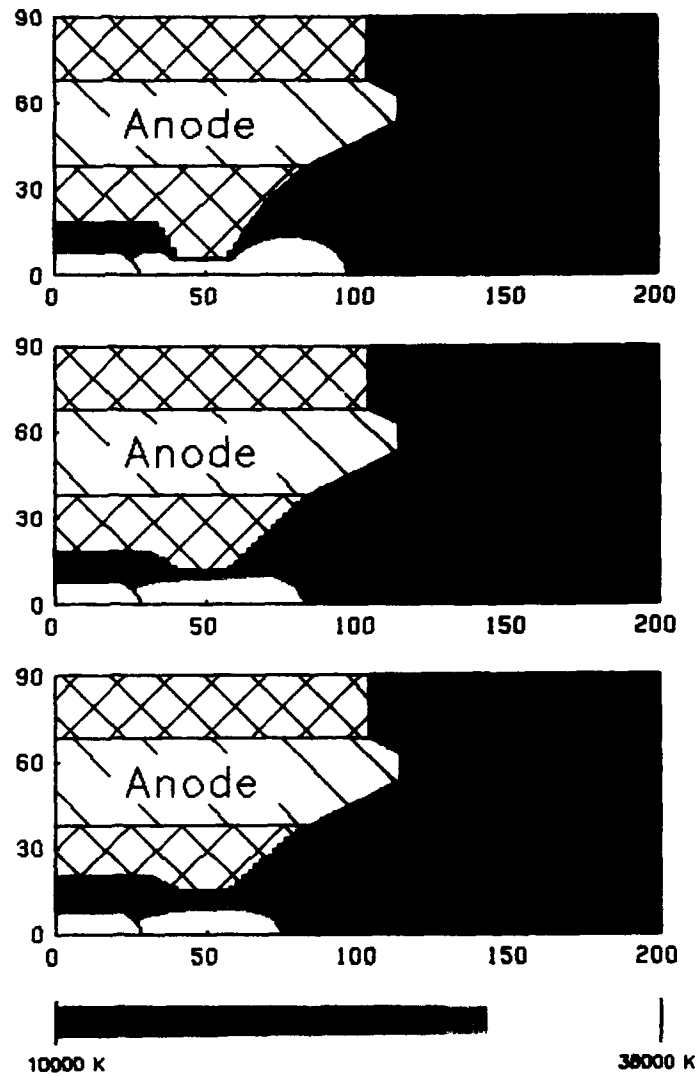


Figure 2.4: Electron Temperature Distribution of the Three Different Throat Geometries for 2 kA and a Mass Flow of 0.8 g/s.

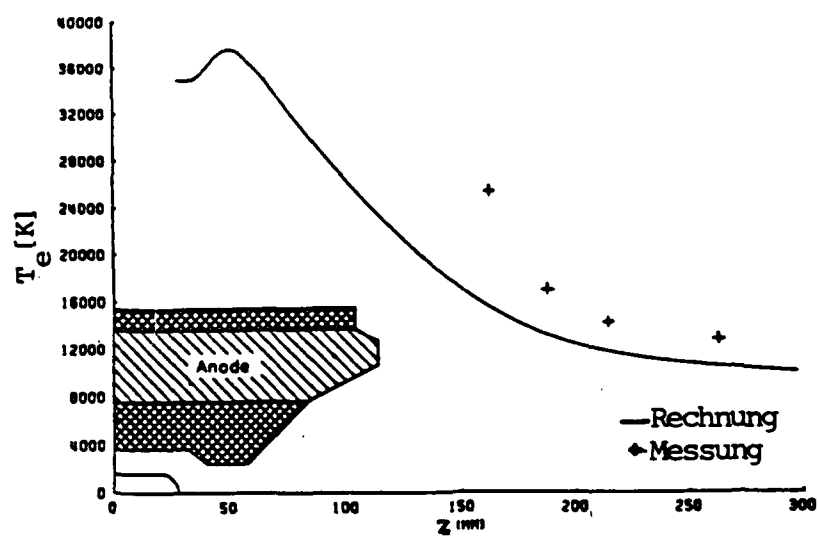


Figure 2.5: Calculated and Measured Electron Temperature Profile for the Thruster with 24 mm Throat Diameter at a Current Level of 2 kA and a Mass Flow of 0.8 g/s.

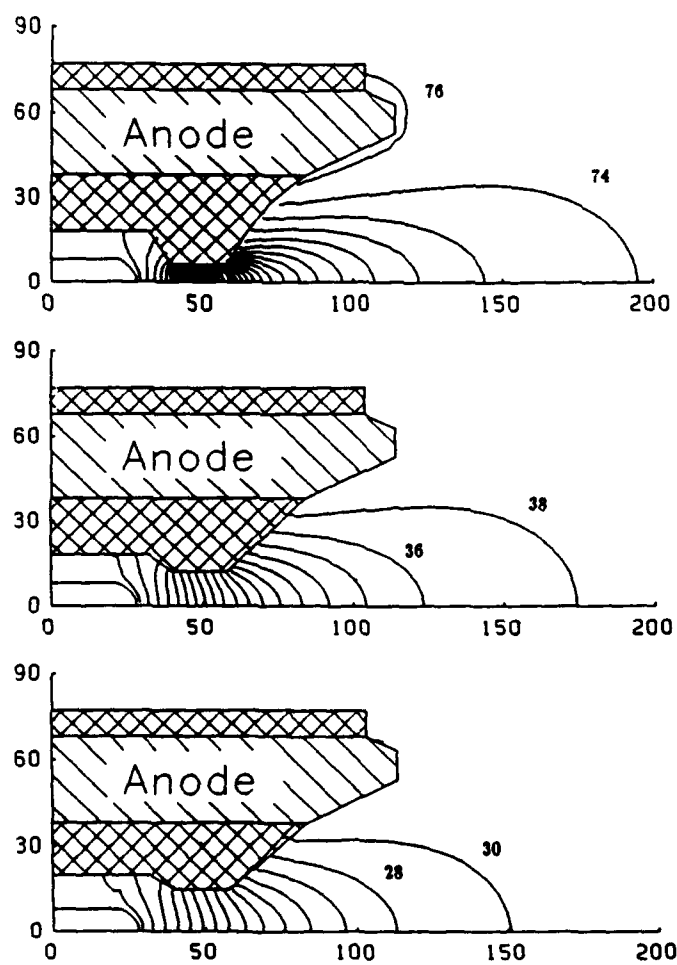


Figure 2.6: Potential Lines of the Three Different Throat Geometries for 2 kA and a Mass Flow of 0.8 g/s.

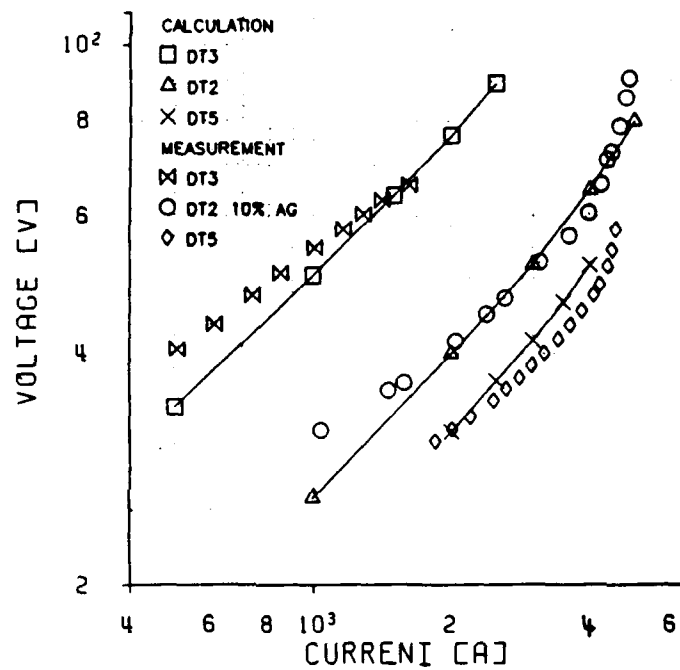


Figure 2.7: Calculated and Measured Discharge Voltage

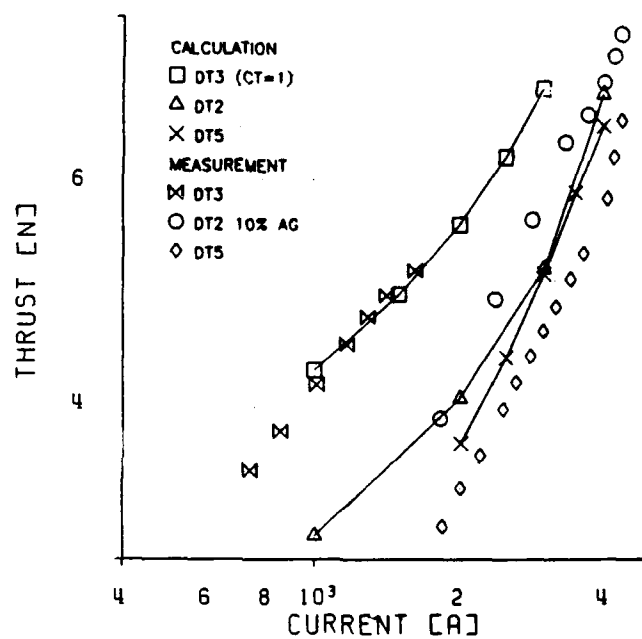


Figure 2.8: Comparison of Calculated and Measured Thrust for a Mass Flow of 0,8 g/s Argon $c_T = 1$

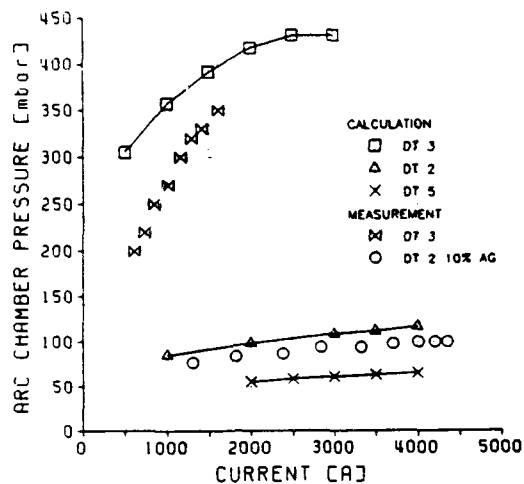


Figure 2.9: Calculated and Measured Arc Chamber Pressure

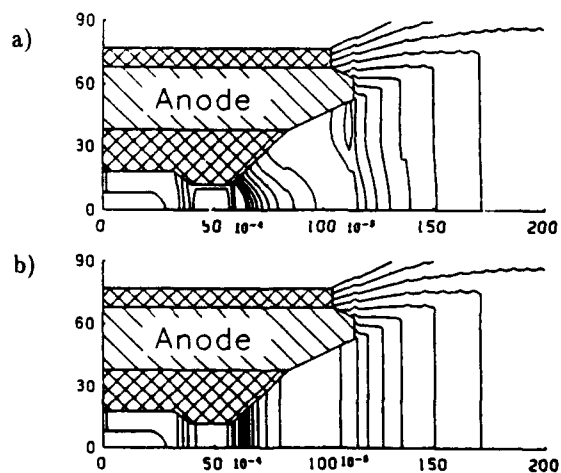


Figure 2.10: Density Maps a) with and b) without the Pinch Effect of the DT2 with Argon Discharge at 2 kA and a mass Flow of 0.8g/s

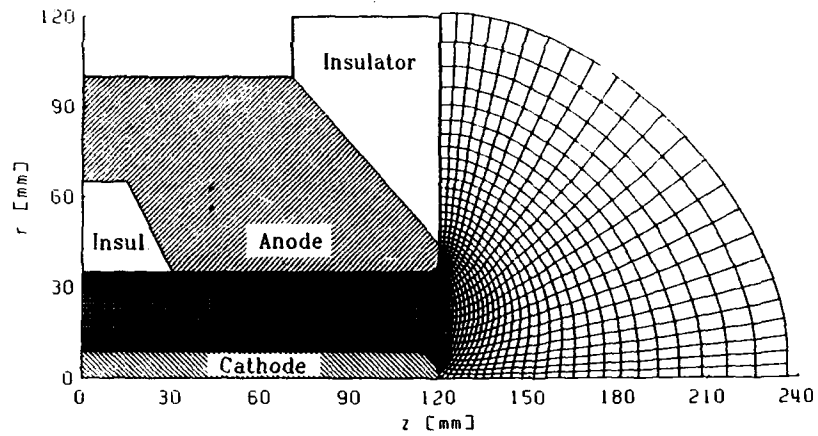


Figure 2.11: Calculation Grid of the ZT2-IRS Thruster.

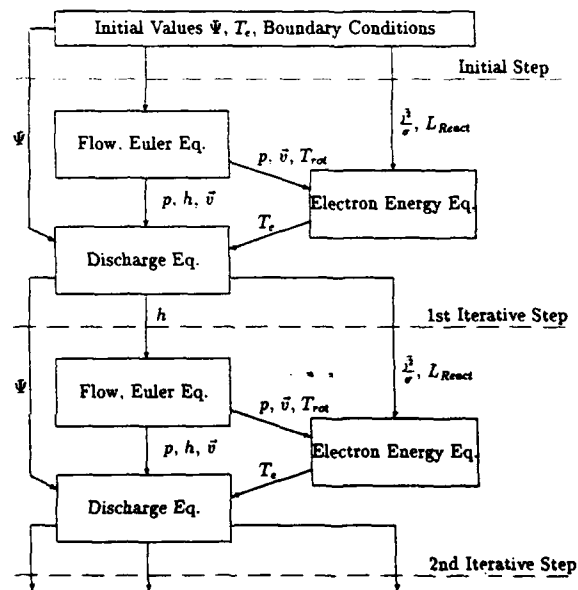


Figure 2.12: Computation Scheme.

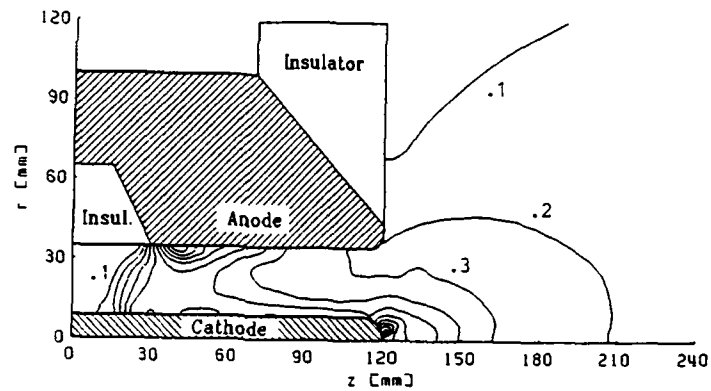


Figure 2.13: Magnetic Reynold's Number Distribution.

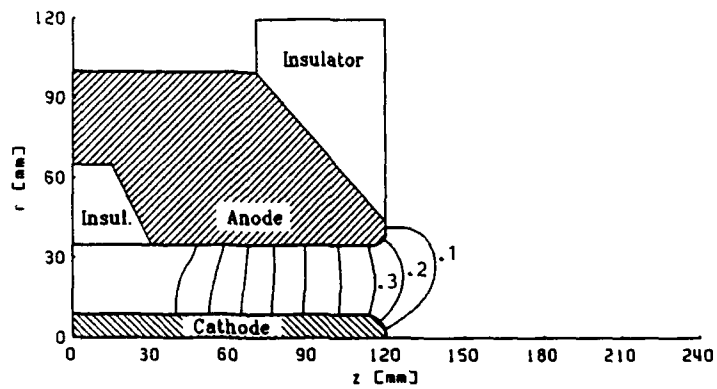


Figure 2.14: Calculated Current Contour Lines.

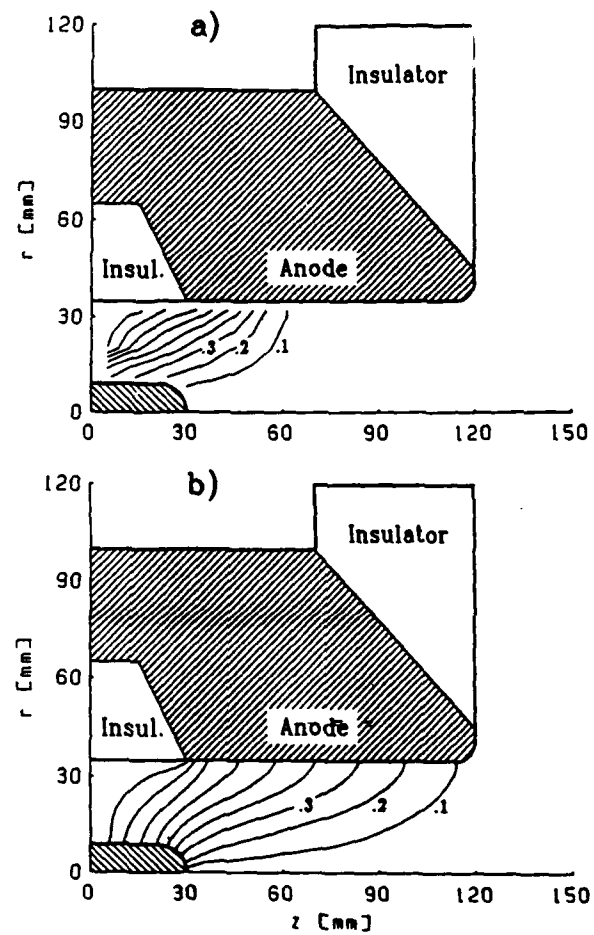


Figure 2.15: Measured a) and Calculated b) Current Contour Lines.

The heavy particle (a) and the electron temperature distribution (b) within and outside the thruster is shown in Fig. 2.16. The maximum temperature value of the heavy particles and of the electrons is near the tip of the cathode, but there is also a remarkable increase of the electron temperature at the upstream side of the anode.

The density map (Fig. 2.17) demonstrates the expansion flow, where the relatively low pinch effect has been taken into account.

The relation of the velocity distribution to the temperatures and density distribution is shown in Fig. 2.18 as a vector graph. It shows a high increase from the inflow boundary downstream. The radial velocity components inside the channel are quite small, which is also an indication for a relatively low pinch effect there.

According to the flow conditions and the known electromagnetic force configuration, the thrust can be calculated. The thrust of an MPD thruster is the sum of all gas dynamic surface forces and the electromagnetic volume forces. Hence it is

$$\vec{T} = \int_{A_s} (\rho \vec{v}\vec{v} + \vec{P}) \cdot d\vec{A} - \int_{V_c} \vec{j} \times \vec{B} dV_c \quad (2.39)$$

where A_s represents the surface of all internal walls and V_c is the current carrying volume. For the case presented here the total thrust was calculated without any losses as 14.4 N. This includes the portion of 5.1 N electromagnetic thrust and the portion of 1 N cold gas thrust.

2.2.3 Comparison with experimental results

As can be seen in Fig. 1.1b the anode of the cylindrical thruster is divided into three segments of 30 mm width. The current in each of the segments is measured separately during the experiment.

	Percentual Current Fraction into Anode Segments			Discharge Voltage
	Anode 1	Anode 2	Anode 3	
Theory	49 A	29 A	22 A	13 V
Experiment	62 A	25 A	13 A	18 V

Table 2.1: Comparison of Numerical and Experimental Results for 2 g/s Argon at 6000 A

The measured data of table 2.1 agree well with the numerical results of Fig 2.14. For example, the experimentally determined current percentage are 62% of the total for the downstream anode segment, 25% for the middle, and 13% for the upstream section. This must be compared with the theoretical percentage of 49%, 29% and 22%. The measured voltage drop was 18 V, whereas the calculation gave a somewhat lower figure of 13 V. Since the numerical model does not include electrode fall voltages, the resulting number matches the experiment quite well.

The code described in this paper was developed and tested in order to gain a more profound understanding of the fundamental processes occurring in MPD thrusters and in order to end up with reliable design criteria and predictions of thruster performances under various conditions. With the curvilinear grid, the code permits a more approximated simulation of geometry dependencies. Thus, better data are obtained for the calculation results with the cylindrical thruster design. In a later research period also the nozzle type thruster designs will be investigated with the curvilinear code.

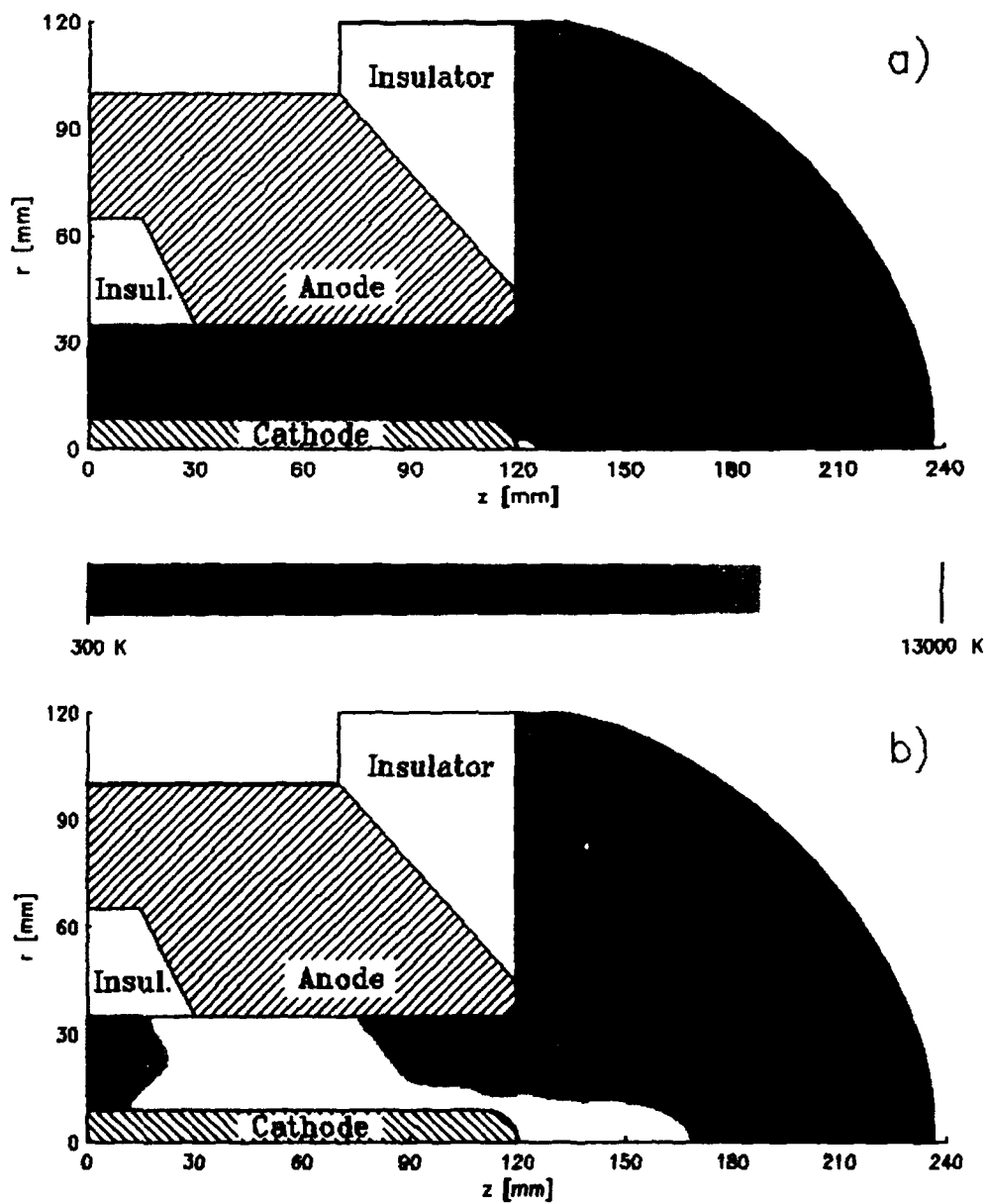


Figure 2.16: a) Heavy Particles and b) Electron Temperature Contours

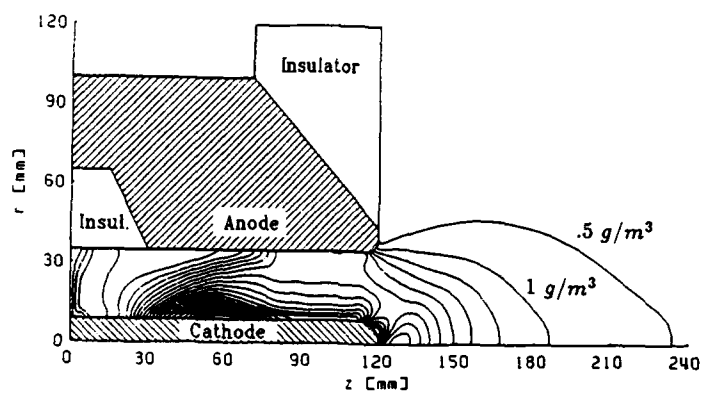


Figure 2.17: Density Distribution.

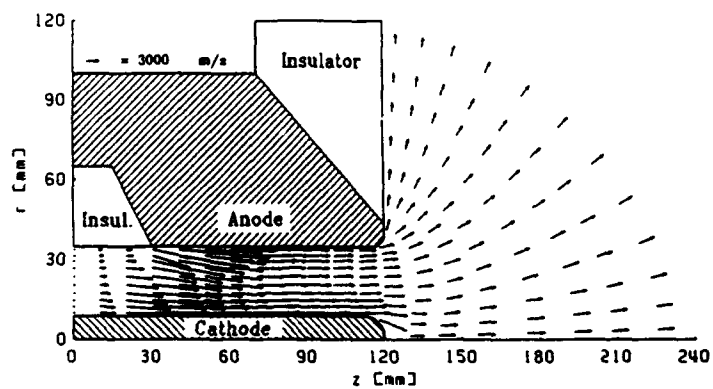


Figure 2.18: Velocity Vector Distribution.

3. Plasmastability

The plasmastability within a self magnetic MPD – thruster has been or is being investigated experimentally and theoretically many times. One of the most crucial limiting effects of these thrusters turns out to be the so called "Onset" phenomenon [31, 32, 33, 34], a plasmainstability which causes a severe degradation of the thruster performance. Several different explanations [35, 36, 37, 38, 39] have been put forward so far and their analytical results agree for almost all quite well with experimental observations. Here, another explanation will be presented which also leads to excellent agreement with the experimentally found onset and which may have some merits. It is based on the " $\omega_e \tau_e$ -dependency" of the electron heatflux (see Appendix A.1) and the fact that with increasing $\omega_e \tau_e$ an overheating of the discharge channel may occur. Such a process which consequently would lead to an unstable "run away heating" could be avoided if the channel assumes a somewhat curved e. g. a helical configuration thereby leading to an increased convection cooling effect [magnetic pumping effect [38]]. In that case increased heating inside the channel would be balanced by an increased loss mechanism.

In the following calculation the condition at which such an overheating occurs will be determined and analyzed.

In order to calculate the maximum value of the product of ω_e , the electron cyclotron frequency times the average collision time ($\tau_e \simeq \frac{1}{\nu_e}$) in the constrictor of a nozzle type hybrid thruster (see Fig.1.1a), one has to determine at first the condition within the constrictor region where the magnetic field becomes a maximum (see Fig.3.1).

By modelling the rotational symmetric, axial current density distribution within the constrictor through a paraboloid of grade n (see Appendix A.2) one obtains for the azimuthal selfinduced magnetic induction field

$$\begin{aligned} B_\theta = B(r) &= \mu_0 \frac{1}{r} \int_0^r j r dr \\ &= \frac{\mu_0 I}{2\pi r_c} \frac{n+2}{n} \frac{r}{r_c} \left[1 - \frac{2}{n+2} \left(\frac{r}{r_c} \right)^n \right] \end{aligned} \quad (3.1)$$

The radial dependent, absolute value of the electron cyclotron frequency follows therefore (see also Appendix A.2) by

$$\omega_e = \left| -\frac{eB(r)}{m_e} \right| = \frac{e}{m_e} B(r) \quad (3.2)$$

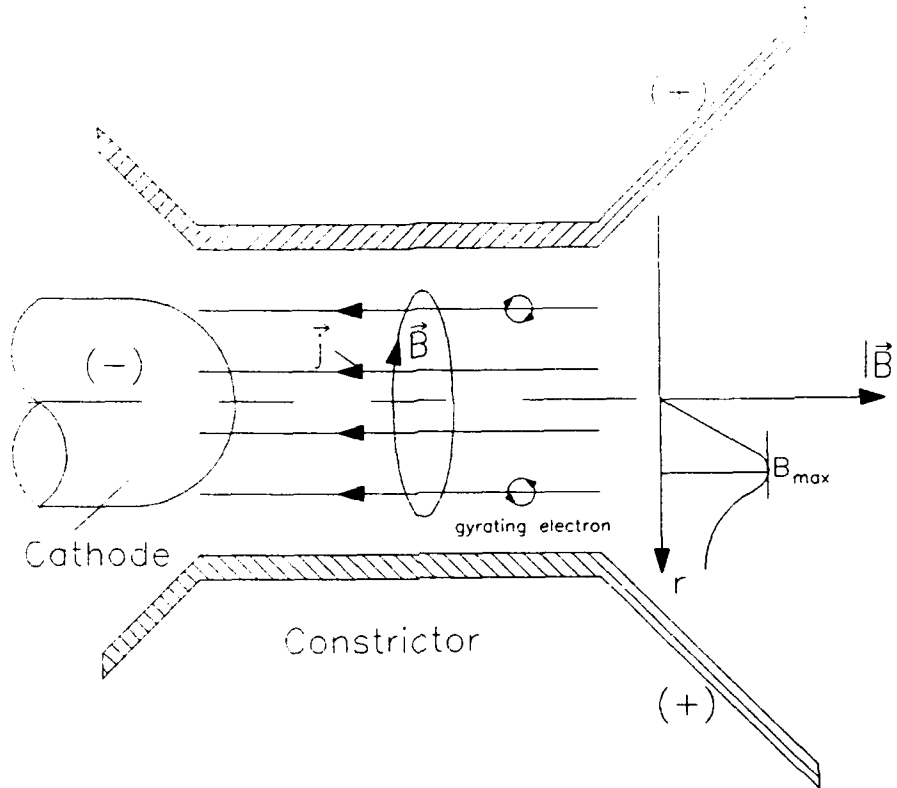


Figure 3.1: Illustration of the Self Magnetic Field within a Plasma Thruster

And the maximum value of B_θ and ω_e follows now by the requirement

$$\frac{\partial}{\partial r} B_\theta(r) = \frac{\partial}{\partial r} \omega_e(r) = 0 \quad (3.3)$$

at

$$\frac{r}{r_0} = \left(\frac{1}{2} \cdot \frac{n+2}{n+1} \right)^{\frac{1}{n}} \quad (3.4)$$

Hence one obtains the optimal gyration frequency by

$$\omega_e = \frac{e}{m_e} \frac{\mu_0}{2\pi} \frac{I}{r_c} \left(\frac{1}{2} \right)^{\frac{1}{n}} \left(\frac{n+2}{n+1} \right)^{\frac{n+1}{n}} \equiv \frac{e}{m_e} \frac{\mu_0}{2\pi} \frac{I}{r_c} J_3 \quad (3.5)$$

where J_3 is a function of the exponent n of the current density paraboloid which varies between about 1.1 and 1.0 if n changes from 1.5 to 100.

Now the electron collision time τ_e or the reciprocal value of the collision frequency ν_e^{-1} follows according to Appendix A.1 by

$$\begin{aligned} \tau_e = \frac{1}{\nu_e} &= \frac{1}{\sum_{\nu \neq e} n_\nu \frac{8}{3} \sqrt{\frac{\pi}{2}} Q_{ee} \frac{\sqrt{m_\nu k T_\nu}}{m_e + m_\nu}} \\ &= \frac{3}{4} \sqrt{\frac{\pi}{2}} \frac{1}{n_e Q_{ee} \sqrt{\frac{k T_e}{m_e}} \left[1 + 2 \sum_{\nu \neq e} \frac{n_\nu Q_{e\nu}}{n_e Q_{ee}} \sqrt{\frac{m_e k T_\nu}{m_\nu k T_e}} \right]} \end{aligned} \quad (3.6)$$

Since Q_{ee} can be expressed by the Grosdover crosssection [see Appendix A.2, eq. A.59 with $z_\nu = |z_n e| = 1$] and since the sum with the terms proportional to $\sqrt{\frac{m_e T_e}{m_\nu T_\nu}}$ are negligible with respect to one, the collision term, τ_e , for the electrons reduces to

$$\tau_e = \frac{1}{\nu_e} = \frac{24\sqrt{2}\pi^{\frac{3}{2}}}{\ln \left\{ 1 + 144\pi^2 \frac{e^3 k^3 T_e^3}{n_e e^4} \right\}} \frac{e_0^2 \sqrt{m_e}}{n_e e^4} (kT_e)^{\frac{3}{2}} \quad (3.7)$$

By means of the definition of the degree of ionization

$$\alpha = \frac{n_e}{\sum_{\nu \neq e} n_\nu} = \frac{\sum_{\nu \neq e} Z_\nu n_\nu}{\sum_{\nu \neq e} n_\nu} \quad (3.8)$$

and the following relations

$$p = \sum_{\nu \neq e} n_\nu kT + n_e kT_e \quad (3.9)$$

One obtains with $T_e = T_\nu \equiv T$ (constrictor condition)

$$n_e = \frac{\alpha}{1 + \alpha} \frac{p}{kT_e} \quad (3.10)$$

and can replace n_e in the formula for τ_e by p , T_e and α .

The dimensionless product $\omega_e \tau_e$ which is of interest here follows now from eq. 3.5, 3.7 and 3.10 by

$$\begin{aligned} \omega_e \tau_e &= \frac{12\sqrt{2}\pi J_3}{\ln \left\{ 1 + 72\pi^2 \frac{e^3 k^3 T_e^3}{n_e e^4} \right\}} \frac{\mu_0 e_0^2}{e^3 \sqrt{m_e}} \frac{(kT_e)^{\frac{3}{2}}}{n_e} \frac{I}{r_c} \\ &= \frac{3\sqrt{2}\pi J_3}{\ln \left\{ 5.7 \cdot 10^{-3} T_e \left(\frac{1+\alpha}{p\alpha} \right)^{\frac{1}{2}} \right\}} \frac{\mu_0 e_0^2}{e^3 \sqrt{m_e}} \frac{1+\alpha}{\alpha} \frac{(kT_e)^{\frac{3}{2}}}{p} \frac{I}{r_c} \\ &= \frac{1.337 \cdot 10^{-13} J_3}{\ln \left\{ 5.7 \cdot 10^{-3} T_e \left(\frac{1+\alpha}{p\alpha} \right)^{\frac{1}{2}} \right\}} \frac{1+\alpha}{\alpha} \frac{(T_e)^{\frac{3}{2}}}{p} \frac{I}{r_c} \end{aligned} \quad (3.11)$$

were the electron temperature T_e must be given in [K], the pressure, p in [Pa] and the quotient arc current, I , divided by arc radius r_c in $\left[\frac{A}{m} \right]$. The degree of ionisation, α is herein a funktion of T_e and p . The electron temperature T_e within eq. 3.11 follows now by that at the channel radius given by eq. 3.4. The temperature profile is now according to Appendix A.2

$$T_e(r) = \hat{T}_e \left\{ 1 - \frac{n+2}{n(n+4)} \left(\frac{r}{r_c} \right)^2 \frac{1 - \frac{4}{(n+2)^2} \left(\frac{r}{r_c} \right)^n - \xi(r)}{1 - \frac{(n+2)^2}{n(n+4)} \xi(r)} \right\}^{\frac{1}{2}} \quad (3.12)$$

where n is the exponent of the current density paraboloid and $\xi(r) \simeq \xi(r) = \xi$ is a dimensionless factor which accounts for radiation losses and which can be considered small compared to one.

$n =$	1.5	2	3	4	10	100
$\xi = 0$	0.701	0.680	0.646	0.619	0.522	0.292
0.05	0.696	0.676	0.643	0.617	0.521	0.292
0.1	0.690	0.671	0.640	0.614	0.520	0.291
0.2	0.673	0.659	0.632	0.608	0.517	0.291
0.4	0.588	0.607	0.602	0.587	0.510	0.291

Table 3.1: J_2 according to eq.(3.12) and (3.13)

Hence one obtains for the electron temperature, T_e in eq. 3.10

$$T_e = J_2(n, \xi) \hat{T}_e \quad (3.13)$$

where \hat{T}_e is the maximum centerline temperature and where the factor J_2 follows by

$$J_2 = \left\{ 1 - \frac{(n+2)^2}{n(n+4)} \left(\frac{1}{2n+1} \right)^{\frac{2}{n}} \cdot \frac{1 - \frac{2}{(n+1)(n+2)} - \xi}{1 - \frac{(n+2)^2}{n(n+4)} \xi} \right\}^{\frac{1}{2}} \quad (3.14)$$

and is tabulated in table 3.1 for n between 1.5 and 100 and ξ between 0 and 0.4.

according to Appendix A.2 [eq. A.47], one can write the maximum electron temperature, \hat{T}_e in the form

$$\hat{T}_e = 1.51 \cdot 10^2 \gamma J_0 \left(\frac{I}{r_c} \right)^{\frac{2}{3}} \quad (3.15)$$

where $\gamma \cdot J_0$ the product of two faktors which varries slowly with \hat{T}_e or with $\left(\frac{I}{r_c} \right)$, p , n and ξ , depending on the type of propellant (see Appendix A.2 for hydrogen and argon). The faktor J_0 is dimensionless and depends only on n and ξ [see table B.1] while the dimensionless γ depends weakly on p and T_e and the type of propellant. Both faktors p and T_e of the order one. In eq. (3.14) \hat{T}_e follows in Kelvin if I and r_c are taken in Ampere and Meter, respectively. If one now replaces T_e in eq. 3.10 according to eq. 3.12 and eq. 3.14 one obtains

$$\omega_e \tau_e = \beta \frac{1}{p} \left(\frac{I}{r_c} \right)^2 \quad (3.16)$$

where

$$\beta = \frac{3.75 \cdot 10^{-8} (J_0 J_2)^{\frac{1}{2}}}{\ln \left\{ 5.7 \cdot 10^{-3} J_2 \hat{T}_e \left(\frac{1+\alpha}{p\alpha} \right)^{\frac{1}{2}} \right\}} \frac{1+\alpha}{\alpha} \gamma^{\frac{1}{2}} \quad \left[\frac{N}{A^2} \right] \quad (3.17)$$

is a coefficient of the order $10^{-8} \left[\frac{N}{A^2} \right]$ which varries slowly with \hat{T}_e or $\frac{I}{r_c}$ and with p , n and ξ depending on the type of propellant. The faktor β is tabulated for hydrogen and argon in table 3.2 and table 3.3, respectively, for different pressure p and maximum temperatures, \hat{T}_e , with $n = 2, 4, 10$ and $\xi \approx 0$.

$\hat{T}_e =$	2	2.5	3	3.5	4	4.5	5	$\cdot 10^4 [K]$
p= n=2	3.37	3.46	3.62	3.74	3.92	4.06	4.19	
10^3 Pa 4	2.44	2.31	2.40	2.51	2.60	2.69	2.77	$\cdot 10^{-8} \left[\frac{N}{A^2} \right]$
10	2.54	1.41	1.40	1.45	1.50	1.54	1.59	
2		3.59	3.68	3.82	3.96	4.09	4.21	
10^4 Pa 4		2.50	2.48	2.56	2.56	2.73	2.81	$\cdot 10^{-8} \left[\frac{N}{A^2} \right]$
10		1.96	1.51	1.50	1.54	1.58	1.62	
2		4.33	3.96	4.01	4.11	4.23	4.34	
10^5 Pa 4		3.53	3.78	2.72	2.77	2.84	2.91	$\cdot 10^{-8} \left[\frac{N}{A^2} \right]$
10		4.14	2.11	1.72	1.66	1.68	1.71	
n=2			5.17	4.62	4.55	4.59	4.66	
10^6 Pa 4			4.21	3.36	3.16	3.14	3.17	$\cdot 10^{-8} \left[\frac{N}{A^2} \right]$
10			4.51	2.71	2.15	1.98	1.94	

Table 3.2: β for Hydrogen

$\hat{T}_e =$	2	2.5	3	3.5	4	4.5	5	$\cdot 10^4 [K]$
p= n=2	4.45	4.37	4.51	4.57	5.12	5.82	6.58	
10^3 Pa 4	4.04	2.99	3.27	3.23	3.44	3.87	4.37	$\cdot 10^{-8} \left[\frac{N}{A^2} \right]$
10	7.21	2.21	1.99	2.18	2.21	2.28	2.52	
2		4.37	4.44	4.37	4.39	4.74	5.22	
10^4 Pa 4		3.37	3.07	3.19	3.11	3.22	3.49	$\cdot 10^{-8} \left[\frac{N}{A^2} \right]$
10		3.93	2.12	2.00	2.10	2.11	2.12	
2		5.77	4.32	4.18	4.02	3.90	4.01	
10^5 Pa 4		5.63	3.28	2.95	2.92	2.82	2.78	$\cdot 10^{-8} \left[\frac{N}{A^2} \right]$
10		8.92	3.31	2.11	1.89	1.88	1.87	
2			5.47	4.03	3.61	3.35	3.12	
10^6 Pa 4			5.05	3.17	2.63	2.43	2.28	$\cdot 10^{-8} \left[\frac{N}{A^2} \right]$
10			6.18	3.20	2.07	1.67	1.53	

Table 3.3: β for Argon

The degree of ionisation, α in eq 3.17 has been calculated for one two and three times ionized particles under the premise that locally the Saha equilibrium is valid. At lower temperatures and higher pressures, $\alpha = \alpha(T_e, p)$ is fairly small ($\ll 1$) such that β becomes quite large (≥ 8). This range, however, is not of interest here and would result in wrong β - values since under those conditions the second term in the denominator of eq. 3.6 can not be neglected anymore. Since here only the main electrically conducting plasma channel is considered, the space for the β - value in table 3.2 and table 3.3 at lower temperatures and higher pressures are left blank.

One should remark here that eq. 3.10 and eq. 3.11 and therefore eq.3.13 and eq.3.14 has been derived under the premise (see Appendix A.2) that the radial heat conduction of the electrons are still not affected by the $\omega_e \tau_e$ - effects; i.e. one has assumed within the energy equation for the electrons that the heat conduction coefficient is a scalar [see eq A.39] and that the factor $\frac{\sin \omega_e \tau_e}{\omega_e \tau_e}$ with which the heatconduction coefficient, λ_e of the radial flux should be multiplied [see Appendix A.1 eq. A.31] has been tacitly set equal to one. For small $\omega_e \tau_e$ -values this assumption is justified since

$$\frac{\sin \omega_e \tau_e}{\omega_e \tau_e} \approx 1 - \frac{1}{6}(\omega_e \tau_e)^2 + \dots \quad (3.18)$$

Now, for $\omega_e \tau_e \leq 0.25$ the error in the heatconduction coefficient, λ_e amounts to $\leq 1\%$ for $\omega_e \tau_e \leq 0.75$ the error amounts to about 10% and less. As long as $\omega_e \tau_e$ stays well below about 0.75, one therefore may apply eq. 3.15 to determine $\omega_e \tau_e$. On the other hand the $\omega_e \tau_e$ - value calculated according to eq. 3.15 should never exceed a critical value $(\omega_e \tau_e)_{crit} \leq 0.75$ in order to avoid "run away heating" within a discharge channel radius given by eq.3.4. If for instance $\omega_e \tau_e$ would exceed such a critical value, $(\omega_e \tau_e)_{crit}$, the radial heatconductionloss of the electrons would be cut off to a certain extend and the temperature within this core region should increase. According to eq. 3.11 also $\omega_e \tau_e$ should increase further which again leads to an even higher temperature and so on. This run away heating effect presents an instability of the discharge and eventually causes the arc core channel to assume a configuration by which also an increased heatloss is possible. Instead of a straight, rotational symmetric channel configuration, the discharge core region may become bent (e.g. helically shaped) thereby experiencing an increased cooling due to transverse magnetic pumping effects. The overheating in the disturbed core region is therefore balanced by an increased cooling. In reality one observes an onset of voltage fluctuations and an increase in average voltage at a certain critical current which could be explained by such a run away heating effect. The conditions under which onset occurs are now mathematically given by the inequality

$$\omega_e \tau_e = \beta \frac{1}{p} \left(\frac{I}{r_c} \right)^2 < (\omega_e \tau_e)_{crit} \quad (3.19)$$

where the critical value $(\omega_e \tau_e)_{crit}$ should be at least large enough to have an effect on the heatconduction (≥ 0.1) and smaller than 0.75 since only then the equality sign in eq. 3.16 is valid. One therefore may limit $(\omega_e \tau_e)_{crit}$ by about the following range

$$0.1 \leq (\omega_e \tau_e)_{crit} < 0.75 \quad (3.20)$$

Instead of taking the pressure, p , as variable in the stability- or onset criteria [eq. 3.17], one may replace, p , by the mass flow rate \dot{m} of the thruster, provided, that the discharge fills the entire cross section (πr_c^2) of the constrictor. One now obtains for the mass flow rate

$$\dot{m} = 2\pi \int_0^{r_c} \rho v r dr \quad (3.21)$$

where ρ is the local density and given by the relation [see also eq. 3.9 with $T_e = T$]

$$p = \rho(1 + \alpha) \frac{k}{m_0} T \quad (3.22)$$

with m_0 as atomic mass and where the axial velocity, v , can be replaced by the local speed of sound under isothermal conditions [41]; hence it is according to eq.3.20

$$v = \sqrt{\left(\frac{\partial p}{\partial \rho}\right)_{T=\text{const}}} = \sqrt{(1 + \alpha) \frac{k}{m_0} T} \quad (3.23)$$

The axial mass flow rate follows therefore by

$$\begin{aligned} \dot{m} &= 2\pi \int_0^{r_c} \frac{p}{\sqrt{\frac{k}{m_0} T(1 + \alpha)}} r dr \\ &= \pi r_c^2 p \sqrt{\frac{m_0}{k}} \cdot 2 \int_0^1 [T(1 + \alpha)]^{-\frac{1}{2}} \frac{r}{r_c} d\left(\frac{r}{r_c}\right) \\ &= \pi r_c^2 p \sqrt{\frac{m_0}{kT}} \cdot \frac{1}{\sqrt{1 + \alpha}} \end{aligned} \quad (3.24)$$

Herein one neglects the magnetic pinch effect and takes \bar{T} according to Appendix A.2. For $n = 4$ and $\xi \leq 0.2$ one may very well approximate eq 3.24 by

$$\dot{m} = \pi r_c^2 p \sqrt{\frac{m_0}{k\bar{T}}} \cdot \frac{1.15}{\sqrt{1 + \bar{\alpha}}} \quad (3.25)$$

where now $\bar{\alpha}$ is an average degree of ionisation which may be taken as

$$\bar{\alpha} = \alpha(\bar{T}) \quad (3.26)$$

with

$$\bar{T} \approx 0.75\hat{T} \quad (3.27)$$

Within the constrictor the electron- and heavy particle temperature can be considered equal. Hence the pressure p in the stability criteria eq.3.19 can be replaced by

$$\begin{aligned} p &= \frac{\dot{m}}{\pi r_c^2} \sqrt{\frac{k\hat{T}_e}{m_0}} \frac{\sqrt{1 + \bar{\alpha}}}{1.15} \\ &= 25.24 \frac{\dot{m}}{r_c^2} \sqrt{\frac{\hat{T}_e(1 + \bar{\alpha})}{M_c}} \quad [Pa] \\ &= 310 \sqrt{\frac{1 + \bar{\alpha}}{M_c}} \frac{\dot{m}}{r_c^2} \gamma J_0 \frac{1}{I^{\frac{1}{2}}} \quad [Pa] \end{aligned} \quad (3.28)$$

where the last expression follows according to eq 3.14; M_c is the atomic weight. The stability criteria can now be written in the form

$$\omega_e \tau_e = \beta^* r^{\frac{1}{2}} \frac{I^{\frac{1}{2}}}{m} < (\omega_e \tau_e)_{crit} \quad (3.29)$$

with

$$\beta^* = 3.22 \cdot 10^{-3} \frac{\beta \sqrt{M_0}}{\sqrt{\gamma J_0 (1 + \bar{\alpha})}} \left[\frac{kg}{sm^{\frac{1}{2}} A^{\frac{1}{2}}} \right] \quad (3.30)$$

a slowly varying factor in \hat{T} or $\frac{I}{r_c}$ and in p, n and ξ and which depends on the type of plasma. β^* is tabulated for hydrogen and argon in table 3.4 and table 3.5, respectively, for different temperatures \hat{T}_e and pressures p with $n = 2, 4, 10$ and $\xi \leq 0.2$.

$\hat{T}_e =$		2	2.5	3	3.5	4	4.5	5	$\cdot 10^4 [K]$
$p =$	$n = 2$	6.29	6.03	5.46	5.27	5.36	5.47	5.57	$\cdot 10^{-11} \left[\frac{kg}{sm^{\frac{1}{2}} A^{\frac{1}{2}}} \right]$
	4	4.70	4.15	3.70	3.64	3.70	3.77	3.84	
	10	5.05	2.61	2.22	2.18	2.21	2.24	2.28	
$10^3 Pa$	2		6.66	6.34	5.79	5.65	5.71	5.79	$\cdot 10^{-11} \left[\frac{kg}{sm^{\frac{1}{2}} A^{\frac{1}{2}}} \right]$
	4		4.82	4.40	4.00	3.80	3.97	4.02	
	10		3.90	2.75	2.41	2.36	2.38	2.40	
$10^4 Pa$	2		9.04	7.47	7.02	6.48	6.35	6.22	$\cdot 10^{-11} \left[\frac{kg}{sm^{\frac{1}{2}} A^{\frac{1}{2}}} \right]$
	4		7.59	5.44	4.91	4.50	4.35	4.34	
	10		9.13	4.26	3.18	2.77	2.66	2.64	
$10^5 Pa$	2			11.1	9.03	8.31	7.72	7.28	$\cdot 10^{-11} \left[\frac{kg}{sm^{\frac{1}{2}} A^{\frac{1}{2}}} \right]$
	4			9.32	6.79	5.96	5.44	5.12	
	10			9.41	4.40	4.16	3.52	3.22	
$10^6 Pa$	2								$\cdot 10^{-11} \left[\frac{kg}{sm^{\frac{1}{2}} A^{\frac{1}{2}}} \right]$
	4								
	10								

Table 3.4: β^* for Hydrogen

$\hat{T}_e =$		2	2.5	3	3.5	4	4.5	5	$\cdot 10^4 [K]$
p=	n=2	5.07	4.56	3.98	3.69	3.96	4.36	4.77	$\cdot 10^{-10} \left[\frac{kg}{sm^3 A^3} \right]$
$10^3 Pa$	4	4.76	3.23	2.97	2.71	2.71	2.77	3.30	
	10	8.77	2.45	1.86	1.89	1.85	1.84	1.97	
	2		4.97	4.63	3.96	3.69	3.84	4.11	$\cdot 10^{-10} \left[\frac{kg}{sm^3 A^3} \right]$
$10^4 Pa$	4		3.97	3.30	2.98	2.72	2.72	2.86	
	10		4.79	2.33	1.92	1.90	1.84	1.80	
p=	n=2		7.55	5.10	4.56	3.92	3.54	3.50	$\cdot 10^{-10} \left[\frac{kg}{sm^3 A^3} \right]$
$10^5 Pa$	4		7.57	4.01	3.31	2.94	2.65	2.53	
	10		5.00	4.18	2.43	1.95	1.83	1.76	
	2			7.64	5.17	4.35	3.73	3.23	$\cdot 10^{-10} \left[\frac{kg}{sm^3 A^3} \right]$
$10^6 Pa$	4			7.29	4.21	3.27	2.79	2.44	
	10			10.0	4.38	2.64	1.96	1.69	

Table 3.5: β^* for Argon

Constrictor diameter	Measurement			$\omega_e \tau_e$ calculated		
	\dot{m}	I_{crit}	$\left(r_c \frac{1}{2} \frac{I^{9/5}}{\dot{m}}\right)_{crit}$	n=10	n=4	n=2
0.024	0.3	2700	2.07	0.38	0.57	0.78
	0.6	3800	1.91	0.35	0.55	0.80
	0.8	4500	1.94	0.37	0.56	0.77
	1.0	4800 ₊	1.75	0.31	0.50	0.70
	1.5	6000 ₊	1.74	0.35	0.49	0.71
0.030	0.8	4300	1.87	0.34	0.56	0.75
	1.6	6400	1.92	0.34	0.54	0.78
[m]	$\cdot 10^{-3} [kg/s]$	[A]	$\cdot 10^9 [m^{1/5} s A^{9/5} / kg]$	0.35	0.54	0.76

Table 3.6: $\omega_e \tau_e$ -Values calculated for different Onset conditions at n=2, 4, 10 for Argon

Constrictor diameter	\dot{m}	I_{crit}	$\left(r_c \frac{1}{2} \frac{I^{9/5}}{\dot{m}}\right)_{crit}$	n=10	n=4	n=2
0.024	0.15	1400	3.07	0.1	0.15	0.17
[m]	$\cdot 10^{-3} [kg/s]$	[A]	$\cdot 10^9 [m^{1/5} s A^{9/5} / kg]$			

Table 3.7: $\omega_e \tau_e$ -values calculated for different Onset conditions at n=2, 4, 10 for Hydrogen

In table 3.6 and 3.7 the $\omega_e \tau_e$ - values for two MPD-thrusters with different constrictor sizes and propellants are calculated for the given onset conditions. In the case for Argon these values lie between about 0,35 and 0,76 depending on the exponent n for the current density paraboloid. Hence it is shown that the observed onset occurs at $\omega_e \tau_e$ - values which cannot be neglectable besides one and that the critical value, $(\omega_e \tau_e)_{crit}$ at which onset occurs is almost proportional to $\frac{I^{1/5}}{\dot{m}}$ what again, agrees very well with the experimental results. The one hydrogen measurements available with the 24 mm constrictor results in a somewhat smaller critical value $(\omega_e \tau_e)_{crit}$ than that calculated for Argon. This discrepancy, however, could be explained by the fact that the discharge channel does not fill the constrictor cross section. This is the more likely since the volume gas flow for hydrogen is much higher than that for argon in a similar current range and therefore confirms the current carrying cross section for hydrogen within a smaller area than that for argon. The consequence of this effect means that the taken mass flow rate for hydrogen is too high. Nevertheless this calculation shows that the $\omega_e \tau_e$ -values in a discharge column becomes large enough to explain the onset phenomenon by "run away Joule heating" .

4. Electrode Effects

4.1 Cathode Experiments

The scheme and test assembly of the cathode erosion experiment are shown in Fig. 4.1 and 4.2, respectively. The cathode consists of a thoriated (2% thorium oxide) tungsten rod of 3 mm diameter. The anode, a metal button of the same material, is mounted transversely to the cathode rod in a distance of 1 mm from the cathode surface. The electrode system and the ignitor are located in the middle of a stainless steel tank with a diameter of 1 m and a length of 2 m.

By means of a PFN (pulse forming network) - battery and an ignitor the cathode is charged by a fairly rectangular current pulse of about 1400 A for ≈ 2 ms. A typical current time pulse is plotted in Fig. 4.3. One pulse transfers an electric charge of about 2,6 As (1 As = 1 Ampere second = 1 Coul). Small variations in the pulse profile were averaged over 50 shots per measuring point and the small variation in the electrical charge per pulse have been accounted for.

The repetition rate of the fully automatically working test facility can be varied between several seconds and several minutes. In the cold cathode experiment the repetition rate is taken between 1 and 2 minutes in order to allow the cathode to cool down between the shots.

4.2 Measurements

The weight loss of the cathode sample has been measured after 50 shots by means of a very accurate scale and the erosion rate given by the weight loss per transferred electric charge is plotted in Fig. 4.4 a, b, c, d, e and f for ambient pressures of 10, 100, 1000, 10000 and 100 000 Pa, respectively. These measurements indicate a strong increase of the erosion rate with an increasing number of shots or with an increasing accumulated electric charge in the beginning and after about 500 shots (each measuring point represents ≈ 50 shots) which corresponds to about 1300 As the erosion rate levels off and reaches a constant value. This fact may be caused by roughening of the original, polished surface due to spot and crater formation and/or due to depletion of the thorium oxide at the main impact area which directly faces the anode. The measurements at 1 bar (Fig.

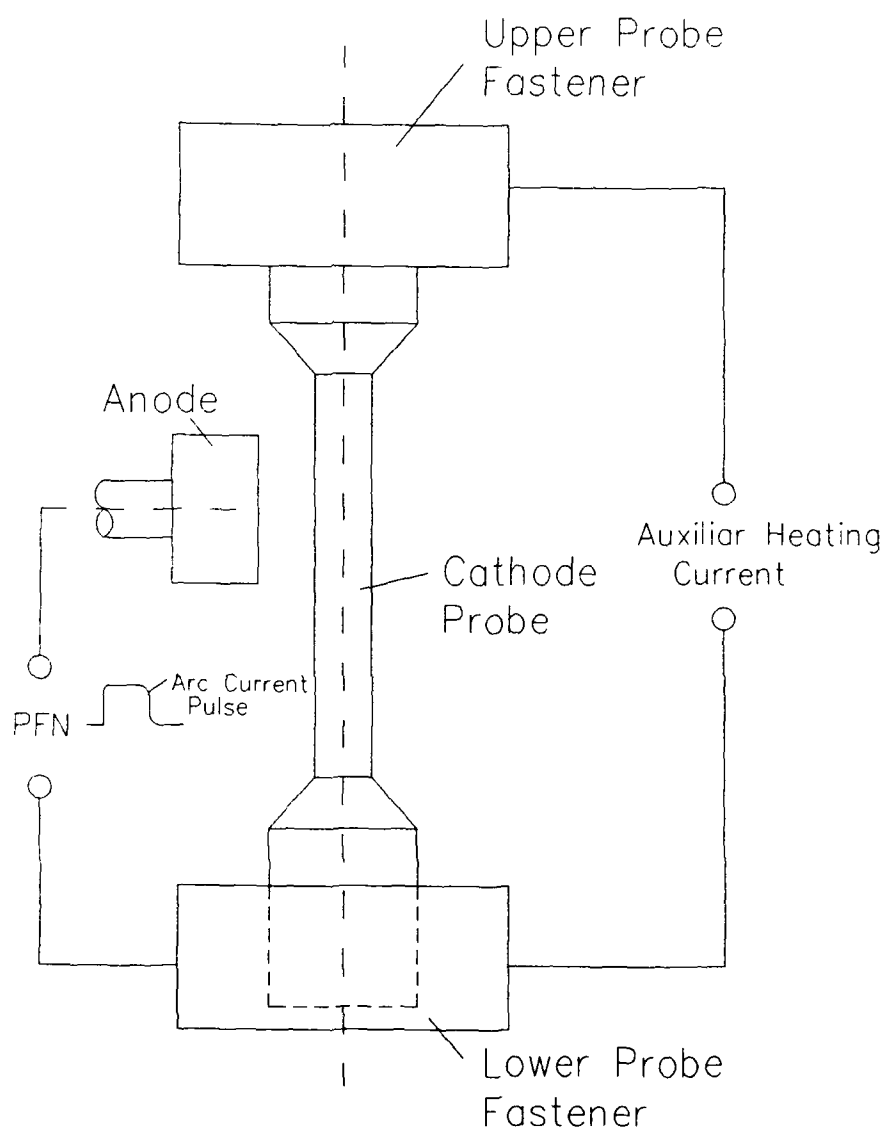


Figure 4.1: Scheme of Cathode Testrig

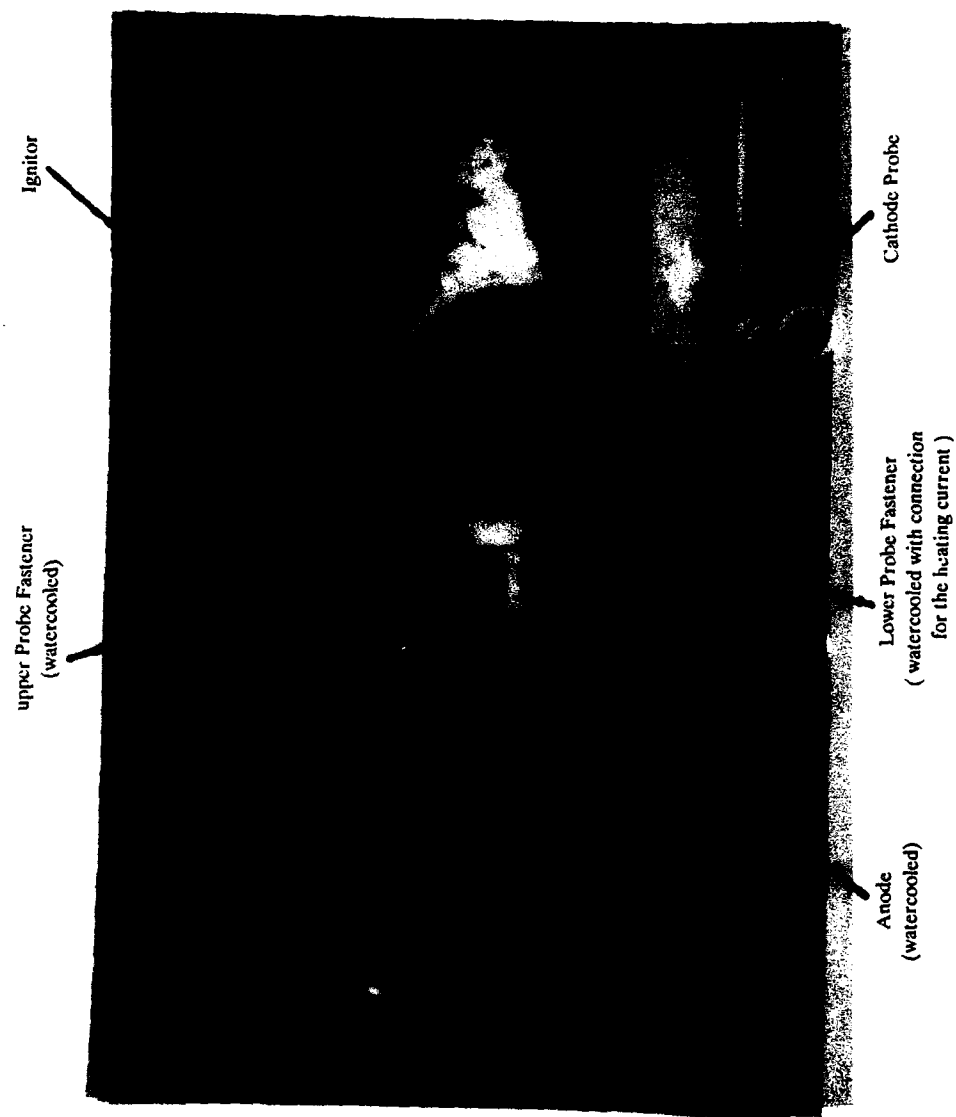


Figure 4.2: Testrig for Cathode Experiment

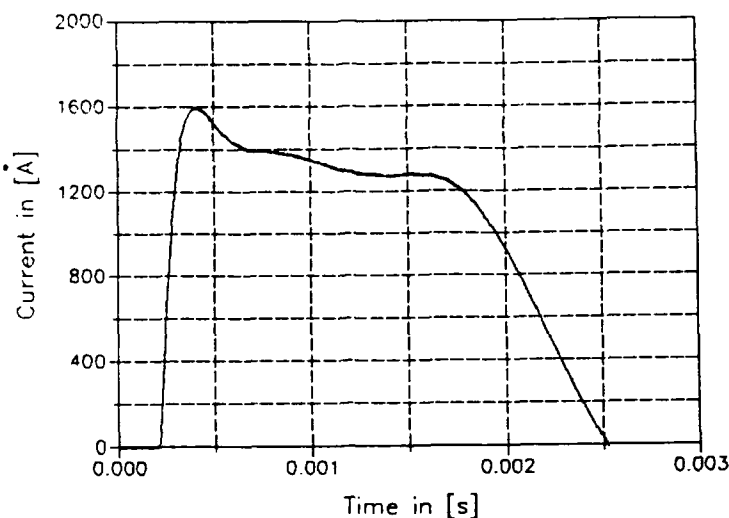


Figure 4.3: Typical Current vers. Time Curve

4.4f) scatter somewhat since the weight loss in that case is fairly small (≈ 0.05 mg) and therefore difficult to measure correctly. In Fig. 4.5 these results are again summarized in one plot in order to show the influence of the pressure on the erosion rate.

If one plots the asymptotic value of erosion rate as function of pressure as shown in Fig. 4.6, there is a distinct threshold between an ambient nitrogen- pressure of 100 and 1000 Pa. Below about 100 Pa the erosion rate seems to stay fairly constant at $27 \mu\text{g/Coul}$, above 100 Pa the erosion rate drops threshold like with increasing pressure to, about $9 \mu\text{g/Coul}$ at 1000 Pa and about $4 \mu\text{g/Coul}$ at 10 000 Pa (≈ 0.1 bar).

Erosion experiments with heated cathode samples showed only limited results. The mass loss (outgasing and evaporation) due to auxiliary heating alone are already fairly high and the specific loss amounts to about $0.1 \mu\text{g/Ws}$ as shown in Fig. 4.7. Interesting to note here is the fact that within a nitrogen atmosphere the mass loss increases rapidly when the heating power exceeds about 450 W what corresponds to a sample surface temperature of about 2000 K. The calibration curve [see Fig. 4.8] between heating power and surface temperature are based on pyrometer measurements taking an emission coefficient for thoriated tungsten of $\epsilon = 0.45$. The strong increase of mass loss due to heating alone in a nitrogen atmosphere above sample temperature of 2000 K indicates that chemical reaction of nitrogen and the thoriated tungsten surface will enhance the mass loss of the sample. These mass loss due to pure heating could not be avoided even after longer heating periods and outgasing. They hampered the proper erosion measurements caused by the arc pulses. Nevertheless, the erosion rates on the cathode samples (thoriated tungsten) due to arcing alone has been determined by measuring the mass losses with and without arc pulses. These cathode losses show that the erosion rates are about one

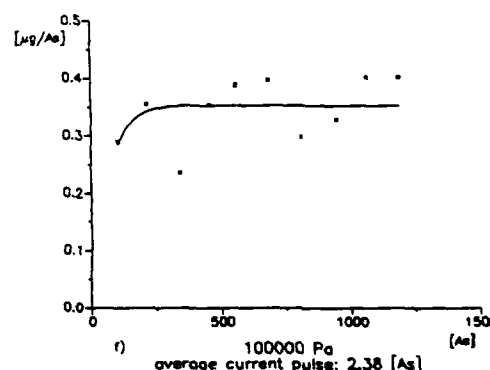
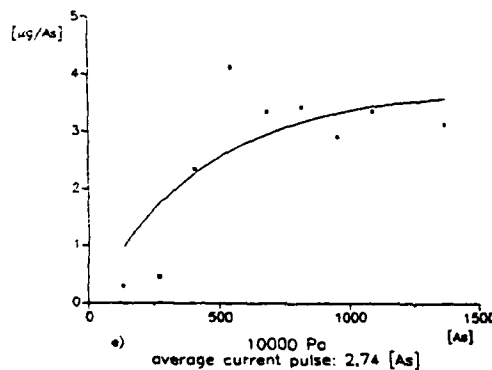
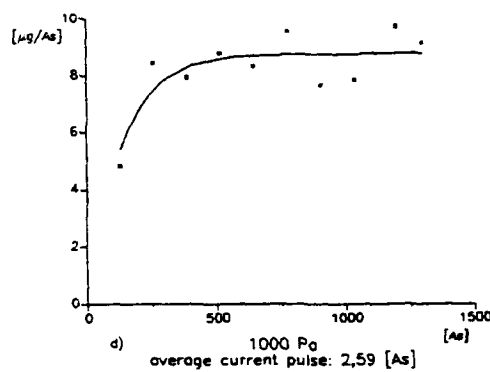
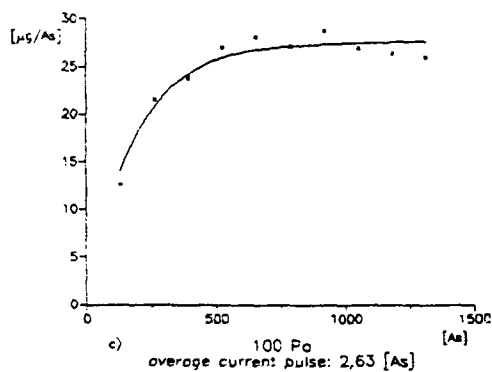
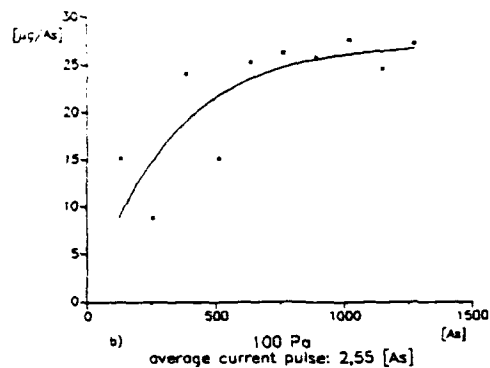
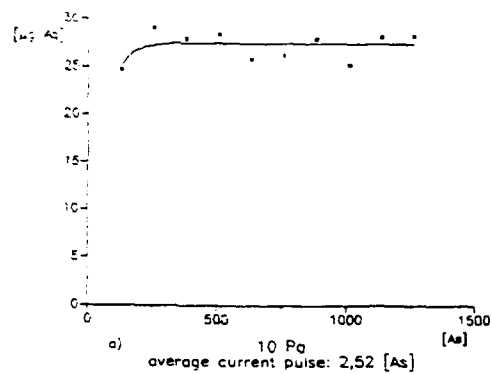


Figure 4.4: Measured Erosionrates in $\left[\frac{\mu g}{As}\right]$ as Funktion of the Accumulated Total Electric Charge in [As] for Different Ambient Pressures. Each Measuring Point is the Result of 50 Current Pulses.(Cathode: Thoriated Tungsten at Room Temperature)

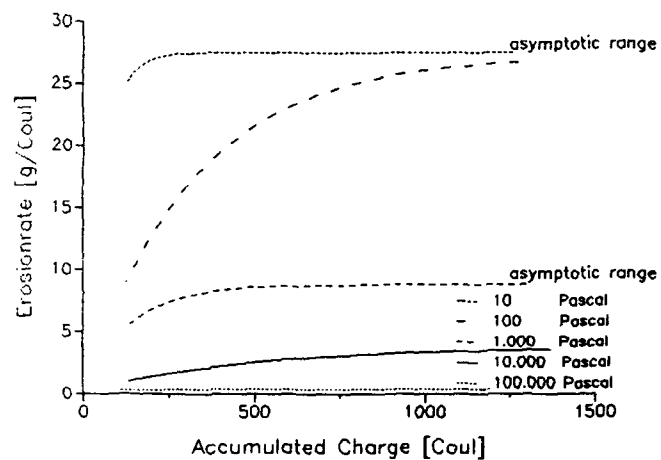


Figure 4.5: Erosion Rate as Funktion of the Accumulated Charge (Number of Current Pulses)

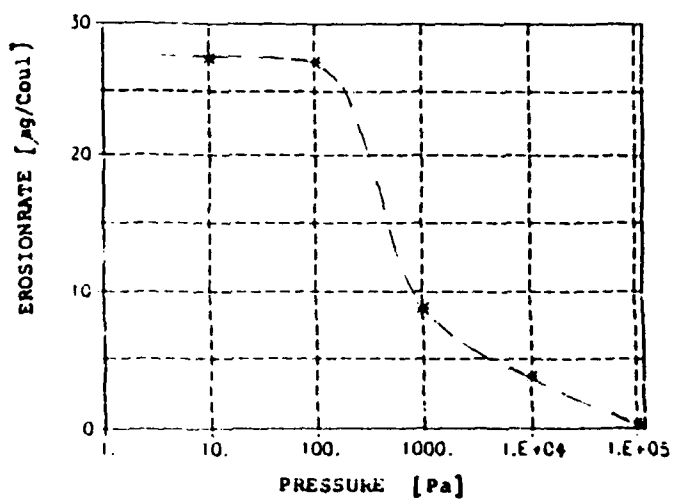


Figure 4.6: Asymptotic Erosion Rate as Funktion of the Ambient Pressure of a Tungsten Cathode in a Nitrogen Atmosphere Charged by a Rectangular Pulses of 1400 A for 2 ms (Pulsfrequency = $1 \cdot 2 \text{ min}^{-1}$)

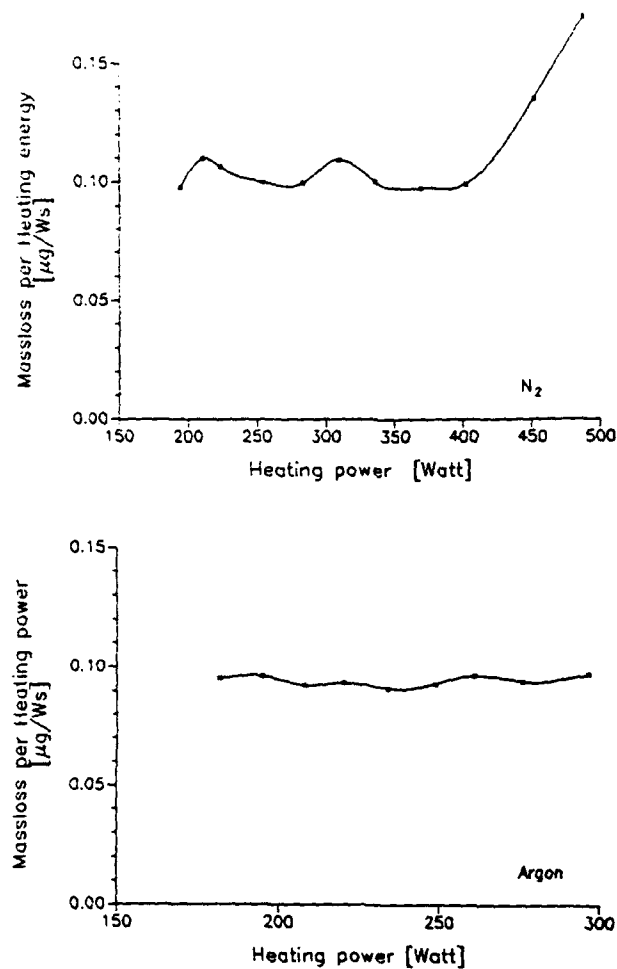


Figure 4.7: Massloss Due to Pure Heating in a Nitrogen and Argon Atmosphere ($p \leq 100\text{Pa}$)

order higher at heated cathodes than at cold ones. In table 4.2 the erosion rates with increasing number of discharges are tabulated.

Reliable measurements beyond about 2000 K at the cathode sample could not be obtained with the present testrig since fusing between sample and fasteners occurred. At these higher temperatures the pressures were also limited to about 100 Pa and less since convection cooling became too strong and also did not allow to achieve higher temperatures than about 2000 K.

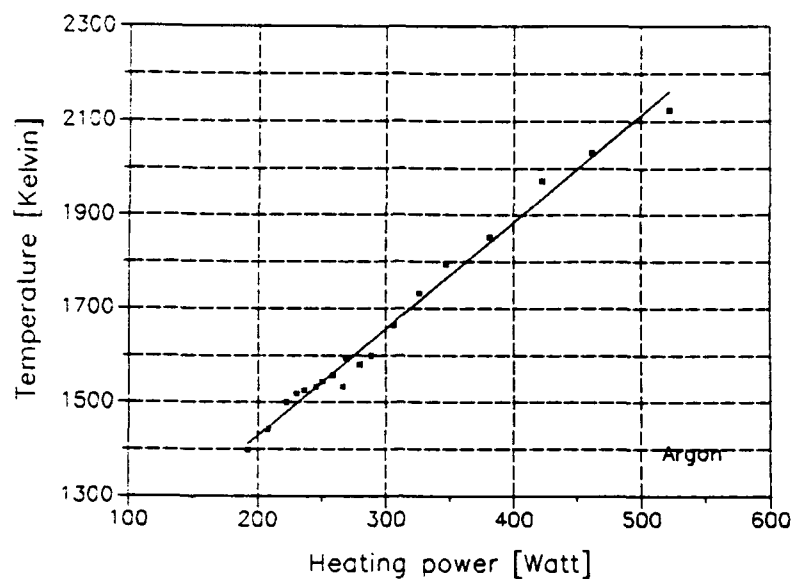


Figure 4.8: Temperature of the heated probe ($\epsilon = 0.45$) as Funktion of the Heating Power

Number of Discharges	Accumulated Electric Charge in As	Erosionrate in $\mu\text{g}/\text{As}$
50	135.35	31.4
100	270.06	186.0
150	405.89	292.0
200	541.03	226.0
250	678.83	223.5
300	815.12	231.3
350	949.52	220.9
400	1082.92	243.7
450	1219.24	250.5
500	1354.68	229.8
average	2.71	
scattering	2.14 %	
	Average Asymptotic Erosionrate	245.2

Table 4.1: Erosionrate caused by arcing only at the surface of a heated tungsten (2% thoriated) cathode in a N_2 -atmosphere ($\leq 100\text{Pa}$) surface temperature: $\approx 1500\text{K}$

4.3 Conclusion and Explanation (qualitative)

The falling characteristic of the erosion rate with increasing pressure (see Fig. 4.6) has been observed before [40, 41, 42, 43] and reported on . Here a qualitative explanation based on the previously developed spot or micro jet theory [18, 38, 44, 46, 47, 48, 49] is presented. Based on that theory the main electron emitting cathode area consists of one or more hot spots of high current-density ($\hat{j} \approx 10^{11} \text{ A/m}^2$ and higher) which cause locally an extremely high heat load on the cathode surface leading to strong local evaporation and micro craters from which electrically conducting plasmajets propagate. Within the spotcraters the vapor plasma pressure, p_s , is quite high and can reach several tens to even 100 bar which depends on the electrode material while the ambient pressure, p_∞ , is usually much smaller. Now, the spot theory tells us that a spot- discharge remains stable i.e. sticks to the same crater like emission site as long as the requirement

$$p_s - p_0 \geq 3.3 \frac{\mu_0}{8\pi} I_s \hat{j}_s \quad (4.1)$$

is fulfilled i.e. the pressure at the inner crater surface p_s , minus the pressure at the outer edge of the current carrying plasmajet, p_0 , (see Fig. 4.9) is larger than about 3.3-times the average pinchpressure of the electrically conducting channel of the plasmajet. If the requirement (4.1) does not hold anymore the main current carrying channel of the plasmajet will bend and attaches the cathode surface somewhere in the neighborhood of the original spot thereby creating a new spot site. Therefore the spot current, I_s , cannot

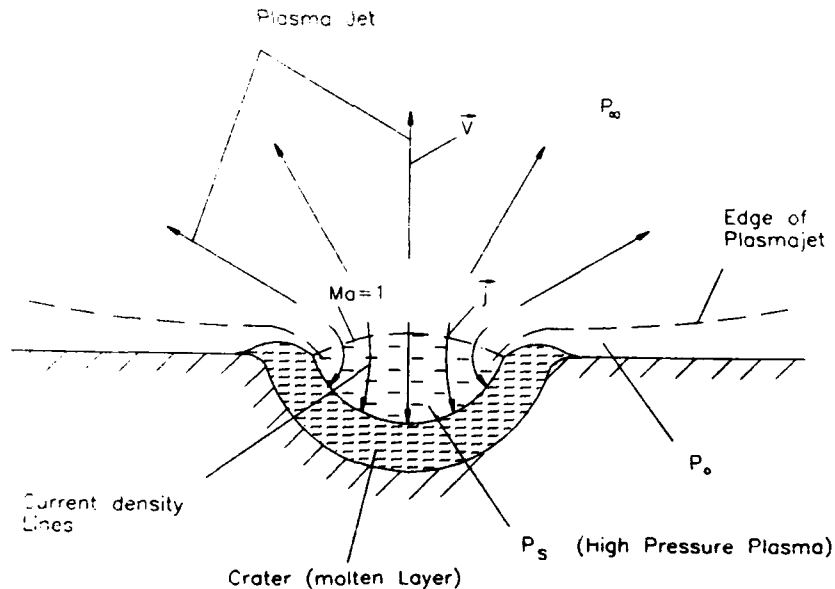


Figure 4.9: Scheme of a Spot Discharge

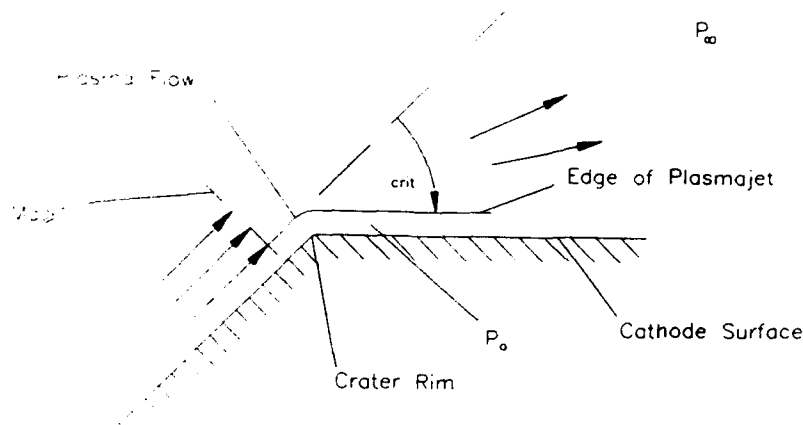


Figure 4.10: Illustration of the Plasmaflow around the Crater Rim with Prandtl-Meyer Deflection Angle, δ

exceed a value as given by eq. (4.1).

In addition the spot theory shows that the minimum erosion rate, ϵ_{Min} in $[\frac{kg}{A \cdot s}]$, due to evaporation is independent of the total current, $I (= \sum I_s)$, or the number of spots, but depends on the (average) spot current I_s , the molecular or atomic weight, M of the evaporated cathode material and the surface temperature within the active crater, T_s . It is

$$\epsilon_{Min} = c \sqrt{\frac{M}{T_s}} I_s \leq \epsilon \quad (4.2)$$

where ϵ is the real erosion rate and $[c \approx 10^{-9} [\frac{kg K^{\frac{1}{2}}}{A \cdot s}]]$ is a factor which depends in a minor way on the geometry of the crater and to some extent on an applied magnetic field. Here in our consideration in which the directional motion is omitted, one may take c as a constant. Based on the relations (4.1) and (4.2) one can now explain the threshold like falling characteristic of the erosion versus pressure curve by means of the Prandtl-Meyer deflection [50] as shown in Fig.4.9 and 4.10.

According to eq. (4.2) the minimum erosion rate and consequently the real erosion rate decreases the smaller the average spot current, I_s , at which the spot discharge becomes unstable.

Now, in order to achieve such an unstable condition (see eq.(4.1)) one has to make at a given spot current density, \hat{j} , the pressure difference ($p_s - p_0$) smaller, or at a given pressure difference the current density larger. The average current density, \hat{j} , however, is strongly coupled to the spot pressure, p_s , and both are constant or simultaneously either

increase or decrease. Both quantities \dot{j} and p_s cannot be changed directly. Therefore, in order to lower the spot current and the erosionrate one has to increase p_0 or better increase the ambient pressure, p_∞ . This fact agrees qualitatively with the experimental finding.

The threshold like increase of the erosionrate by lowering the pressure from about 100 Pa to 1000 Pa (see Fig. 4.6) needs, however, a more detailed discussion of the shape of the plasmajet.

As long as the Prandtl-Meyer deflection δ is smaller than a critical angle, δ_{crit} (see Fig. 4.10, where δ_{crit} spans between the slope of the inner crater surface and the proper cathode surface) the edge of the plasmajet does not touch the cathode surface outside the crater and the pressure, p_0 can be considered equal to the ambient pressure, p_∞ . If, however, the Prandtl-Meyer deflection exceeds δ_{crit} , the plasmajet will hit the cathode surface and thereby evaporate cathode material, ($p_0 \geq p_\infty$) and eventually increase the crater size.

The Prandtl-Meyer deflection angle, δ increases now with decreasing pressure ratio, $\frac{p_0}{p_s}$, according to the following relations [50]

$$\delta = \varphi - \psi \quad (4.3)$$

where φ and ψ follows from

$$\tan(\varphi \sqrt{\frac{\kappa-1}{\kappa+1}}) = \sqrt{\frac{2}{\kappa+1} \left(\frac{p_s}{p_0}\right)^{\frac{\kappa-1}{\kappa}} - 1} \quad (4.4)$$

$$\tan \psi = \sqrt{\frac{\kappa+1}{\kappa-1}} \sqrt{\frac{2}{\kappa+1} \left(\frac{p_s}{p_0}\right)^{\frac{\kappa-1}{\kappa}} - 1} \quad (4.5)$$

$\kappa = \frac{c_p}{c_v}$ is the ratio of the specific heats, with the range of the pressure ratio: $\left[0 \leq \frac{p_0}{p_s} \leq \left\{\frac{2}{\kappa+1}\right\}^{\frac{\kappa}{\kappa-1}}\right]$

For $\frac{p_0}{p_s} = \frac{2}{\kappa+1}^{\frac{\kappa}{\kappa-1}}$ ($=0.56$ for $\kappa=1.2$ and 0.49 for $\kappa = 1.66$) the expansionflow reaches $M_a = 1$; for $\frac{p_0}{p_s} \leq \left(\frac{2}{\kappa+1}\right)^{\frac{\kappa}{\kappa-1}}$ the expansionflow is supersonic. The deflectionangle δ is tabulated for various values $\frac{p_0}{p_s}$ and κ in Table 4.2.

For an ambient pressure p_∞ of about $1 \text{ bar} (= 10^5 \text{ Pa})$ one can expect the pressure ratio $\frac{p_0}{p_s}$ in the range: $\frac{p_0}{p_s} = \frac{p_\infty}{p_s} = 10^{-1} - 10^{-2}$; i.e. the Prandtl-Meyer deflection can still be considered small such that the plasmajet does not hit the cathode surface outside the crater rim. If, however, $\frac{p_0}{p_s}$ reaches values of about $10^{-3} - 10^{-4}$, there is a great possibility (even for $\kappa = 1.66$) that the plasma comes close to or even hits the cathode surface and therefore evaporates additional cathode material ($p_0 \geq p_\infty$). By further lowering of the ambient pressure, p_∞ , this limited area will also emit electrons and must be counted to the spot crater. Hence the spot size of the electrically active crater increases if one lowers the ambient pressure. This fact has been indeed observed before [51]. By means of the well known phenomenon of the Prandtl-Meyer expansionflow applied to the flow of cathode spot, one therefore can explain the almost thresholdlike increase of the erosionrate by lowering the ambient pressure below $\sim 1000 \text{ Pa}$. The observed erosionrate versus pressure curve as shown in Fig.4.6, however, is specific for the given experiment and cannot be generalized. At more powerfull current pulses and/or longer lasting pulses than in the experiment presented here and especially on ductile cathode materials

$\frac{p_0}{p_a}$ ~ 0	$\kappa = 1.2$ ~ 207	$\kappa = 1.4$ 129	$\kappa = 1.66$ ~ 90
10^{-7}	160,7	116,8	86,0
10^{-6}	150,3	111,9	83,7
10^{-5}	137,5	105,0	80,0
10^{-4}	121,4	95,2	74,2
10^{-3}	101,0	81,4	64,9
10^{-2}	74,4	61,2	49,8
10^{-1}	37,2	30,5	24,5
0.2	22,6	18,0	13,8
0.4	6,44	4,10	2,16

Table 4.2: Prandel- Mayer Deflection δ for various pressure ratios $\frac{p_0}{p_a}$ and κ - values

like copper and aluminium etc., the transition from higher erosionrates at low ambient pressures ($\leq 10\text{Pa}$) to lower erosion rates at higher ambient pressures ($\geq 10^3\text{ Pa}$) is less steep and moreover the erosionrate can increase dramatically at higherpressures too. This latter behavior stems from the fact that at higher pressures ($\geq 10^4\text{ Pa}$) the spot activity is located in a smaller area of the cathode surface and that not only the active spot but the entire area becomes molten and erodes very heavily by droplet jecton and/or splashing [45].

5. List of Reports and Publications

During the period of the research grant the following reports, and student thesis have been accomplished. Either the entire publications or part of them are supported by this grant.

Papers

- Schrade H.O., Auweter-Kurtz M., Kurtz H.L., Merke, Sleziona P.C., "Plasma Thruster Development", AFOSR-84-0394, September 1986.
- Auweter-Kurtz M., Kurtz H.L., Schrade H.O., Sleziona P.C., "Numerical Modeling of the Flow Discharge in MPD-Thrusters", AIAA-87-1091, 19th International Electric Propulsion Conference, Colorado Springs, CO, 1987.
- Schrade H.O., Auweter-Kurtz M. and Kurtz H.L., "Cathode Erosions Studies on MPD-Thrusters", AIAA Journal Vol. 25 p 1105 1987
- Sleziona P.C., Auweter-Kurtz M., Schrade H.O., "Numerical Codes for Cylindrical MPD-Thrusters", IEPC 88-043, 20th International Electric Propulsion Conference, Garmisch-Partenkirchen, 1988.
- Auweter-Kurtz M., Glaser S.F., Kurtz H.L., Schrade H.O., Sleziona P.C., "An Improved Code for Nozzle Type Steady State MPD-Thrusters", IEPC 88-043, 20th International Electric Propulsion Conference, Garmisch-Partenkirchen, 1988.
- Schrade H.O., Auweter-Kurtz M., Kurtz H.L., Merke W.D., Sleziona P.C., "Plasma Thruster Development", N 00014-87-G-0119, October 1988.
- Auweter-Kurtz M., Kurtz H.L., Merke W.D., Sleziona P.C., "Numerical Modeling of the Flow Discharge in MPD-Thrusters", Journal of Propulsion and Power, Vol. 5 No. 1, pp. 49-55, 1989.
- Schrade H.O., "Arc Cathode Spots: Their Mechanism and Motion", IEEE Trans. Plasma Science, Vol. 17 p. 635, 1989.
- Auweter-Kurtz M., Kurtz H.L., Merke W.D., Schrade H.O., Sleziona P.C., Wegmann T., "High Power Steady State MPD-Thruster", AFOSR-88-0325, March 1990.

- Sleziona P.C., Auweter-Kurtz M., Schrade H.O., " Numerical Evaluation of MPD-Thrusters ", AIAA 90-2602, 12st Inetrnational Electric Propulsion Conference, Orlando, FL, July 1990.
- Schrade H.O., "Fundamentals of Arc Electrode Interaction Phenomena", Contribution to the Workshop on Electrode Erosion in Electric Space Propulsion Engines, Edited by M.Kristiansen and L.Hatfield Tex Tech Univ. Lubbock Tex, March 1989.
- Sleziona P.C., Auweter-Kurtz M., Schrade H.O., Wegmann T., " Comparison of Numerical and Experimental Investigations of Nozzle Type MPD Accelerators ", AIAA 90-2663, 21st International Electric Propulsion Conference, Orlando, FL, July 1990.
- Sleziona P.C., Auweter-Kurtz M., Schrade H.O., " Computation of MPD Flows and Comparison with Experimental Results ", Second World Congress on Computational Mechanics. Stuttgart, FRG, August 1990.
- Polk J.E., Kelly A.J. and Jahn R.G. (Princeton Univ.), Kurtz H.L., Auweter-Kurtz M. and Schrade H.O. (Univ. Stuttgart), "Mechanisms of Hot Cathode Erosion in Plasma Thrusters", 21st International Electric Propulsion Conference AIAA-90-2673, Orlando FL, July 1990.
- Glocker B., Schrade H.O. and Sleziona P.C., "Numerical Prediction of Arcjet Performance", 21st International Electric Propulsion Conference AIAA-90-2612, Orlando, FL, July 1990.
- Auweter-Kurtz M., Glocker B., Kurtz H.L., Loesener O., Schrade H.O., Tubanos N., Wegmann T. and Willer D. (Univ. Stuttgart) and Polk J.E. (Princeton Univ.), " Cathode Phenomena in Plasma Thrusters", 21st International Electric Propulsion Conference AIAA-90-2662, Orlando, FL, July 1990.

Diplom-and Student-Thesis Work

- Isselhorst A., "Calculation of the Expansionprocess in a Plasma-Thruster Accounting for electromagnetic Compression", IRS No. 87-S5 Diplomthesis 1987.
- Glaser S.F., "Calculation of the Expansionprocess in a Plasma-Thruster by means Of a Two Temperature Model", IRS No.88- S23 Diplomthesis 1988.
- Weber K., "Heat-Transport in Micro-Spots of Arc Cathodes", IRS No. 88 Diplomthesis 1988.
- Mayer W., "Numerical Flow Calculations in Cylindrical MPD- Thrusters by means of a Finite Volume Methode, IRS No.89-S1 Diplomthesis 1989.
- Zube D., "Building and Testing of an Automatically Working Cathode Erosion Experiment", IRS No. 89 S2 Student-Thesis 1989.

- Kempf N., "Heat- and Masstransport Behavior of Micro-spots on Arc Cathodes".
- Fuchs U., "Coupled Flow- and Current Code Calculation of a Cylindrical MPD-Propulsion Device", IRS 89-S22, Diplomthesis 1989.
- Gerhard H-M., "Two Dimensional Flow calculations of a Nozzle Type MPD-Thrusters", IRS 89-S23 Diplomthesis 1989.
- Renner A., "Calculations of Plasma-Thrusters with Different Nozzle Geometries", IRS Nr. 90-S12 Student-Thesis 1990.
- Fasoulas St. , " Microspot Behavior on Arc Cathodes in Various Magnetic Field Configurations " , IRS Nr. 90-S17, July 1990.

Reports

on the theme :

Basic Processes of Plasma Propulsion	Period covered
1. Interim Scientific Report	1.Aug. 1986 - 31 July 1987
2. Interim Scientific Report	1.Aug. 1987 - 31 July 1988
3. Interim Scientific Report	1.Aug. 1988 - 31 July 1989

6. Acknowledgements

The authors would like to thank the Air Force Office of Scientific Research and the European Office of Aerospace Research and Developement for the Grant support and especially Mr. M. Birkan PhD. and S. Lazdinis PhD. for their help and valuable advices. For typing and formatting this report the authors would like to thank Mr. B. Glocker Dipl. Ing. and Mr. J. Nuding.

A. Appendices

A.1 Influence of the Magnetic Field on the Heat-flux within an Electrically Charged Plasma-component

It has been shown previously¹ that in a relaxation free plasma (distribution functions of different gascomponents adjust themselves immediately to a given special condition) the distribution function $f_i^{(0)}$ due to gradients becomes perturbed and can be written in first approximation by

$$f_i^{(p)} \simeq f_i^{(0)} - \Delta \vec{\xi}_i \cdot \nabla f_i^{(0)} \quad (\text{A.1})$$

where $f_i^{(0)}$ is the Maxwell Boltzmann distribution

$$f_i^{(0)} = n_i \left(\frac{m_i}{2\pi k T_i} \right)^{\frac{3}{2}} \exp \left(\frac{-m_i}{2k T_i} \vec{V}_i^2 \right) \quad (\text{A.2})$$

and $\Delta \vec{\xi}_i$ represent a vector element with the dimension of a length the absolute value of which corresponds to a mean free path i. e. the probability length along which a test particle sustains and transports its velocity \vec{V}_i or its distribution properties. In that derivation one has assumed so far that no external field effects are present. If one now allows that a magnetic induction field \vec{B} is present, one has to account for the fact that the "statistical motion" of a $Z_i e$ - charged particle proceed not anymore along a straight line but rather along a circular or helical line caused by the magnetic force $Z_i e (\vec{V}_i \times \vec{B})$.² In the following one now considers a magnetic field \vec{B} perpendicular to the gradient of the distribution function $f_i^{(0)}$.

In the presents of a magnetic field it is therefore convenient to express the length vector-element by the sum of two vectors: $\Delta \vec{\xi}_{i\parallel}$ which is parallel and $\Delta \vec{\xi}_{i\perp}$ which is perpendicular with respect to \vec{B} . Hence

$$\Delta \vec{\xi}_i = \Delta \vec{\xi}_{i\parallel} + \Delta \vec{\xi}_{i\perp} \quad (\text{A.3})$$

Within a magnetic induction field \vec{B} a test particle with the electric charge $Z_i e$ and the peculiar velocity $\vec{V}_i = \vec{V}_{i\parallel} + \vec{V}_{i\perp}$ (\parallel parallel, \perp perpendicular with respect to \vec{B}) moves along a circular or helical line with a Lamorradius given by

$$\vec{r}_L = \frac{m_i}{Z_i e} \frac{[\vec{V}_i \times \vec{B}]}{\vec{B}^2}, \quad |\vec{r}_L| = r_L = \frac{m_i}{Z_i e} \frac{|\vec{V}_{i\perp}|}{B} \quad (\text{A.4})$$

the statistical pathlength is now given by

$$\begin{aligned} |\Delta \vec{\xi}| \equiv \Delta s &= \sqrt{(\Delta s_{\perp})^2 + (\Delta s_{\parallel})^2} \\ &= \frac{1}{v_i} |\vec{V}_i| = \frac{1}{v_i} \sqrt{\vec{V}_{i\perp}^2 + \vec{V}_{i\parallel}^2} \end{aligned} \quad (\text{A.5})$$

¹Interim Scientific Report "Basic Processes of Plasm propulsion" Grant AFSOR 86-0337, covering period 1.Aug 1988 - 31.July 1989

²one may here approximate the test particle velocity \vec{v}_i by its peculiar velocity \vec{V}_i as long as the average thermal speed is much larger than the relative drift velocity between the colliding particles

where

$$\begin{aligned}\Delta s_{\perp} &= \frac{1}{\nu_i} |\vec{V}_{i\perp}| \\ \Delta s_{\parallel} &= \frac{1}{\nu_i} |\vec{V}_{i\parallel}| \end{aligned} \quad (\text{A.6})$$

and

$$\nu_i = \sum_{\nu(i)} \frac{8}{3} \sqrt{\frac{2}{\pi}} n_{\nu} Q_{i\nu} \frac{\sqrt{m_{\nu} k T_{\nu}}}{m_i + m_{\nu}} \quad (\text{A.7})$$

is the average collision frequency of the test particle i , and $Q_{i\nu}$ the effective collision cross section between particle i and ν . According to eq. (A.4), it follows from Fig.(A.1)

$$\Delta s_{\perp} = 2r_L \varphi \quad (\text{A.8})$$

and for the secant, $\Delta a = |\Delta \vec{\xi}_{i\perp}|$ one obtains

$$\Delta a = 2r_L |\sin \varphi| \quad (\text{A.9})$$

Based on eqs. (A.8), (A.6) and (A.4) it follows

$$2\varphi = \frac{\Delta s_{\perp}}{r_L} = \frac{Z_i e B}{m_i \nu_i} \equiv \omega_i \tau_i \quad (\text{A.10})$$

where ω_i is the cyclotron frequency of the particle i

$$\omega_i = \frac{Z_i e B}{m_i} \quad (\text{A.11})$$

and τ_i is the average collision time

$$\tau_i = \frac{1}{\nu_i} \quad (\text{A.12})$$

The length vector element, $\Delta \vec{\xi}_i$, in the perturbation term $-\Delta \vec{\xi} \cdot \nabla f_i^{(0)}$ can now be written by

$$\Delta \vec{\xi}_i = \frac{1}{\nu_i} \vec{V}_{i\parallel} + \Delta \vec{\xi}_{i\perp} \quad (\text{A.13})$$

where the length vector element normal to \vec{B} (see Fig. (A.1) follows by

$$\Delta \vec{\xi}_{i\perp} = \vec{X} - 2\vec{r}_L \quad (\text{A.14})$$

Now it is

$$\vec{X} = \pm 2\vec{r}_L \sin \left(\frac{\pi - 2\varphi}{2} \right) \frac{[\Delta \vec{\xi}_{i\perp} \times \vec{B}]}{\Delta a \cdot B} \quad (\text{A.15})$$

where the sign of $\sin \left(\frac{\pi - 2\varphi}{2} \right) = \cos \varphi$ alternates between plus and minus depending on φ lies within a range $n\pi \leq \varphi \leq (n+1)\pi$ with even ($n = 0, 2, 4 \dots$) or uneven ($n = 1, 3, 5 \dots$) numbers for n , respectively. Together with eq.(A.4) and eq.(A.9), one obtains

$$\Delta \vec{\xi}_{i\perp} = \frac{\pm \cos \varphi}{|\sin \varphi|} \frac{1}{B} [\Delta \xi_{i\perp} \times \vec{B}] - 2 \frac{m_i}{Z_i e B^2} [\vec{V}_{i\perp} \times \vec{B}] \quad (\text{A.16})$$

In order to eliminate $\Delta \vec{\xi}_{i\perp}$ on the right side of this equation, one takes the vector product of the equation and obtains

$$[\Delta \vec{\xi}_{i\perp} \times \vec{B}] = -\frac{\pm \cos \varphi}{|\sin \varphi|} \cdot B \Delta \vec{\xi}_{i\perp} + 2 \frac{m_i}{Z_i e} \vec{V}_{i\perp} \quad (\text{A.17})$$

Indroced into the equation of $\Delta \vec{\xi}_{i\perp}$, one obtains

$$\Delta \vec{\xi}_{i\perp} = \frac{\pm \cos \varphi}{|\sin \varphi|} \frac{1}{B} \left\{ -\frac{\pm \cos \varphi}{|\sin \varphi|} \cdot B \Delta \vec{\xi}_{i\perp} + 2 \frac{m_i}{Z_i e} \vec{V}_{i\perp} \right\} - 2 \frac{m_i}{Z_i e B^2} [\vec{V}_{i\perp} \times \vec{B}] \quad (\text{A.18})$$

and solved for $\Delta \vec{\xi}_{i\perp}$, one finally ends up with

$$\begin{aligned} \Delta \vec{\xi}_{i\perp} &= \pm 2 |\sin \varphi| \cos \varphi \frac{m_i}{Z_i e B} \vec{V}_{i\perp} - 2 \sin^2 \varphi \frac{m_i}{Z_i e B^2} [\vec{V}_{i\perp} \times \vec{B}] \\ &= \sin 2\varphi \frac{m_i}{Z_i e B} \vec{V}_{i\perp} - 2(1 - \cos 2\varphi) \frac{m_i}{Z_i e B^2} [\vec{V}_{i\perp} \times \vec{B}] \end{aligned} \quad (\text{A.19})$$

or together with eq.(A.10)

$$\Delta \vec{\xi}_{i\perp} = \frac{1}{\nu} \left\{ \frac{\sin \omega_i \tau_i}{\omega_i \tau_i} \vec{V}_{i\perp} - \frac{1 - \cos \omega_i \tau_i}{\omega_i \tau_i} \frac{1}{B} [\vec{V}_{i\perp} \times \vec{B}] \right\} \quad (\text{A.20})$$

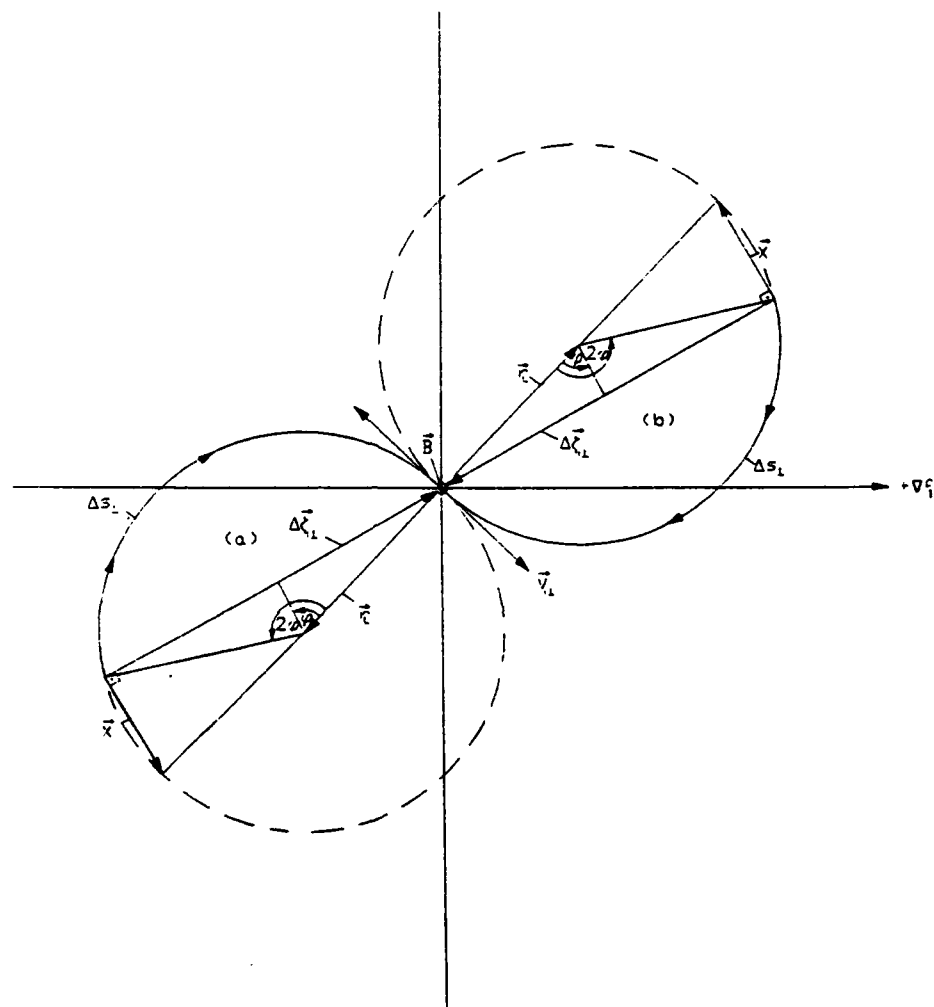


Figure A.1: Illustration of the Particle Motion within a Magnetic Induction Field, \vec{B} , normal to the Gradient, ∇f_i : (a) $\vec{V}_{i\perp}$ towards ∇f_i ; (b) $\vec{V}_{i\perp}$ opposite to ∇f_i (\vec{B} normal to plane).

The entire vector element is now given according to eq.(A.20) by

$$\Delta \vec{\xi}_i = \frac{1}{\nu_i} \vec{V}_{i\parallel} + \frac{\sin \omega_i \tau_i}{\omega_i \tau_i} \frac{1}{\nu_i} \vec{V}_{i\perp} - \frac{1 - \cos \omega_i \tau_i}{\omega_i \tau_i} \frac{1}{B \nu_i} [\vec{V}_{i\perp} \times \vec{B}] \quad (\text{A.21})$$

The perturbation term in eq.(A.1) follows therefore for the restricted case in which the magnetic induction field \vec{B} is perpendicular to the gradient, $\nabla f_i^{(0)}$, by

$$\begin{aligned} -\Delta \vec{\xi}_i \cdot \nabla f_i^{(0)} &= - \left\{ \frac{\sin \omega_i \tau_i}{\omega_i \tau_i} \frac{1}{\nu_i} \vec{V}_{i\perp} - \frac{1 - \cos \omega_i \tau_i}{\omega_i \tau_i} \frac{1}{B \nu_i} [\vec{V}_{i\perp} \times \vec{B}] \right\} \cdot \nabla f_i^{(0)} \\ &= - \left\{ \frac{\sin \omega_i \tau_i}{\omega_i \tau_i} \frac{1}{\nu_i} \vec{V}_i - \frac{1 - \cos \omega_i \tau_i}{\omega_i \tau_i} \frac{1}{B \nu_i} [\vec{V}_i \times \vec{B}] \right\} \cdot \nabla f_i^{(0)} \end{aligned} \quad (\text{A.22})$$

Both expressions are identical since the directional derivations of $\vec{V}_{i\perp} \cdot \nabla \dots$ and $\vec{V}_i \cdot \nabla \dots$ and $[\vec{V}_{i\perp} \times \vec{B}] \cdot \nabla \dots$ and $[\vec{V}_i \times \vec{B}] \cdot \nabla \dots$ give the same results respectively (∇f is perpendicular to \vec{B}).

Since for f_i the following normalization requirement must be fulfilled

$$M_{0i} = \int f_i d\vec{V}_i = n_i \quad (\text{A.23})$$

one has still to normalize the perturbed distribution function $f_i^{(p)}$. For $f_i^{(p)}$ this zero moment becomes not exactly n_i (see the following side calculation)

$$\begin{aligned} M_{0i}^{(p)} &= \int f_i^{(p)} d\vec{V}_i \\ &= n_i \left(1 - \frac{\sin(\omega_i \tau_i)}{\omega_i \tau_i} \frac{1}{\nu_i} \nabla \vec{v}_i + \frac{1 - \cos^2(\omega_i \tau_i)}{\omega_i \tau_i} \frac{2}{\nu_i} \right) \cdot \\ &\quad \cdot \int_{\vec{\xi}=-\infty}^{+\infty} \vec{\xi}_i \frac{[\vec{\xi}_i \times \vec{B}]}{B} \cdot \nabla \vec{v}_i e^{-\xi_i^2} d\vec{\xi}_i \end{aligned}$$

with $\vec{\xi}_i = \sqrt{\frac{m_i}{2kT_i}} \vec{V}_i$.

Now it is

$$\begin{aligned} &\frac{2}{\nu_i} \int_{-\infty}^{+\infty} \vec{\xi}_i \frac{[\vec{\xi}_i \times \vec{B}]}{B} \cdot \nabla \vec{v}_i e^{-\xi_i^2} d\vec{\xi}_i = \\ &= \frac{2}{\nu_i B} \int \int \int \xi_x \left[(\xi_y B_z - \xi_z B_y) \frac{\partial}{\partial x} \vec{v}_{ix} + (\xi_z B_x - \xi_x B_z) \frac{\partial}{\partial y} \vec{v}_{ix} + (\xi_x B_y - \xi_y B_x) \frac{\partial}{\partial z} \vec{v}_{ix} \right] + \\ &+ \xi_y \left[(\xi_y B_z - \xi_z B_y) \frac{\partial}{\partial x} \vec{v}_{iy} + (\xi_z B_x - \xi_x B_z) \frac{\partial}{\partial y} \vec{v}_{iy} + (\xi_x B_y - \xi_y B_x) \frac{\partial}{\partial z} \vec{v}_{iy} \right] + \\ &+ \xi_z \left[(\xi_y B_z - \xi_z B_y) \frac{\partial}{\partial x} \vec{v}_{iz} + (\xi_z B_x - \xi_x B_z) \frac{\partial}{\partial y} \vec{v}_{iz} + (\xi_x B_y - \xi_y B_x) \frac{\partial}{\partial z} \vec{v}_{iz} \right] e^{-\xi_x^2 - \xi_y^2 - \xi_z^2} d\xi_x d\xi_y d\xi_z \\ &= \frac{1}{\nu_i B} [\vec{B} \times \nabla] \cdot \vec{v}_i \\ &= \frac{1}{\nu_i B} [\nabla \times \vec{v}_i] \cdot \vec{B} \end{aligned}$$

and therefore

$$\begin{aligned} M_{0i}^{(p)} &= n_i \left(1 - \frac{\sin(\omega_i \tau_i)}{\omega_i \tau_i} \frac{1}{\nu_i} \nabla \vec{v}_i + \frac{1 - \cos(\omega_i \tau_i)}{\omega_i \tau_i} \frac{1}{\nu_i B} [\nabla \times \vec{v}_i] \cdot \vec{B} \right) \\ &\neq n_i \end{aligned}$$

Now, the proper normalized distributionfunction f_i under perturbed conditions with temperature and density gradients follows according to this result from eq. (A.1) by

$$f_i = \frac{f_i^{(0)} - \frac{\sin(\omega_i \tau_i)}{\omega_i \tau_i} \frac{1}{\nu_i} \vec{V}_i \cdot \nabla f_i^{(0)} + \frac{1 - \cos(\omega_i \tau_i)}{\omega_i \tau_i} \frac{1}{\nu_i B} [\vec{V}_i \times \vec{B}] \cdot \nabla f_i^{(0)}}{1 - \frac{\sin(\omega_i \tau_i)}{\omega_i \tau_i} \frac{1}{\nu_i} \nabla \vec{v}_i + \frac{1 - \cos(\omega_i \tau_i)}{\omega_i \tau_i} \frac{1}{\nu_i B} [\nabla \times \vec{v}_i] \cdot \vec{B}} \quad (\text{A.24})$$

It may be of interest to note here that for

$$|\omega_i \tau_i| = \left| \frac{Z_i e}{m_i \nu_i} B \right| \ll 1$$

the distribution function f_i becomes effectively independent of \vec{B} and assumes the known form as calculated before under the assumption of no external field³. The heatflux vector due to conduction follows now by

$$\vec{q}_i = \int \frac{1}{2} m_i \vec{V}_i^2 \vec{V}_i d\vec{V}_i \quad (\text{A.25})$$

By replacing f_i according to eq.(A.24) and summation over the velocity-space, one eventually obtains the heatflux vector due to conduction within a magnetic field normal to ∇f_i (i.e. normal to $\nabla T_i, \nabla n_i$) by

$$\vec{q}_i = -\frac{5n_i (kT_i)^2}{2\nu_i m_i} \cdot \frac{1}{1 - \frac{\sin(\omega_i \tau_i)}{\omega_i \tau_i} \frac{1}{\nu_i} \nabla \vec{v}_i + \frac{1 - \cos(\omega_i \tau_i)}{\omega_i \tau_i} \frac{1}{\nu_i} B [\nabla \times \vec{v}_i] \cdot \vec{B}} \cdot \left\{ \frac{\sin \omega_i \tau_i}{\omega_i \tau_i} \left[\frac{1}{n_i} \nabla n_i + \frac{2}{T_i} \nabla T_i \right] - \frac{1 - \cos \omega_i \tau_i}{\omega_i \tau_i} \left[\frac{[\vec{B} \times \nabla n_i]}{n_i B} + 2 \frac{[\vec{B} \times \nabla T_i]}{T_i B} \right] \right\} \quad (\text{A.26})$$

where

$$\begin{aligned} \omega_i &= \frac{Z_i e |B|}{m_i} \\ \tau_i &= \frac{1}{\nu_i} = \frac{1}{\sum_{\nu(i=1)} n_\nu \frac{4}{3} \sqrt{\frac{2}{\pi}} Q_{i\nu} \frac{\sqrt{m_\nu k T_\nu}}{m_i + m_\nu}} \end{aligned} \quad (\text{A.27})$$

Noteworthy is the fact that for $|\omega_i \tau_i| > 0$ the heatflux vector has a component not only parallel to the temperature and density gradients, but also in the direction normal to \vec{B} and $\nabla n_i, \nabla T_i$. For increasing $|\omega_i \tau_i|$ values the heat flux in the direction of $\nabla n_i, \nabla T_i$ decreases and the flux normal to \vec{B} and the gradients increases at first reaches a maximum and then decreases. For $|\omega_i \tau_i| = \pi, 2\pi, 3\pi, \dots$, \vec{q}_i diminishes. If one takes $\nabla n_i = \frac{\partial n_i}{\partial T_i} \nabla T_i$, and since for most cases

$$\frac{1}{\nu_i} \nabla \vec{v}_i \ll 1 \text{ and } \frac{1}{\nu_i} [\nabla \times \vec{v}_i] \ll 1 \quad (\text{A.28})$$

one can write the heat flux vector due to conduction in good approximation by

$$\begin{aligned} \vec{q}_i &= -n_i \frac{5k^2 T_i}{\nu_i m_i} \left[1 + \frac{T_i}{2n_i} \frac{\partial n_i}{\partial T_i} \right] \left\{ \frac{\sin \omega_i \tau_i}{\omega_i \tau_i} \nabla T_i - \frac{1 - \cos \omega_i \tau_i}{\omega_i \tau_i} \cdot \frac{[\vec{B} \times \nabla T_i]}{B} \right\} \\ &\equiv -\vec{\lambda}_i \nabla T_i \end{aligned} \quad (\text{A.29})$$

where now the heatconductioncoefficient becomes a tensor and follows by

$$\vec{\lambda}_i = \lambda_i \cdot \begin{vmatrix} \frac{\sin \omega_i \tau_i}{\omega_i \tau_i} & -\frac{1 - \cos \omega_i \tau_i}{\omega_i \tau_i} \frac{B_x}{B} & -\frac{1 - \cos \omega_i \tau_i}{\omega_i \tau_i} \frac{B_y}{B} \\ \frac{1 - \cos \omega_i \tau_i}{\omega_i \tau_i} \frac{B_x}{B} & \frac{\sin \omega_i \tau_i}{\omega_i \tau_i} & -\frac{1 - \cos \omega_i \tau_i}{\omega_i \tau_i} \frac{B_z}{B} \\ -\frac{1 - \cos \omega_i \tau_i}{\omega_i \tau_i} \frac{B_y}{B} & -\frac{1 - \cos \omega_i \tau_i}{\omega_i \tau_i} \frac{B_z}{B} & \frac{\sin \omega_i \tau_i}{\omega_i \tau_i} \end{vmatrix} \quad (\text{A.30})$$

³Basic Processes of Plasma propulsion, Interim Scient. Report, Grant AFOSR 86-0337, covering period Aug 88 - July 89

with

$$\lambda_i = n_i \frac{5k^2 T_i}{\nu_i m_i} \left[1 + \frac{T_i}{2n_i} \frac{\partial n_i}{\partial T_i} \right] \quad (\text{A.31})$$

For

$$\omega_i \tau_i = \frac{Z_i e |\vec{B}|}{m_i \nu_i} \ll 1$$

the heatconduction coefficient becomes a scalar and independent of the magnetic field, \vec{B} ; it then assumes the form of the classical conduction coefficient as derived elsewhere [1] what has to be expected. For noticable values $|\omega_i \tau_i| \geq 0.1$, however, the heatconduction coefficient is a tensor the elements of which become periodically zero for $\omega_i \tau_i = n\pi$ with $n = 1, 2, 3, \dots$; and their relative maximas inbetween become smaller the larger the $|\omega_i \tau_i|$ values.

A.2 Determination of the Temperature profile within the Constrictor

In order to calculate the temperature profile within the current carrying plasmachannel of the constrictor (see Fig. A.1) one solves within the range $0 \leq r \leq r_c$ the energy equation of the electrons under the assumption that (a) the axial temperature gradient can be neglected besides the radial one, (b) the temperature difference between electrons and heavy particles like atoms and ions is negligible ($T_e = T$) and (c) the current density can be modelled by a paraboloid of grade n according to

$$j = \hat{j} \left[1 - \left\{ \frac{r}{r_c} \right\}^n \right] \quad (\text{A.32})$$

where

$$\hat{j} = \frac{n+2}{n} \frac{I}{\pi r_c^2} \quad (\text{A.33})$$

results from the requirement

$$I = 2\pi \int_0^{r_c} j r dr = \pi r_c^2 \frac{n}{n+2} \hat{j} \quad (\text{A.34})$$

Hence the energy equation for the electrons reduces to

$$\frac{j^2}{\sigma} = -\frac{1}{r} \frac{d}{dr} \left(r \lambda_e \frac{dT_e}{dr} \right) + RL \quad (\text{A.35})$$

Where RL stands for reaction - and radiation losses of the electrons. After integration and rearranging one obtains

$$-2\pi r \lambda_e \frac{dT_e}{dr} = 2\pi \int_0^r \left\{ \frac{j^2}{\sigma} - RL \right\} r dr \quad (\text{A.36})$$

Now, within the arc column the axial voltage drop $\frac{dV}{dz}$ or the electric field E_z can be considered independent of r and since within the throat $j = j_z = \sigma E_z$, it follows

$$\frac{j(r)}{\sigma(r)} = \frac{\hat{j}}{\hat{\sigma}} = \text{const} \quad (\text{A.37})$$

According to eq.(A.36) together with (A.32) and (A.37) one obtains

$$\begin{aligned} -r \lambda_e \cdot \frac{dT_e}{dr} &= \frac{\hat{j}^2}{\hat{\sigma}} \int_0^r \left\{ 1 - \left(\frac{r}{r_c} \right)^n - \frac{RL}{\hat{j}^2/\hat{\sigma}} \right\} r dr \\ &= \frac{\hat{j}^2}{\hat{\sigma}} \left\{ \frac{r^2}{2} - \frac{1}{n+2} \frac{r^{n+2}}{r_c^n} - \int_0^r \frac{RL}{\hat{j}^2/\hat{\sigma}} r dr \right\} \end{aligned} \quad (\text{A.38})$$

The heatconduction coefficient, λ_e of the electrons follows now under the premise that the radial heatflux is not strongly affected by $\omega_e \tau_e$ - effects ($\omega_e \tau_e \leq 0.1$) as

$$\lambda_e = c_\lambda \cdot T_e^{\frac{5}{2}} \left[\frac{W}{mK} \right] \quad (\text{A.39})$$

and the electric conductivity as

$$\sigma = c_\sigma \cdot T_e^{\frac{3}{2}} \left[\frac{A}{mV} \right] \quad (\text{A.40})$$

where c_λ and c_σ are coefficients which are only weakly temperature - and pressure dependent, at least as long the degree of ionisation is larger than a few percent.

$$c_\lambda \simeq \frac{2.88 \cdot 10^{-10}}{\ln \left(5.7 \cdot 10^{-3} \frac{T_e}{p_e^{\frac{1}{2}}} \right)} \left\{ 1 + \frac{T_e}{2n_e} \frac{\partial n_e}{\partial T_e} \right\} \left[\frac{W}{mK^{\frac{1}{2}}} \right] \quad (\text{A.41})$$

$$c_\sigma \simeq \frac{3.88 \cdot 10^{-3}}{\ln \left(5.7 \cdot 10^{-3} \frac{T_e}{p_e^{\frac{1}{2}}} \right)} \left[\frac{A}{VmK^{\frac{1}{2}}} \right] \quad (\text{A.42})$$

If one now replaces in eq.(A.38) λ_e and $\hat{\sigma}$ according to eq.(A.33) and eq.(A.40), respectively, and \hat{j} according to eq.(A.33), one obtains after integration

$$\hat{T}_e^{\frac{1}{2}} - T_e^{\frac{1}{2}} = \frac{7}{8\pi^2} \frac{I^2}{\bar{c}_\lambda c_\sigma \hat{T}_e^{\frac{3}{2}} r_c^2} \left(1 + \frac{2}{n} \right)^2 \left(\frac{r}{r_c} \right)^2 \left\{ 1 - \frac{4}{(n+2)^2} \left(\frac{r}{r_c} \right)^n - \xi(r) \right\} \quad (\text{A.43})$$

where

$$\xi(r) = \frac{4}{r^2} \int_0^r \frac{1}{r} \left(\int_0^r \frac{RL}{\hat{j}^2 \hat{\sigma}} r dr \right) dr \quad (\text{A.44})$$

depends on the radiationloss RL and can be considered small compared with one. One can show that for a hydrogen plasma at a pressure below about 5 bar this assumption is justified. \bar{c}_λ is an average value of c_λ which is defined by

$$\bar{c}_\lambda = \frac{7 \int_{T_e}^{\hat{T}_e} c_\lambda T_e^{\frac{3}{2}} dT_e}{2 \left(\hat{T}_e^{\frac{1}{2}} - T_e^{\frac{1}{2}} \right)} \quad (\text{A.45})$$

with $T_e \sim 6000K$ One may now assume that the temperature $T_e(r_c) \sim 6000K$ at the edge of the arc core is quite smaller than the maximum temperature \hat{T}_e in the center of the core, i.e. $T_e^{\frac{1}{2}} \ll \hat{T}_e^{\frac{1}{2}}$. Hence from the above equation the maximum temperature follows with $r = r_c$ by

$$\hat{T}_e = \left\{ \frac{7}{8\pi^2 \bar{c}_\lambda c_\sigma} \right\}^{\frac{1}{2}} \cdot \left(\frac{I}{r_c} \right)^2 \cdot \left\{ \left(1 + \frac{4}{n} \right) \left[1 - \frac{(n+2)^2}{n(n+4)} \cdot \xi(r_c) \right] \right\}^{\frac{1}{2}} \quad (\text{A.46})$$

In order to get the temperature profile, one now replaces in eq.(A.43) the following expression according to eq.(A.46)

$$\frac{7}{8\pi^2 \bar{c}_\lambda c_\sigma} \left(\frac{I}{r_c} \right)^2 = \frac{\hat{T}_e^{\frac{5}{2}}}{\left(1 + \frac{4}{n} \right) \left\{ 1 - \frac{(n+2)^2}{n(n+4)} \xi(r_c) \right\}}$$

One obtains

$$\hat{T}_e^{\frac{1}{2}} - T_e^{\frac{1}{2}} = \hat{T}_e^{\frac{1}{2}} \left(\frac{r}{r_c} \right)^2 \frac{(1 + \frac{2}{n})^2}{1 + \frac{4}{n}} \left[\frac{1 - \frac{4}{(n+2)^2} \left(\frac{r}{r_c} \right)^n - \xi(r)}{1 - \frac{(n+2)^2}{n(n+4)} \xi(r_c)} \right]$$

and solved for T_e yields

$$T_e = \hat{T}_e \left\{ 1 - \frac{(n+2)^2}{n(n+4)} \left(\frac{r}{r_c} \right)^2 \frac{1 - \frac{4}{(n+2)^2} \left(\frac{r}{r_c} \right)^n - \xi(r)}{1 - \frac{(n+2)^2}{n(n+4)} \xi(r_c)} \right\}^{\frac{2}{3}} \quad (\text{A.47})$$

The dimensionless temperature profile, $\frac{T_e}{T_e(r_c)}$, is now plotted in Fig.(A.2) for different current density exponents, n . As can be shown, the ξ - dependency can be neglected within this model approach as long as $\xi(r_c) \simeq \xi \leq 0.2$.

In order to determine the maximum electron temperature, \hat{T}_e , one starts from eq.(A.46) replaces \bar{c}_λ according to eq.(A.43) and c_σ according to (A.40), respectively, and obtains

$$\hat{T}_e = 1.513 \cdot 10^2 \cdot J_0 \gamma \left(\frac{I}{r_c} \right) \quad [K] \quad (\text{A.48})$$

where the factor J_0 is now given by

$$J_0 = \left\{ \left(1 + \frac{4}{n} \right) \left[1 - \frac{(n+2)^2}{n(n+4)} \xi(r_c) \right] \right\}^{\frac{1}{2}} \quad (\text{A.49})$$

and tabulated for different n and ξ (see Table A.1), and γ is a dimensionless factor of the order one which follows for singly ionized gases by

$n=$	1,5	2	3	4	10	100
$\xi=0$	1,297	1,246	1,185	1,149	1,070	1,008
0,1	1,256	1,211	1,155	1,122	1,047	0,987
0,15	1,233	1,191	1,139	1,107	1,034	0,976
0,2	1,209	1,171	1,122	1,092	1,021	0,964

Table A.1: $J_0(n, \xi)$

$$\gamma = \gamma(\hat{T}_e, p) = \gamma^* \cdot \left\{ \ln \left[5.7 \cdot 10^{-3} \cdot \frac{\hat{T}_e}{p^{\frac{1}{2}}} \right] \right\}^{\frac{1}{2}} \quad (\text{A.50})$$

with

$$\gamma^* = \left[\frac{7}{4(\hat{T}_e^{\frac{1}{2}} - T_e^{\frac{1}{2}})} \int_{T_e}^{\hat{T}_e} \frac{\left(1 + \frac{T_e}{2n_e} \frac{\partial n_e}{\partial T_e} \right) \cdot T_e^{\frac{3}{2}}}{\ln \left[5.7 \cdot 10^{-3} \cdot \frac{T_e}{p^{\frac{1}{2}}} \right]} dT_e \right]^{-\frac{1}{2}} \quad (\text{A.51})$$

and $T_e \simeq 6000K$. The numerical factor in eq. (A.48) has the dimension $[Km^{\frac{3}{2}}/A^{\frac{3}{2}}]$. If one now assumes local reaction equilibrium according to "Saha-Eggert",⁴ one obtains the degree of ionization for a singly ionized plasma by

$$\alpha = \frac{n_e}{\sum_{\nu \neq e} n_\nu} = \frac{\sum_{\nu \neq e} Z_\nu n_\nu}{\sum_{\nu \neq e} n_\nu} = \left\{ 1 + \frac{p}{c_1 T^{\frac{3}{2}} \exp(-c_2/T)} \right\}^{-1} \quad (A.52)$$

where

$$c_1 = \frac{u_1 \cdot 2 (2\pi m_e)^{\frac{3}{2}}}{u_0 h^3} k^{\frac{3}{2}} \quad (A.53)$$

$$c_2 = \frac{\chi_{01}}{k} \quad (A.54)$$

The expression $\frac{u_1 \cdot 2}{u_0}$ is the quotient of the partition- functions and of the order one, m_e is the electron mass, k is the Boltzmannconstant and h is Planck constant; χ_{01} is the ionization energy. With the knowledge of α and the premise that within the constrictor $T_e = T$, one can replaced p_e and $\frac{T_e}{n_e} \frac{\partial n_e}{\partial T_e}$ in eq.(A.51) by

$$p_e = n_e k T_e = \frac{\alpha}{1 + \alpha} p \quad (A.55)$$

and for a singly ionized plasma the second expression by

$$\frac{T_e}{n_e} \frac{\partial n_e}{\partial T_e} = - \left\{ 1 - \frac{1}{2} (1 - \alpha) \left[\frac{5}{2} + \frac{c_2}{T_e} \right] \right\} \quad (A.56)$$

n=	1,5	2	3	4	10	100
$\xi=0$	0,736	0,743	0,751	0,757	0,770	0,778
0,05	0,733	0,740	0,750	0,756	0,770	0,778
0,1	0,728	0,737	0,748	0,754	0,69	0,778
0,2	0,716	0,728	0,742	0,751	0,768	0,778
0,4	-	0,693	0,724	0,738	0,765	0,777
0,6	-	-	0,655	0,704	0,757	0,777

Table A.2: $J_1(n, \xi)$

The integral γ^* can now be calculated for a hydrogen plasma as function of \hat{T}_e and $p(=const)$ and finally γ , the expression of eq.(A.50). The somewhat lengthy but straight forward numerical procedure leads to a function $\gamma = \gamma(p, \hat{T}_e)$ which is plotted in Fig.(A.3) for different pressures in a temperaturerange between about 10000K and 50000K. Within this range the dimensionsless factor γ can be well approximated (with an error of less than 3%) by the relation

$$\gamma = 9.35 \cdot 10^{-2} [\hat{T}_e - 2230]^{\frac{1}{4}} - 4.34 \cdot 10^{-2} \ln \left(\frac{p}{10^5} \right) \quad (A.57)$$

where \hat{T}_e is taken in Kelvin and p in Pascal. Knowing γ as function of \hat{T}_e and p , one now can determine from eq.(A.48) the maximum electrontemperature, \hat{T}_e , as function of $\frac{I}{r_c}$, p , n and $\xi(r_e)$. For a current density profile given by a paraboloid with an exponent of

⁴Unsöld, " Physik der Sternatmosphäre ", Springer Book [25]

$n = 4$ and a loss coefficient of $\xi \approx 0$, the maximum electron temperature, \hat{T}_e has been calculated according to eqs.(A.48), (A.51), (A.52) and (A.57) as function of $\frac{I}{r_c}$ and p . The results are plotted in Fig.(A.4).

For a plasma with one and more times ionized particles one can now determine γ in an analog way as it is done for hydrogen in eq.(A.50). One obtains now

$$\gamma = \gamma^* \left\{ \ln \left[5.7 \cdot 10^{-3} \frac{\hat{T}_e}{p^{\frac{1}{2}}} \right] \cdot \left(1 + \sum_{\nu \geq 2} \frac{n_\nu}{n_e} \left[\frac{Q_{e\nu}}{Q_{e1}} - Z_\nu \right] \right) \right\}^{\frac{1}{2}} \quad (\text{A.58})$$

where γ^* is again given by eq.(A.51). The ratios of the collision cross sections (with $\nu \geq 1$)

$$Q_{e\nu} = \left(\frac{Z_\nu e^2}{\epsilon_0 k \hat{T}_e} \right)^2 \cdot \frac{\ln \left\{ 1 + 144 \pi^2 \frac{e^3 k^3 \hat{T}_e^3}{n_e e^6 Z_\nu (Z_\nu + 1)} \right\}}{64 \pi} \quad (\text{A.59})$$

are mainly functions of Z_ν^2 and in addition to a minor extend a function of the quantities under the \ln - termes. For an Argon plasma allowing singly - and doubly ionized particles, the dimensionless quantity, γ has been calculated by taking a local "Saha equilibrium". The somewhat involved calculation finally leads to an expression which depends on \hat{T}_e and p again. The expression for γ can now be well approximated by

$$\gamma \approx 1.25 \cdot 10^{-5} \left\{ 1 - 0.22 \ln \left(\frac{p}{10^5} \right) \right\} \cdot \hat{T}_e + 0.85 \quad (\text{A.60})$$

The relative error of this formula amounts to about $\pm 5\%$ within the range for \hat{T}_e and p given by $14000K \leq \hat{T}_e \leq 40000K$ and $10^3 Pa \leq p \leq 3 \cdot 10^5 Pa$, respectively. The maximum electron temperature, \hat{T}_e , within the core of an argon arc follows therefor from the eqs.(A.48) and (A.60) by

$$\hat{T}_e = \frac{129 \cdot J_0}{1 - 1.89 \cdot 10^{-3} \left\{ 1 - 0.22 \ln \left(\frac{p}{10^5} \right) \right\} \cdot J_0 \cdot \left(\frac{I}{r_c} \right)^{\frac{2}{3}}} \cdot \left(\frac{I}{r_c} \right)^{\frac{2}{3}} \quad (\text{A.61})$$

where J_0 is slightly varying function depending on n and $\xi(r_c)$ and given according to Table (A.1).

In addition to the temperature maximum \hat{T}_e within the arc channel of the constrictor one is interested in the average electron temperature defined by

$$\bar{T}_e = \frac{2}{r_c^2} \int_{r=0}^{r_c} T_e r dr \quad (\text{A.62})$$

Replacing T_e in the integrand by eq.(A.42), one obtains

$$\begin{aligned} \bar{T}_e &= 2\hat{T}_e \cdot \int_{\frac{r}{r_c}=0}^1 \left\{ 1 - \frac{(n+2)^2}{n(n+4)} \left(\frac{r}{r_c} \right)^2 \cdot \frac{1 - \frac{4}{(n+2)^2} \left(\frac{r}{r_c} \right)^n - \xi(r)}{1 - \frac{(n+2)^2}{n(n+4)} \xi(r_c)} \right\}^{\frac{2}{3}} \frac{r}{r_c} d\left(\frac{r}{r_c} \right) \\ &\equiv \hat{T}_e \cdot J_1 \end{aligned} \quad (\text{A.63})$$

where the coefficient J_1 is a function of the current density profile exponent, n and the dimensionless quantity, $\xi(r_c) \approx \tilde{\xi} \approx \xi$, which accounts for radiation - and reaction losses. In Table (A.2) this coefficient J_1 , is presented for various values of n and ξ .

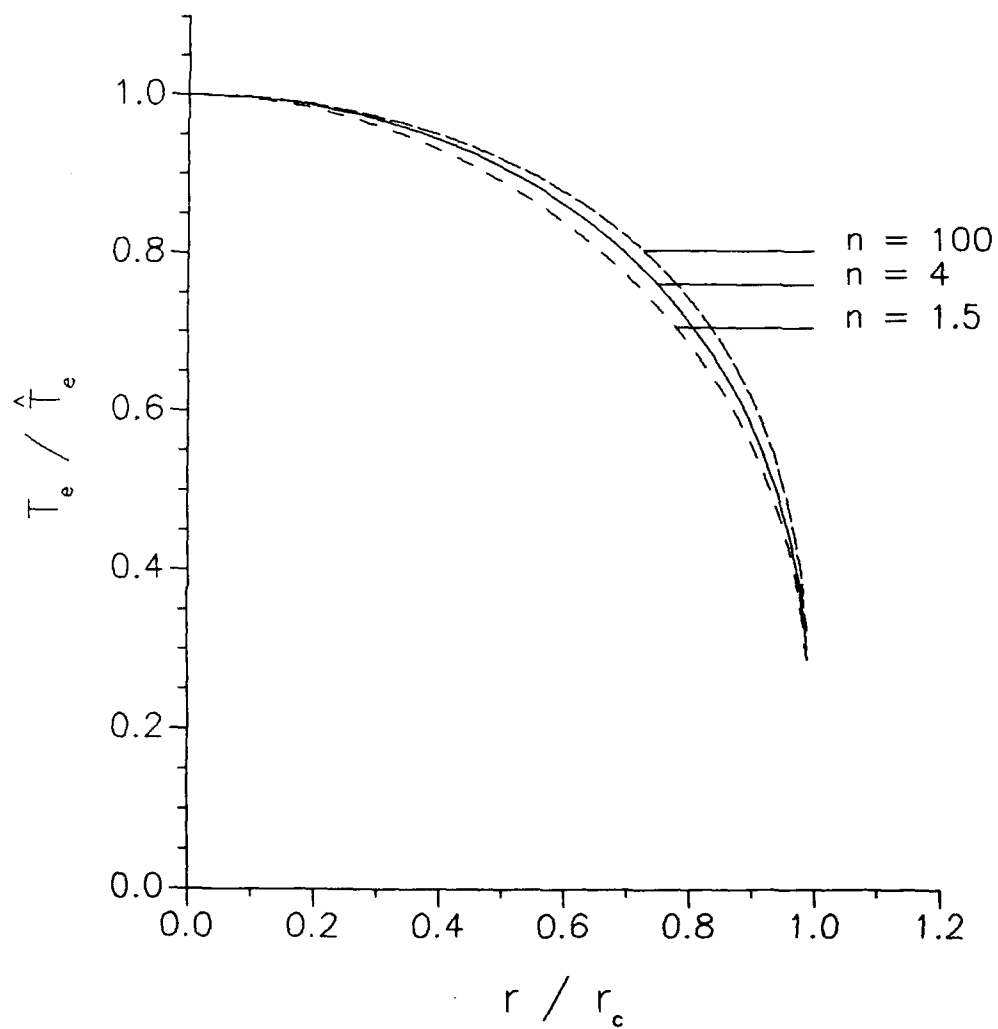


Figure A.2: Temperature Profile for Different Grades n of the Current Density Paraboloids within the Arc Core

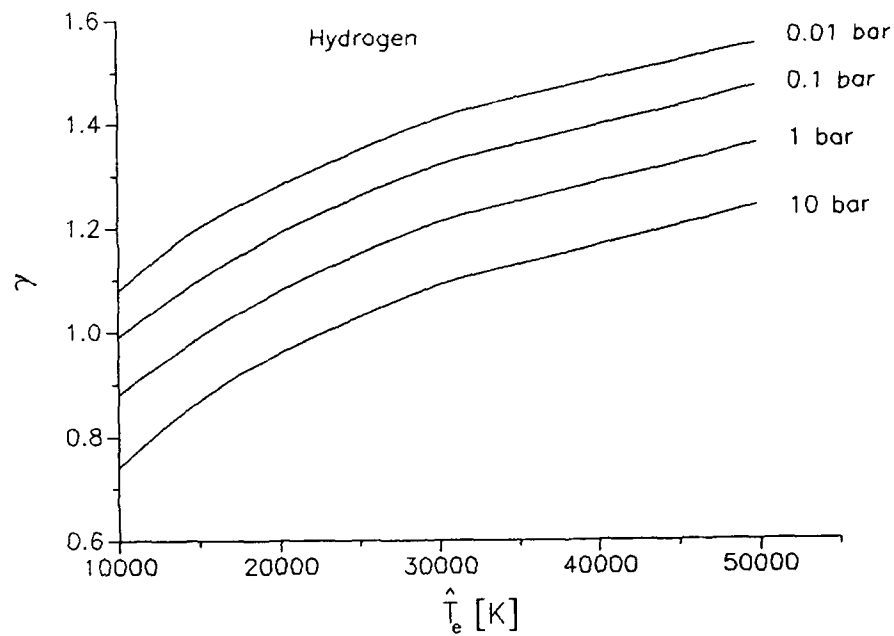


Figure A.3: Plot of γ as Funktion of \hat{T}_e and p as Parameter of Hydrogen as Propellant

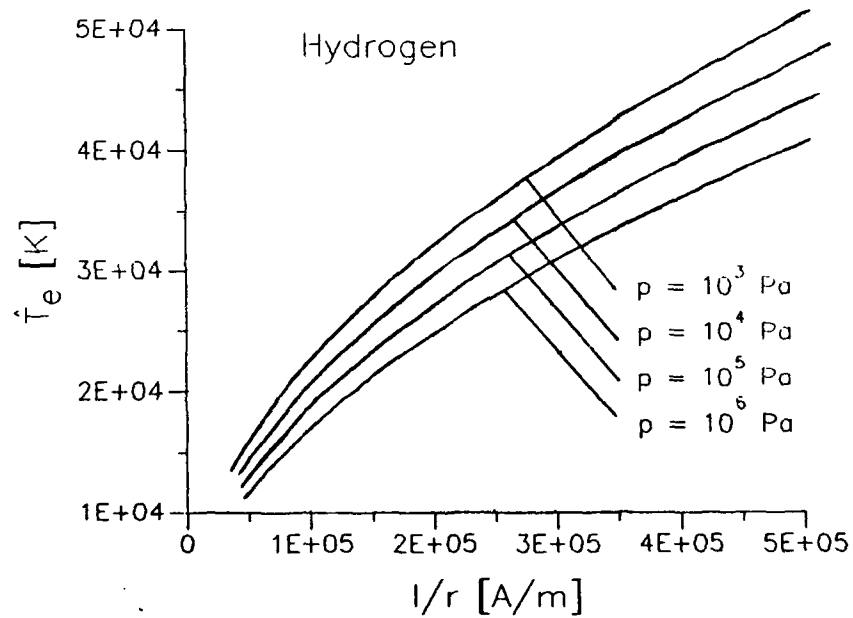


Figure A.4: Maximum Electrontemperature within an Hydrogen Arc Core as Function of the Quotient $\frac{I}{r_c}$ (arc current divided by the core radius) for different pressure p , $n = 4$, $\xi = 0$.

Bibliography

- [1] G.L. Bennet, M.A. Watkins, D.C. Byers and J.W. Barnett, " Enhancing Space Transportation: The NASA Program to Develop Electric Propulsion " ; NASA Tech. Mem. 4244 Oct. 90
- [2] R.D. Smith, C.R. Roberts, K. Davies and J. Vaz, " Development and Demonstration of a 1.8 kW Hydrazine Arcjet Thruster " ; AIAA 90-2447 21. Electr. Propuls. Conf. Orlando, Fl. July 1990
- [3] G. Baiocchi and W. Deininger, " Review of Plasma Propulsion Developments at BPD " ; AIAA 90 - 2559 21. Electr. Propuls. Conf. Orlando, Fl. July 1990
- [4] T. Yamada, Y. Shimizu, K. Toki and K. Kuriki, " Thermal Analysis and Thrust Performance of a Low Power Arcjet Thruster " ; AIAA 90 - 2581, 21. Electr. Propuls. Conf. Orlando, Fl. July 1990
- [5] W.M. Smith, J.C. Andrews, " Interests in Electric Propulsion " ; Proceedings 20th Int. Electr. Propuls. Conf., P.48 Garmisch Partenkirchen, Oct. 1988
- [6] W.D. Deininger, A. Chopra, D.Q. King and T.J. Pivorotto, " Thermal-Design Improvements for 30 kWe Arcjet Engines " , Proceedings 20th Int. Electr. Propuls. Conf. p.416, Garmisch Partenkirchen Oct. 1988
- [7] G. Cruciani, W. Deininger and C. Petagna, " Development of a 1 N radiationcooled Arcjet " , AIAA 90-2536 21 Electr. Propuls. Conf. Orlando, Fl. July 1990 and E. Tosti, H.O. Schrade and C. Petagna; " Test Results of a 15kW Watercooled Arcjet " , AIAA 90-2535 21. Electr. Propuls. Conf. Orlando, Fl. July 1990
- [8] M. Auwetter-Kurtz and E.W. Messerschmid; " Plasma Accelerator Activities at the University of Stuttgart " , AIAA - 2659 21. Electr. Propuls. Conf. Orlando, Fl. July 1990
- [9] A. Gallimore, A. Kelly and R. Jahn; " Anode Power Deposition in Quasi Steady MPD thrusters " , AIAA 90 -2668 21. Electr. Propuls. Conf. Orlando, Fl. July 1990
- [10] K. Kuriki; " Electric Propulsion Research and Development in Japan " , AIAA 90 - 2676 21. Electr. Propuls. Conf. Orlando, Fl. July 1990

- [11] Hügel H.; " Zur Strömung kompressibler Plasmen im Eigenfeld von Lichtbogenentladungen " , DLR-FB-70-13, 1970. Publishing Col: Wiss. Berichtswesen der DFVLR, Postfach 906058, D-5000 Köln 90.
- [12] Auweter-Kurtz, M., Kurtz H.L., Schrade H.O. and Slezione P.C. ; " Numerical Modeling of the Flow Discharge in MPD-Thrusters " ; Journal of Propulsion and Power, Vol.5 No.1, pp. 49-55, 1989.
- [13] Auweter-Kurtz M., Glaser S.F., Kurtz H.L., Schrade H.O. and Slezione P.C. ; " An Improved Code for Nozzle Type Steady MPD Thrusters " ; IEPC 88-043, 20th International Electric Propulsion Conference, Garmisch-Partenkirchen, 1988.
- [14] Minakuchi H. and Kuriki K. ; " Magnetoplasmdynamic Analysis of Plasma Acceleration " ; 17th International Electric Propulsion Conference, IEPC 84-06, Tokyo, 1984.
- [15] Kimura, I., Toki K. and Tanaka M.; " Current Distribution on the Electrodes of MPD Arcjets " ; AIAA Journal, Vol. 20, No. 7, p. 889, 1982.
- [16] Lawless J.L. and Subramanian V.V.; " A Theory of Onset in MPD Thrusters " ; AFOSR-Report 83-0033, 1983.
- [17] Heimerdinger D. ; " An Approximate Two-Dimensional Analysis of an MPD Thruster " ; SSL 9-84, MIT, Cambridge, Mass., June 1984. and Chanty J.M.G., Martinez-Sanchez M. ; " Two- Dimensional Numerical Simulation of MPD Flows " ; AIAA 87 - 1090 19th International Electric Propulsion Conference, Colorado Springs, CO, 1987.
- [18] Schrade H.O., Auweter-Kurtz M. and Kurtz H.L. ; " Basic Processes of Plasma Propulsion " ; Final Scientific Report, AFOSR Grant 82-0298, Jan. 1987
- [19] Maisenhälder F. and Mayerhofer W.; " Jet-Diagnostics of a Self-Field Accelerator with Langmuir Probes " ; AIAA-Journal, Vol 12, No 9, Sept. 1974, pp. 1203-1209
- [20] Renner A. ; " Berechnung von düsenförmigen Plasmatriebwerken mit unterschiedlicher Geometrie " ; IRS-Nr 90-S12 Studienarbeit, IRS Universität Stuttgart
- [21] Eberle A. ; " Characteristic Flux Averaging Approach to the Solution of Euler's Equations " ; VKI lecture series, Computational fluid dynamics, 1987-04,1987
- [22] Slezione P.C., Auweter-Kurtz M., and Schrade H.O. ; " Numerical Codes for Cylindrical MPD Thrusters " ; IEPC 88-043, 20th International Electric Propulsion Conference, Garmisch-Partenkirchen, 1988.
- [23] Slezione P.C., Auweter-Kurtz M., Glocker B., Gogel T., Götz T. , Messerschmid E., and Schrade H.O. ; " Non-Equilibrium Flow in Arcjets " ; Proc. Conf. Hypersonic Flows for Reentry Problems, Antibes, France, January 1990.

- [24] Slezione P.C., Auweter-Kurtz M., Schrade H.O. and Wegmann T. ; " Comparison of Numerical and Experimental Investigations of MPD Accelerators " ; AIAA 90 - 2663 21. Electr. Propuls. Conf. Orlando, Fl. July 1990
- [25] Unsöld A. ; " Physik der Sternatmosphären " ; Springer, Berlin Heidelberg New York, 1968.
- [26] Finkelnburg W and Maeker H. ; " Elektrische Bögen und thermische Plasmen " ; Handbuch der Physik Bd. XXII, Gasentladungen II, Springer, Berlin 1956.
- [27] Knoll M et. al. ; " Gasentladungstabellen " ; Verlag von Julius Springer Berlin 1935
- [28] Schrade H.O. and Slezione P.C. ; " Basic Processes of Plasma Propulsion " ; Interim scientific Report AFOSR Grant 86-0337, June 1990
- [29] Hügel H ; " Zur Funktionsweise der Anode im Eigenfeldbeschleuniger " ; DFVLR-FB 80-30, 1980.
- [30] J.W. Barnett and J.R. Jahn ; " Operation of the MPD - Thruster with stepped Current Inputs " ; Dissertation for the Degree of Philosophy by J.W. Barnett, Mechan. and Aerospace Engineering Princeton Univ. April 1985. and J.W. Barnett and R.J. Jahn ; " Onset Phenomena in MPD Thrusters " ; AIAA 85 - 2038, Oct 1985
- [31] J.S. Sovey and Mautenicks ; " Performance and Lifetime Assesment of MPD- Arc Thruster Technology " ; NASA Tech. Memorandum 101293, AIAA - 88 - 3211, 24th Joint Propulsion Conf. July 1988
- [32] Kuriki K. and Iida H. ; " Spectrum Analysis of Instabilities in MPD-Arcjet " ; IEPC 84-28, Proceedings of the 17th International Electric Propulsion Conference, Tokyo, 1984.
- [33] F.G. Baksht, B. Ya Moizhes and A.B. Rybakov ; " Critical Regime of Plasma Accelerator Sov. Phys. " ; Tech.Phys. 18, p 1613, 1974.
- [34] A.P. Shubin; " Dynamic Nature of Critical Regimes in Steady State High- Current Plasma Accelerators " ; Sov. J. Plasma Phys. Vol. 2 p18, 1976.
- [35] G.L. Cann and R.L. Harder ; " Thrust Efficiencies of Electromagnetic Engines " ; AIAA 6 (3) p 558, 1966
- [36] J.L. Lawless and V.L. Subramanian ; " A Theory of Onset in MPD Thrusters " ; Scientific Report AFOSR 83-0033, 1983
- [37] Schrade H.O., Auweter-Kurtz M., Kurtz H.L. ; " Stability Problems in Magnetoplasmadynamics Arc Thrusters " ; 18th Fluid Dynamics and Plasmadynamic and Laser Conf. AIAA 85-1633 July 1985
- [38] Schrade H.O. ; " Magnetoplasmadynamic Effects in Electric Arcs " ; Interim Scient. Report AFOSR 82-0298 Aug. 1983

- [39] Schrade H.O., B. Glocker, and P.C. Sleziona ; " Model Calculation of Arcjet Thrusters "; Report ESTEC Contract No 6784/86/NL/PH(Sc) Dec. 1990
- [40] G. V. Butkevich, G. S. Belkin et al ; " Electrical Erosion of the High Current Contact and Electrodes " ; Doc-86079804
- [41] C.W. Kimblin ;" Cathode Spots Erosion and Ionisation Phenomena in the Transition from Vacuum to Atmosphere Pressure Arcs " ; J. Appl. Phys. 45 p 5235, Dec 1974
- [42] J. L. Meunier and M. G. Drouet ;" Experimental Study of the Effect of Gas Pressure on Arc Cathode Erosion and Redeposition in He, Ar, and SFe from Vacuum to Atmosphere Pressure " ; IEEE Trans. Plasma Sci. Ps-15 p 515 Oct 1987
- [43] R. L. Burton and S.Y. Wang ;" Initial Development of 3kW Pulsed Electrothermal Thruster " ; AIAA 89-2265, 25th Joint Propulsion Conference, Monterey CA, July 1989
- [44] Schrade H.O.; Contribution: " Workshop on Electrode Erosion in Electric Space Propulsion Engines" ; March 1989 Edited by M. Kristiansen and L. Hartfield Tex. Tech. University Lubock, Texas June 1989
- [45] A. L. Donaldson, T. G. Engel and M. Kristianson ;" State of the Art Insulator and Electrode Materials for Use in High Current, High Energy Switching " ; IEEE Trans. on Magnetics, Vol. 25 p. 138 Jun. 1989
- [46] Auweter-Kurtz, M. et. al. ;" Cathode Phenomena in Plasma Thrusters " ; AIAA 90.2662, 21. Electr. Propuls. Conf. Orlando, Fl. July 1990
- [47] Schrade H.O., Auweter-Kurtz M., Kurtz H.L. ; " Analysis of the Cathode Spot of Metal Vapor Arcs " ; IEEE Trans. Plasma Sci. Vol. Ps-11, p. 103 1983
- [48] Schrade H.O., Auweter-Kurtz M., Kurtz H.L. ; " Cathode Erosion Studies on MPD Thrusters " ; AIAA Journal Vol. 25, p 1105 Aug. 1987
- [49] Schrade H.O. ; " Arc Cathode Spots: Their Mechanasim and Motion " ; IEEE Trans Plasma Sci, Vol. Ps 17 p 635, Oct. 1989
- [50] Th. Mayer, Contr. " Foundation of High Speed Aerodynamics " ; Compilation of G.F. Carrier, Dover Publication Inc. New York p 51 ff, 1951
- [51] N.M. Zykova, V.V. Kantsel. V. I. Rakhovskii, I.F. Seliverstvova and A.P. Ustiments ; " Cathode and Anode Regions in an Electric Arc " ; Sov. Phys-Tech Phys Vol. 15, No 11 P.1844,1971